Measuring Spin-Energy Correlations in Nuclear Fission

by

Nathan P. Giha

A dissertation submitted in partial fulfillment
of the requirements for the degree of
Doctor of Philosophy
(Nuclear Engineering and Radiological Sciences)
in the University of Michigan
2024

Doctoral Committee:

Professor Sara A. Pozzi, Co-Chair
Dr. Fredrik Tovesson, Co-Chair
Professor Christine A. Aidala
Professor Igor Jovanovic

Kyle (left), Stefano (middle), and Nathan (left)

October 6, 2021

Ann Arbor, MI, USA

Nathan P. Giha

giha@umich.edu

ORCID iD: 0000-0002-6826-4681

DEDICATION

To Elizabeth, with love.

ACKNOWLEDGEMENTS

This dissertation was made possible by a long list of fellow students, lab scientists, professors, and more, and I feel lucky to call many of them my friends.

I want to first acknowledge the NERS graduating class of 2018—our times together as NER(d)S led to lifelong friendships, and I'm glad that so many of you stuck around for grad school as well: Kyle Beyer, Michael Hua, Flynn Darby, Zach Welker, Chris Swenson, Lauren Green, and more. We made Ann Arbor our home for many years and as our numbers dwindle, I cherish how our little town felt in those days when we were all together. Of course, many of my other graduate student group-mates became great friends and sources of support—whether we overlapped briefly or for many years: Chris Meert, Leah Clark, Ellie Mullin, and Ricardo Lopez.

Thank you to all of the mentors at Michigan who got me to this point. I started my research career with Marc Ruch in May of 2016, and he's still helping me with advice to this day. I have been in Sara Pozzi's group ever since, and over eight years later, it's difficult to conceptualize leaving. Between the pandemic and my petitions to go this way and that during my Ph.D., it has been a strange five years. I appreciate your level-leaded presence. Thank you to both Shaun Clarke and Sara for keeping me around for so long, and for your guidance and mentorship. Thank you as well to Angela Di Fulvio and Will Steinberger, who helped me balance research and academics as an undergrad and into the beginning of grad school.

Thank you to my mentees, who probably have taught me more than I've taught them at this point: James Baker, Ethan Schneider, and Alex Tuckey. I feel lucky to have ended up with such a kind and capable group of mentees, and I know you will all be great scientists if you decide to stay on that path.

Thank you to Fredrik Tovesson at Argonne National Laboratory for wholeheartedly embracing a mentorship that he didn't really ask for. Stefano and I showed up at ANL in February 2022 to put the chamber together and all of a sudden, he was on my committee. Committee of what? Neither of us knew yet. Then, he was co-chairing the committee. Then I was staying at ANL. This experimental campaign, both its execution and analysis, is definitely the most difficult thing I have done, and it is thanks to him that we made it through.

It is apparent that Fredrik cares about this field and whatever we can do to advance it. Thank you for hosting me at ANL and for your invaluable contributions to this dissertation over the past couple years.

Thank you to the mentors from other institutions who generously lent a few months of their time to a curious intern. I thank Filip Kondev from Argonne National Lab for teaching me all about gamma-ray spectroscopy and level schemes; I had no idea it would work out so well at the time, but that knowledge became extremely important to my dissertation. Thank you to Dan Akerib and Tom Shutt from SLAC for making that leap of faith that led you to bring me into the Liquid Nobles group for a few months, and to Ann Wang and Alden Fan for teaching me the ways of LZ. Thank you to Maris Arthurs for being an excellent friend during our stay in Redwood City.

Thank you to John Rodriguez and Courtney Wagoner for being absolute rock-star project managers. Every single administrative hurdle was so much easier thanks to your help, and it certainly doesn't hurt that you're great people.

Thank you to my collaborators on the LANL and ANL projects who made this work possible. On the LANL side, thank you to Keegan Kelly and Matt Devlin for giving us your data, and going the extra mile to meet with me several times to explain things as we rifled through it. At ANL, thank you to Michael Oberling, Russell Knaack, and Ivan Tolstukhin for not only building us a high-performing (and quite beautiful) chamber, but for being incredible friendly and supportive over the past couple years. I will miss our small talk in the hallways at ANL. Thank you to Dana Duke and her former team at LANL for giving us a great start on our fragment analysis scripts. Lastly, thank you to almost the entire low-energy physics group at Argonne—most of you helped some way or another during the 2023 experimental run, whether it be taking shifts or debugging the many issues we encountered. Thank you especially to Claus Mueller-Gatermann and Amel Korichi for your support during the experiment. Michael O. and Ivan deserve another mention here as well, making the run a success.

Thank you to the broader fission community for their hospitality, and especially Dorthea Gjestvang and Ramona Vogt. Dorthea, I really appreciate our fission discussions and the enthusiasm you bring for our field, and for science in general. I hope that we can share an office one day. Ramona, thank you for always expressing interest in my work, helping me broadcast it to the community, and making an effort to meet up and discuss.

Thank you to Kyle Beyer and Stefano Marin, my brothers in arms in fission. We may not have been in a physics department, but look at us now: three physics postdocs. Who would've thought? It was our camaraderie that kept me slogging through the most difficult portions of the Ph.D.

Thank you to Kyle for being my buddy. It's a running theme at this point that we end up in the same places and stay together: Lawrence St, Hawai'i, and most recently, Taos. Let's keep that up. Elizabeth and Dana can come, too.

Thank you to Stefano for teaching me how to be a good experimentalist, to convince myself before I try to convince others. I stand at the top of this mountain thanks to you. The view is nice, and satisfying, but there are higher peaks still in the distance. More importantly, thank you for being a great friend. I'm looking forward to being a stone's throw away from you for at least a couple years.

Thank you to my family for your enthusiasm and support over the past five years. You were home base during a wild few years of constant moving and travel, and always let me know how proud you were.

Lastly, thank you to my wife, Elizabeth. The last couple months were insane: a wedding interleaved with dissertation submission and defense, and not on a relaxing sort of timeline. Mixed in, the stresses of figuring out where we would end up next. It is a testament to your strength and patience that we are on the other side in once piece. I am excited to start our next chapter together in the City of Light. I love you.

TABLE OF CONTENTS

LIST OF FIGURES

FIGURE

LIST OF TABLES

TABLE

LIST OF ACRONYMS

TKE Total Kinetic Energy

TXE Total eXcitation Energy

LDM Liquid Drop Model

NLD Nuclear Level Density

g.s. Ground State

CN Compound Nucleus

PPAC Parallel Plate Avalanche Counter

PCB Printed Circuit Board

ENIG Electroless Nickel Immersion Gold

HV High Voltage

IYR Isomeric Yield Ratio

ABSTRACT

Despite over eighty years of study since nuclear fission was discovered, important details of this nuclear process remain poorly understood. Among them is the mechanism by which fission fragments acquire substantial spins, or angular momenta, despite originating from a heavy nucleus that may start with no spin. Thanks to advances in computational models of fission, theorists and experimentalists have recently put forth renewed effort toward revealing this spin generation mechanism. A truly predictive model of fission—with the correct spin generation mechanism—would have far-reaching implications on our understanding of fission recycling in the r-process of nucleosynthesis and our ability to simulate fission neutron and γ-ray emission for nuclear safeguards and nonproliferation scenarios.

This dissertation aims to measure correlations between the spin generated in the fission fragments and the energy available to them. Practically, we measure correlations between fission γ-ray emission and properties of the fragments that emit them. We first measure the γ-ray multiplicity and spectrum from ^{239}Pu(n,f) as a function of incident neutron energy using the Chi-Nu liquid scintillator array at the Los Alamos Neutron Science Center. We then develop and characterize a specialized fission fragment detector that measures the fragments' kinetic energies and masses at Argonne National Laboratory. Loaded with a ^{252}Cf(sf) source, We place that fragment detector inside Gammasphere, a high-resolution and high-granularity γ-ray spectrometer, to measure correlations between the kinetic energies of specific fragments and γ-ray spectra they emit. We leverage our knowledge of the fragments' nuclear level schemes to reconstruct their spin distributions as a function of energy for the first time. Focusing on ^{144}Ba, we find its average spin to be insensitive to energy—inconsistent with predictions from solely statistical excitation of rotational modes in the fragments. We thus conclude that more complex modes of spin generation are at play in fission.

We discuss the corpus of correlated fission measurements that are relevant to spin generation and show how our measurements fit into that collection. We suggest improvements to the presented experiments in case they are repeated in the future, as well as straightforward extensions to the analysis presented in the dissertation with the existing data sets. Finally, we propose future experiments and analyses that will unlock entirely new fragment initial conditions and measured quantities, respectively.

CHAPTER 1

Introduction

Nuclear fission is both interesting and important. Discovered in 1938 [1, 2], it is the very extreme of nuclear deformation in which the perpetually vibrating nucleus cannot hold itself together, and blows apart in spectacular fashion. It is the competition between the Coulomb and strong nuclear forces, with completely different coupling constants and length scales. It takes less than a femtosecond, yet its effects persist for years in the form of β-unstable products. It is also important in calculating elemental abundances in the r-process of nucleosynthesis due to fission recycling [3–7].

Fission is also a dual-use technology: capable of generating an abundance of clean and safe energy, or when weaponized, of destruction on a massive scale. The nuclear weapons states which brought about nuclear weapons and continue to maintain stockpiles of them assume an additional responsibility in ensuring that fissionable material is not used for nefarious purposes.

Since its discovery, nuclear fission has accumulated a rich experimental history. There are so many things that can be measured in fission. The yields, kinetic energies, masses, and angular distributions of the two (or more) fragments, the energies, directions, and multiplicities of the prompt fission neutrons and γ rays, can all be measured. Upon studying correlations between two of these quantities, or even correlations among several of them, we can begin to uncover hints of how fission works. Examples include neutron [8] and γ-ray multiplicity [9, 10] as a function of fragment mass, γ-ray emission as a function of fragment energy [10–12],

angular distributions of neutrons and γ rays relative to the fission axis [8, 10], and more derived quantities such as fragment spin as a function of mass via γ-ray spectroscopy [13, 14] or isomeric yield ratios [15]. Correlated measurements are key to differentiating between models of fission which might agree well on the integral quantities above, but have quite disparate predictions for their relationships.

Recent experimental and theoretical efforts in fission have focused on determining the mechanism by which two fragments, each with several $\hbar$ of spin, emerge from a system with zero or near-zero spin. The experiments in this dissertation focus on measuring correlations between the energies of the fission fragments and the γ rays they emit. As we will see, γ-ray emission is highly correlated with the initial spin, or angular momentum, of a fission fragment. We discuss how our measurements relate to the relationship between the excitation energy (E^*) and spin (J, or sometimes I) of fragments, and interpret what our results suggest about the spin generation mechanism.

1.1 The Discovery of Fission

The discovery and study of fission is intrinsically tied to the Second World War and the Manhattan Project, but the proverbial ball started rolling before then. In 1934-35, Enrico Fermi bombarded uranium samples with neutrons in an attempt to make transuranic elements with $Z > 92$ [16]. He believed he succeeded, having observed β^- decays after the bombardment [17], but Ida Noddack correctly guessed that the uranium nuclei had "disintegrate[d] into several larger fragments." Physicist Lise Meitner and her chemist colleague Otto Hahn, along with Fritz Strassmann, began similar experiments. Meitner, due to her Jewish descent, fled from the German lab in July 1938 to escape the Nazis. Just a few months later, Hahn and Strassmann continued their work and and found isotopes of barium, but could not interpret the results in the frame of a nuclear reaction [1]. They reached out to Meitner and shortly after, she published a paper in Nature [2] with her nephew Otto Frisch.

Meitner and Frisch interpreted it in the frame of a drop of liquid nuclear matter breaking apart and releasing ~ 200 MeV, and borrowed the term "fission" from biologists. Hahn was awarded with the 1944 Nobel Prize in Chemistry. Meitner's profound contributions to the discovery went unrecognized.

There are many accounts of the Manhattan Project, even in pop culture [18]. It came to a head in August of 1945 when the US dropped two nuclear fission weapons, a gun-type design with ^{235}U called Little Boy and an implosion-type with a ^{239}Pu pit called Fat Man, on Hiroshima and Nagasaki. Since then, it has become of global importance to control materials which could be used to make such weapons.

1.2 Physical Overview

Nuclear fission occurs because as nuclei grow past ^{56}Fe, additional nucleons generally become more and more loosely bound. Thus, systems with > 180 or so nucleons can achieve a lower energy state by splitting. The total energy released in fission, Q, is simply $Q = m_A - \sum m_{\rm f}$, where m_A is mass of the fissioning nucleus and the sum runs over all fragments with masses $m_{\rm f}$. Typical Q values are about 200 MeV, although it depends on the reaction. Most of the energy goes to the total kinetic energy (TKE) of the fragments, around 170 MeV, while the rest goes to internal excitation energy in the fragments (E^* for a single fragment, or TXE when referring to the sum).

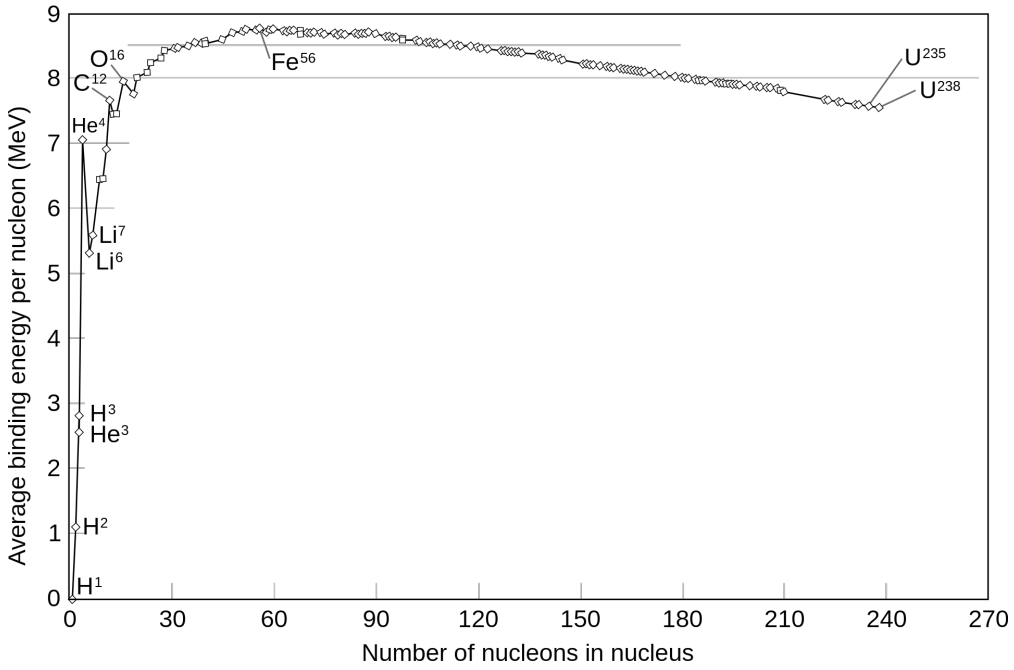

Figure 1.1: Binding energy per nucleon, as a function of nucleon number [19].

Fission is not the only decay channel available to heavy nuclei that want to lose nucleons. Most heavy nuclei that are unstable to nucleon emission will emit α particles. In fact, even for nuclei that do fission spontaneously like ^{252}Cf, ^{240}Pu, ^{238}U, etc., they are much more likely to emit an α particle. The reason for this bias against fission is one of nuclear deformation—nuclei are constantly vibrating and slightly changing shape, but only some will deform enough to reach the "saddle point" that leads to fission with any regularity. As a result, there is a "fission barrier" that a system must either tunnel through, or overcome with the help of an external energy source.

1.2.1 The Liquid Drop Model

Bohr and Wheeler initially used the liquid drop model (LDM) to explain fission as the Coulomb repulsion winning its competition over the surface tension of an incompressible nuclear fluid, traversing a potential barrier that resists forming non-spherical shapes—like is required for fission—in the process. They derived an impressive amount of information about

fission from this model, with few other ingredients [20]. After surmounting the fission barrier, the drop would continue to stretch until it splits into two roughly equal parts—fragments. The total energy E_{tot} of such a droplet of incompressible, positively-charged fluid with a certain shape is modeled as

$$E_{tot} = E_{vol} + E_{surf} + E_{Coul} + E_{symm} + E_{sp} \tag{1.1}$$

where E_{vol} is the volume energy, E_{surf} is the surface energy, E_{Coul} is the Coulomb repulsion energy, E_{symm} is the Pauli energy, and E_{sp} is the spin pairing energy [21, 22]. This model can be used to find the energy of nuclear shapes, and therefore determine the energy required to deform a nucleus to the "saddle point," after which it would descend into fission. If we only consider axially symmetric configurations, the coordinates of the nuclear surface r can be expanded in Legendre polynomials P_l like so

$$r(\cos\theta) = R\left(1 + \sum_{l=1}^{\infty} \alpha_l P_l(\cos\theta)\right), \tag{1.2}$$

where R is the radius of a spherical (i.e. not deformed) drop of nuclear matter and α_l are the coefficients that determine the contribution from the Legendre polynomial of degree l to the nuclear shape. Since the volume, Pauli energy, and spin pairing do not depend on these α_l, we only need to consider the surface and Coulomb terms to imagine the shape of the LDM fission barrier. Fig. 1.2 from Bohr and Wheeler's paper shows a representation of the fission barrier as a function of a set of deformation parameters α.

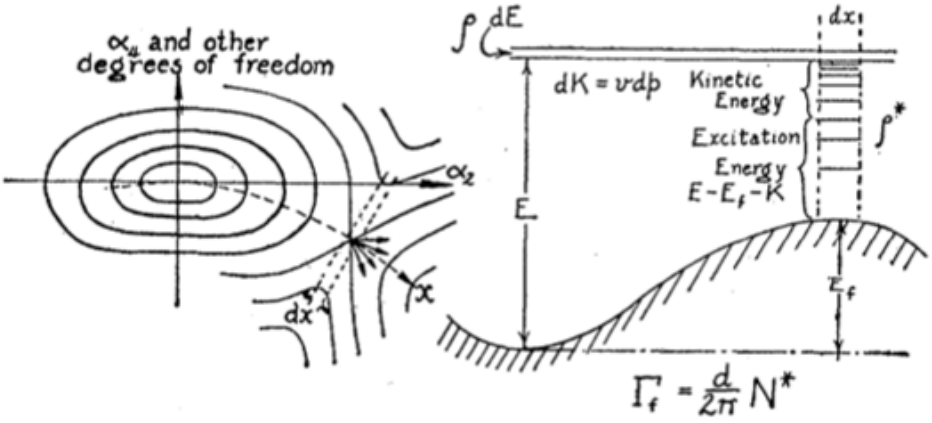

Figure 1.2: Fission barrier in the liquid drop model. Potential energy surface as a function of the set of deformation parameters α, from Ref. [20]

The liquid drop model has many attractive qualities: it offers an intuitive explanation of the fission barrier and yields decent estimates for quantities like the TKE. However, one would expect a symmetric distribution in fragment (Z, A) with this model, and that is decidedly not the case for major fissioning actinides like ^{252}Cf, ^{235}U, ^{239}Pu, and so on.

1.2.2 Shell effects

The fragment mass yield can be highly asymmetric depending on the fissioning nucleus, resulting in "light" and "heavy" fragment peaks. An early measurement of the mass yield for ^{252}Cf(sf) is shown in Fig. 1.3 [23]. This difference from the LDM prediction is due to nuclear shell effects. The macroscopic LDM model must therefore be modified with a microscopic component (Strutinsky shell correction [24]) to accurately model the fission barrier shape. A contemporary rendition of the potential energy surface with shell effects included is shown in Fig. 1.4. The characteristic double-humped fission barrier structure is visible, at $q_2 \sim 2$ and 4. A notable feature is the large barrier at $q_2 \sim 5, \alpha_g \sim 0$, which strongly suppresses symmetric fission at lower potential energies.

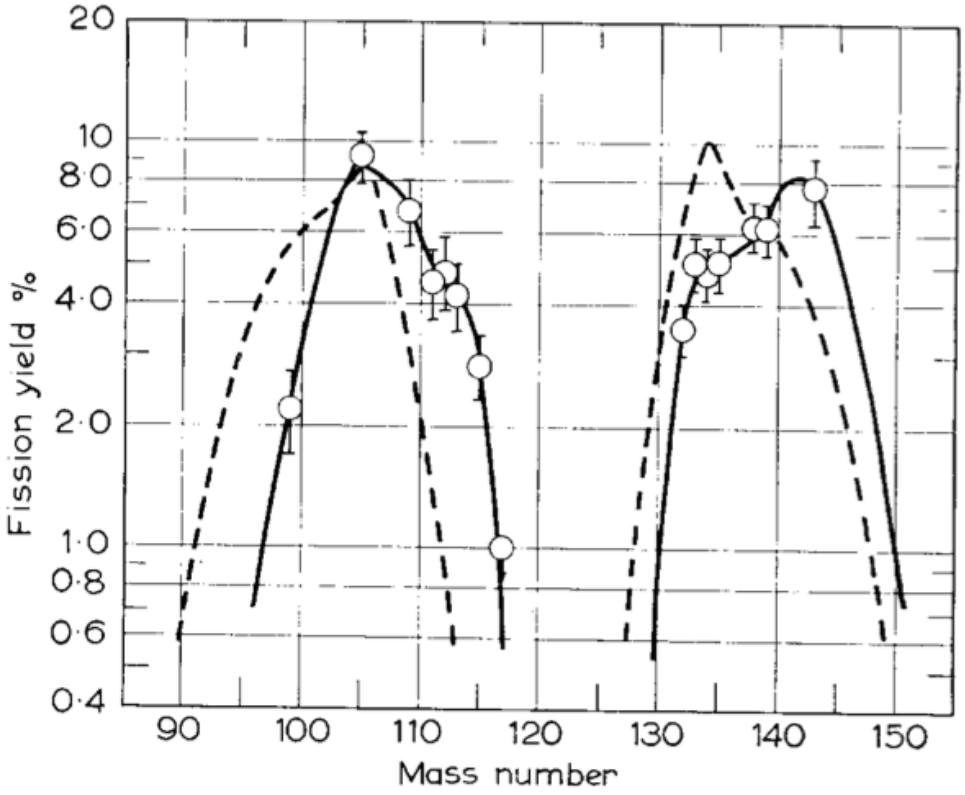

Figure 1.3: Fragment mass yield for ^{252}Cf(sf), (solid line) and ^{242}Cm(sf) (dashed line), from Ref. [23].

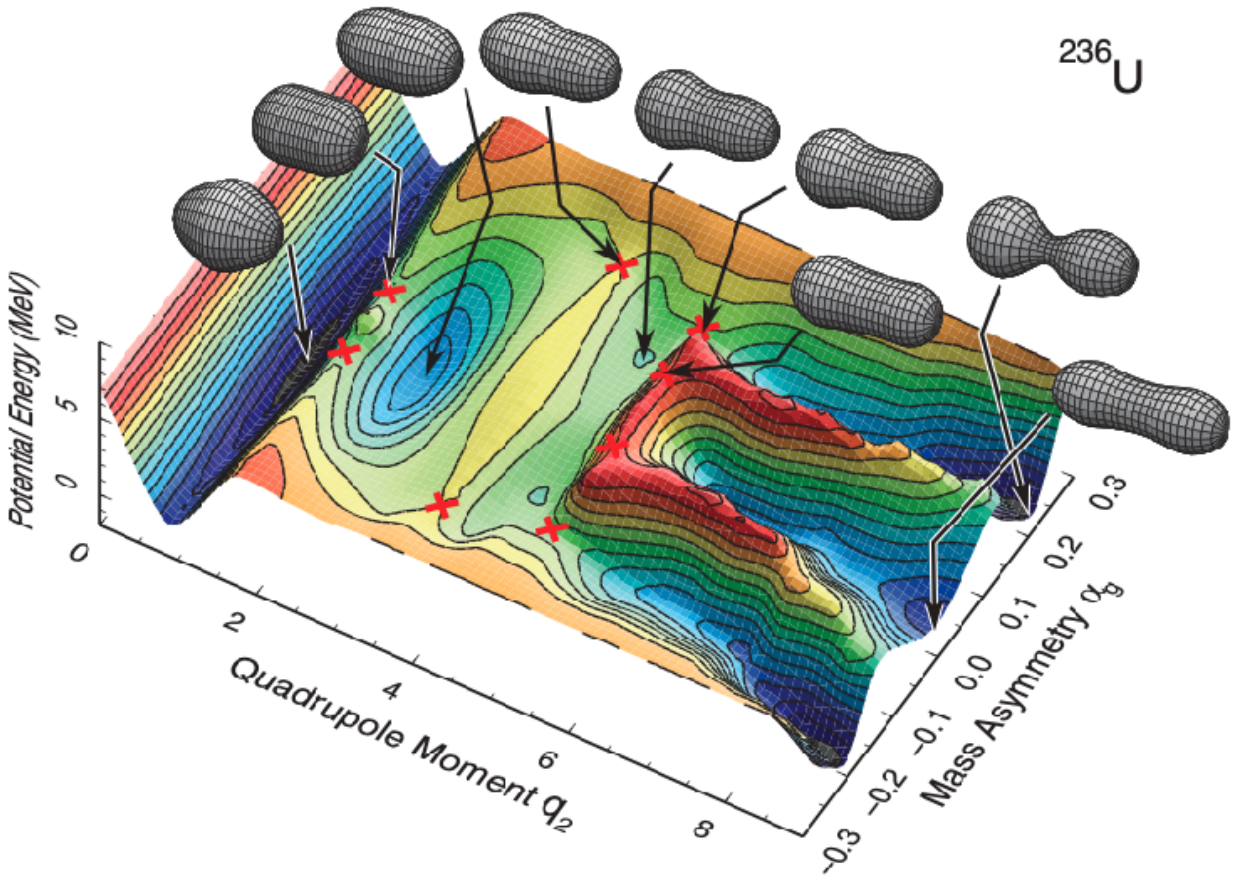

Figure 1.4: Two-dimensional potential energy surface for ^{236}U, from Ref. [25].

Once the nucleus splits, the fragments can be treated as separate systems that reach thermal equilibrium before any particle emission occurs.

1.2.3 Timeline of fission

Fission involves all three fundamental forces in the Standard Model—the strong nuclear and electromagnetic forces compete for supremacy during scission, prompt neutron emission is governed by the strong force, prompt γ-ray emission by the electromagnetic force, and β-decay of the fragments by the weak force. Correspondingly, the process spans many orders of magnitude in time.

This timeline is illustrated in Figure 1.5. Scission is estimated to take $\sim 10^{-21} - 10^{-20}$ s and is experimentally inaccessible. Since prompt neutron emission begins at around 10^{-18}

s after scission, the nascent fragments are never accessible either. This time scale is much longer than the time it takes for a nucleon to orbit in the nucleus ($\sim 10^{-22}$ s), so the prompt emission can be said to come after the fragment has a chance to equilibrate. γ-ray emission usually takes less than 10^{-12} s, but that depends on whether a fragment gets stuck in a long-lived isomeric state. To reconstruct the initial conditions (E^*, J) of the fragments right after scission, we apparently must measure the prompt neutrons and γ rays.

Figure 1.5: A timeline of the fission process, from Ref. [26].

1.2.4 Fragment de-excitation

After scission the fission fragments quickly reach thermal equilibrium, possessing large amounts of E^* (around 20 MeV for ^{252}Cf(sf)) and spin (around 6-8 $\hbar$). If the E^* of a fragment exceeds the neutron separation energy, S_n, then a neutron will usually be emitted with a kinetic energy based on the fragment temperature. Neutrons are generally considered to remove little of the fragment's spin since they are emitted isotropically in the fragment frame [8], although this assumption has been challenged recently by a theoretical study [27]. Prompt neutron emission generally proceeds until $E^* < S_n$, although there is some competition with γ-ray emission when E^* is just above S_n [28]. Fragments borne from ^{252}Cf(sf) usually emit between 0-3 neutrons each. Note that scission neutron emission, which is an active topic of fission research, is omitted from this picture.

After prompt neutron emission, the nucleus is usually left with most of its initial J and a few MeV of E^* above the "yrast line". The nuclear level density (NLD) is still relatively high in this regime, so the following γ-ray emission is well-characterized statistically with the

NLD and γ-ray strength function. $E1$ transitions dominate in this statistical regime. They are not necessarily stretched—and can even increase a fragment's J—so the average effect on J is assumed to be low. Statistical γ-ray emission proceeds until the fragment reaches the yrast line, where the NLD is low. Discrete, identifiable γ-ray transitions start to dominate.

Discrete γ-ray emission is central to the work presented here since these γ rays are responsible for removing most of the fragments' spins [13, 14]. The nuclear level schemes of common fission fragments are well-studied: the energies and spins of the levels, as well as the energies and spins of the allowed γ-ray transitions are recorded in libraries such as the evaluated nuclear structure data files (ENSDF) [29]. Measuring the γ rays with identifiable energies provides a nearly model-independent method for reconstructing the spins of fission fragments post-statistical emission.

A diagram of the entire de-excitation process is shown in Figure 1.6. Figure 1.7 shows the E^*-J plot for low-lying levels of ^{144}Ba, a common fragment for low-energy actinide fission. The "yrast band," or the band of states with the lowest energy at a given spin, is clearly visible.

1.3 Outline

In Chapter 2 we measure the dependence of prompt γ-ray emission on energy in ^{239}Pu(n, f). After transforming from incident neutron energy, E_i, to average compound nucleus excitation energy, $\langle E_x \rangle$, we observe an approximately linear increase in the γ-ray multiplicity between $9 < \langle E_x \rangle < 19$ MeV. We determine that most of the additional γ rays come from an enhancement around $E_\gamma = 0.7$ MeV—characteristic of the stretched quadrupole γ-rays that remove much of the fragments' spin—and conclude positive, approximately linear E^*, J correlations in the studied energy range.

In Chapter 3 we introduce the twin Frisch-grid ionization chamber (TFGIC) that we built at Argonne National Laboratory in Lemont, IL. The TFGIC is designed to measure

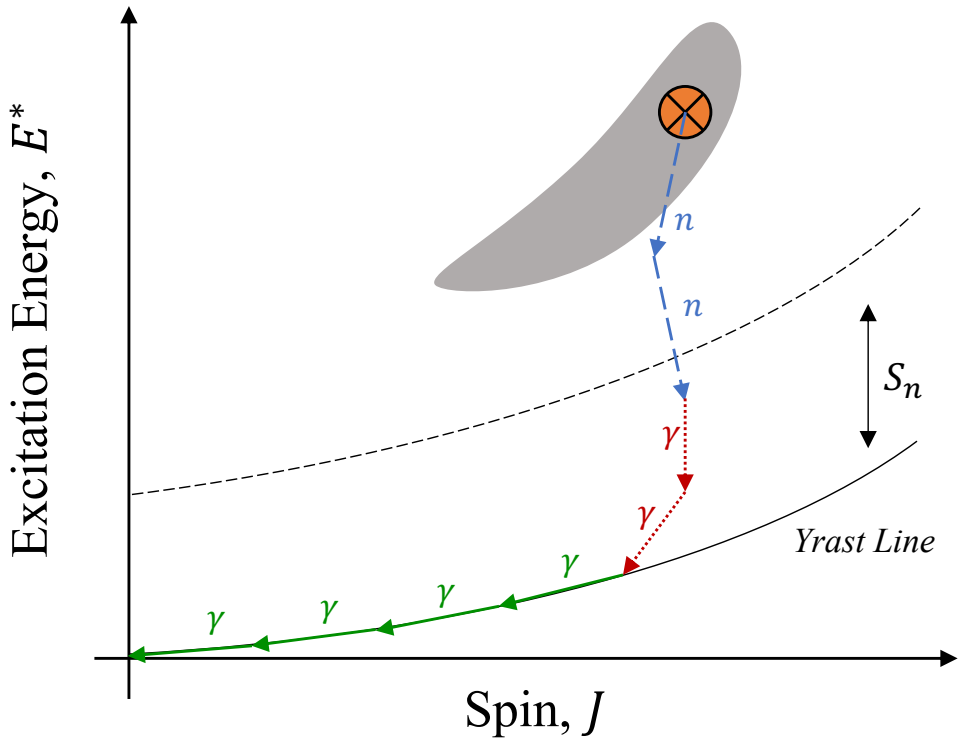

Figure 1.6: De-excitation of a fission fragment by emission of neutrons, statistical γ rays, and discrete γ rays. The yrast line follows the nuclear levels with minimum E^* for a given J. Neutrons are in dashed blue, statistical γ rays in dotted red, and discrete γ rays in solid green arrows.

the kinetic energies, masses, and directions of the fission fragments in binary fission while remaining mostly transparent to the prompt neutrons and γ rays. We performed a characterization of the chamber's resolutions for these measurements, combined with a scintillator array, in preparation for the experiment discussed in Chapter 4.

In Chapter 4 we discuss an experiment we performed at Argonne National Laboratory and the first analysis of this unique data set. We measure the average spin $\langle I \rangle$ of ^{144}Ba, a common fragment produced in ^{252}Cf(sf), as a function of TKE. We combine the twin Frisch-grid ionization chamber from Chapter 3 with Gammasphere, a world-class γ-ray spectrometer comprising Compton-suppressed HPGe detectors, which was designed to measure high-multiplicity γ-ray events. The chamber was loaded with a ^{252}Cf(sf) source and provides a fission trigger, the TKE of the fragments, the approximate fragment masses, and

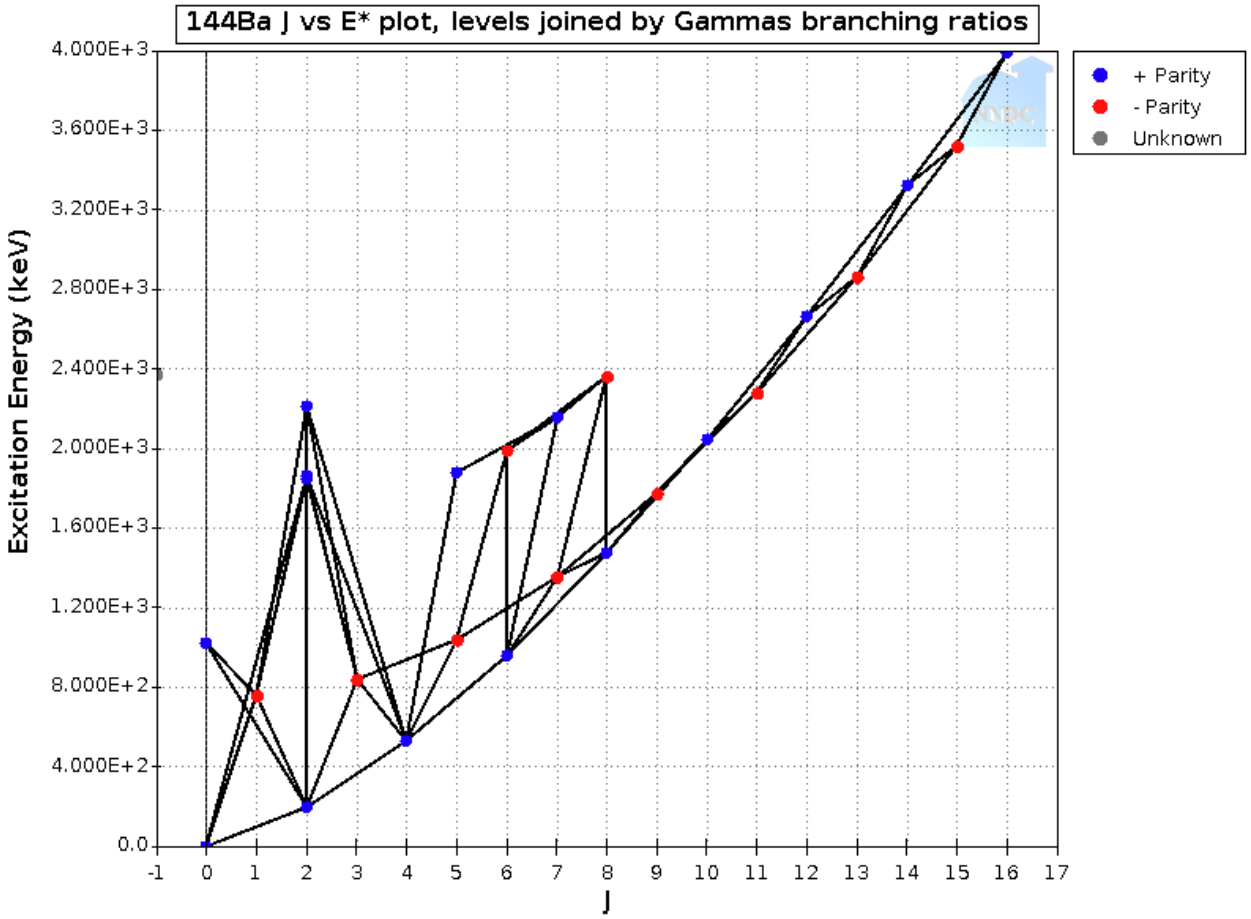

Figure 1.7: J vs. E^* for low-lying states in ^{144}Ba. The "yrast band," or the band of states with the lowest energy at a given spin, in this case consists of states in the ground-state and octupole bands. Retreived from NNDC on 18 Jan 2024.

the polar angle of the fission axis. Gammasphere provides the total γ-ray yield, fragment identification through the tagging of decay γ rays, and the feeding of rotational bands in the fragments. We determine the dependence of $\langle I \rangle$ on the fragments' TKE by correlating the fragment properties with the distribution of discrete levels that are fed. The resulting virtual independence of the spin of ^{144}Ba on TKE suggests that spin is not generated through the statistical excitation of rotational modes, and more complex mechanisms are required.

In Chapter 5 we summarize these experiments, discuss the implications of these experiments and others on our understanding of fission, and suggest possible pathways for the future of this project.

CHAPTER 2

Correlations Between Energy and γ-ray Emission in Neutron-Induced Fission of ^{239}Pu

2.1 Introduction

In Chapter 2 we explore γ-ray emission from the ^{239}Pu(n,f) reaction. Induced fission offers a straightforward path to increasing the total excitation energy available to the fragments—adding incident neutron energy increases the excitation energy of the ^{240}Pu* compound nucleus (CN) by the same amount, up to a small correction for the CN kinetic energy. Studying the γ-ray emission as a function of the incident energy, we can then infer something about spin-energy (E^*-J) correlations. Understanding the relationship between the excitation energy of the fissioning system—and consequently of the fragments—and the fragment spins is critical for constraining the possible mechanisms of spin generation. For example, the popular statistical model posits that the high spins with which fragments emerge are solely due to the higher density of high-spin states at large excitation energy [30]. This model would result in a nonlinear dependence of spin on excitation energy.

There is a rich history of neutron-induced fission experiments, thanks in large part to its significance to nuclear technologies like power reactors. For the same reason, however, these experiments studying emission from neutron-induced fission lean overwhelmingly toward measurements of prompt fission neutrons rather than γ rays. Still, plenty of measurements of fission γ rays from neutron-induced fission exist, but mostly for thermal neutron-induced

Table 2.1: Fission γ-ray measurements and whether they were able to statistically resolve changes in γ-ray multiplicity, $\Delta\overline{N}_\gamma$, or changes in the γ-ray spectrum, ΔSpec. For neutron-induced reactions other than ^{239}Pu(n,f), E_x above the 2$^{\mathrm{nd}}$-chance fission threshold are omitted. Experiments by Fréhaut are frequently cited in discussions about the energy dependence of spin in fission, but the conclusions in Refs. [31] and [32] are contradictory.

Reference	Reaction	E_n	E_x	$\Delta\overline{N}_\gamma$	ΔSpec
This work	^{239}Pu(n,f)	2-40	9-19	✓	✓
ENDF/B-VIII.0 [37]	^{239}Pu(n,f)	0-20	6.53-19	✓	
Fréhaut [31, 32]	^{235}U(n,f)	1.14-14.66	7.69-12.22	N/A	N/A
Qi [33]	^{238}U(n,f)	1.90,4.90	6.71,9.61		
Laborie [34]	^{238}U(n,f)	1.6,5.1,15.0	6.41,9.91		✓
Oberstedt [35]	^{235}U(n,f)	$\overline{E}_n = 1.7$	$\overline{E}_x = 8.25$		
Rose [36]	^{233}U$(d,p\mathrm{f})$	-	4.8-10		
Rose [36]	^{239}Pu$(d,p\mathrm{f})$	-	4.5-8.8		
Gjestvang [11]	^{240}Pu$(d,p\mathrm{f})$	-	5.5-8.5	✓	

fission. Experimental investigations on the dependence of γ-ray emission on the energy of the fissioning system are sparse [11, 31–36]. In most cases, the experiments investigated only a few different energies or a limited energy range, and could not resolve any trends in the multiplicity or energy spectrum as a result. Table 2.1 summarizes these experiments, listing the investigated reaction, energies, and whether or not they observed changes in the γ-ray multiplicity and spectrum. The ENDF/B-VIII.0 evaluation for ^{239}Pu(n,f) is also included. Note that only Gjestvang *et al.* [11] identified a significant change in γ-ray multiplicity. Only Laborie *et al.* [34] found changes in the γ-ray spectrum, but exclusively above 2 MeV in γ-ray energy, uncharacteristic of the yrast transitions that are related to fragment spin.

In this Chapter, we analyze the ^{239}Pu(n,f) data from Kelly *et al.* [38], in which a broad range of excited states of ^{240}Pu* were populated. We present clear experimental evidence for increasing γ-ray multiplicity, $\overline{N}_\gamma$, over the incident neutron energy range of $2 < E_i < 40$ MeV. We find an approximately linear relationship between $\overline{N}_\gamma$ and the average compound nucleus (CN) excitation energy, $\langle E_x \rangle$, within $9 < \langle E_x \rangle < 19$ MeV. Furthermore, by differentiating with respect to the γ-ray energy, E_γ, we find the γ-ray multiplicity around $E_\gamma = 0.7$ MeV—characteristic of $E2$ transitions along fragment rotational bands—increases with the

excitation energy of the compound system. We compare our results to phenomenological fission models CGMF [39], FIFRELIN [40], and FREYA [41], and ultimately suggest a positive, approximately linear spin-energy correlations in the measured energy range. This conclusion, while not sufficient to rule out the non-linearity expected in the statistical model of spin generation on its own, gives a clue that the mechanism may be more complicated.

We include details of the experiment in Section 2.2, analysis in Section 2.3, and fission models in Section 2.4. We present our results, discussion, and conclusions in Sections 2.5, 2.6, and 2.7.

2.2 Experimental setup and procedure

The experiment was carried out at the Los Alamos Neutron Science Center [42], where a broad-spectrum neutron beam was produced via spallation reaction of an 800 MeV proton beam on a tungsten target. The neutron beam, ranging in kinetic energy from thermal (0.025 eV) to hundreds of MeV, was incident on a multi-foil Parallel-Plate Avalanche Counter (PPAC, Fig. 2.1) [43] containing 100 mg of ^{239}Pu, 21.5 m from the spallation target.

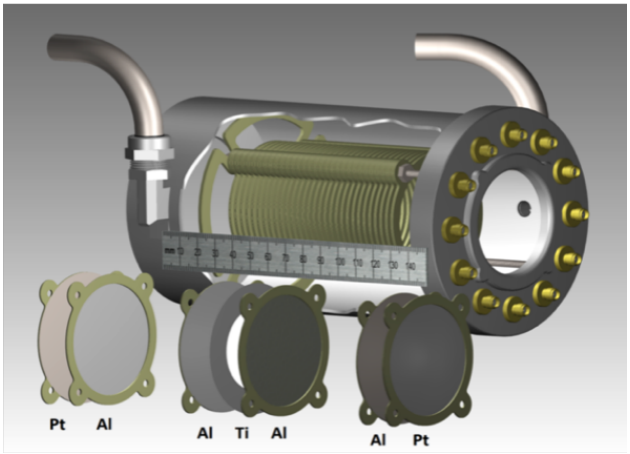

Figure 2.1: Rendering of the PPAC, from Ref. [43].

Neutron-induced fission was measured in the PPAC and the neutrons and γ rays emitted by the fragments were measured using the Chi-Nu liquid scintillator array (Fig. 2.2), a

hemispherical array of 54 EJ-309 [44] organic scintillator detectors. We separate the data into quasi-monoenergetic bins of incident energy, E_i, determined by the neutron time of flight between spallation and measurement of fission in the PPAC. A detailed description of the experiment that generated these data is available in Kelly *et al.* [38]. Whereas Kelly *et al.* focused on prompt fission neutron measurements, we apply an entirely new analysis to the fission γ-ray data.

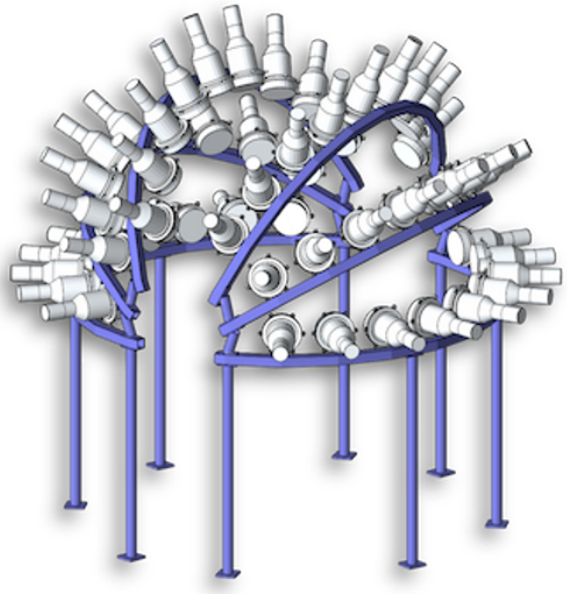

Figure 2.2: Rendering of the Chi-Nu liquid scintillator array, from Ref. [38].

2.3 Analysis

Since the target nucleus ^{239}Pu is unstable to α decay, the PPAC signal from pileup of multiple α events cannot always be separated from that produced by decelerating fission fragments. This α pileup presents a significant background for fragment detection. The background trigger rate from ^{239}Pu α decay during beam-on is estimated by examining the measured PPAC activity and spectrum in the absence of beam, see Fig. 2.3. This background is subtracted from the beam-on spectrum (Fig. 2.4) to isolate the fission events (Fig 2.5).

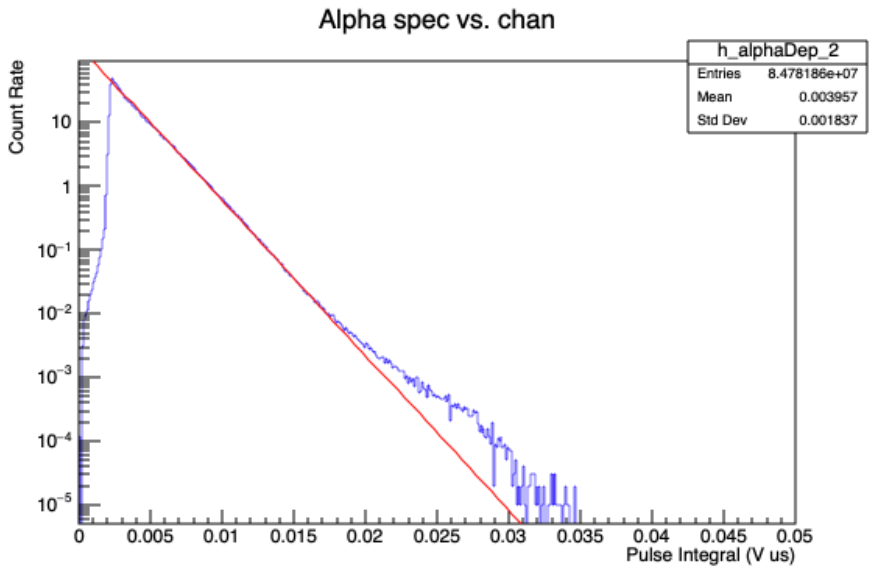

Figure 2.3: α spectrum in a PPAC plate, gating on pre-beam (blue histogram). The exponential fit (red line) was not used in the analysis.

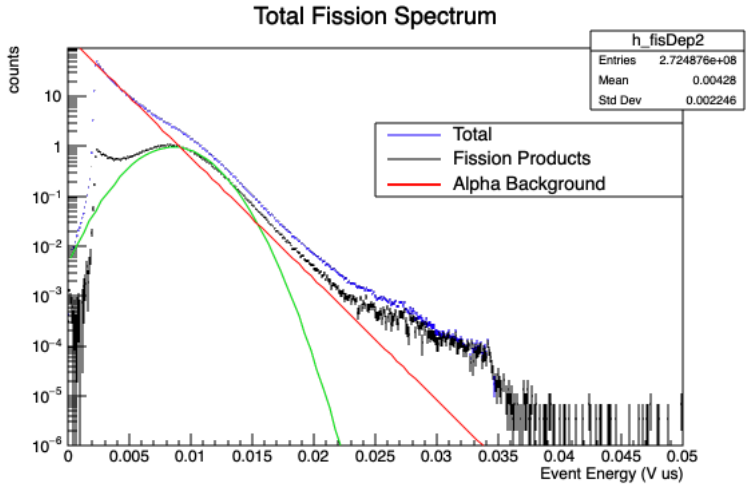

Figure 2.4: α + fission spectrum in a PPAC plate, in-beam (blue histogram). The exponential+gaussian fit (red and green lines) was not used in the analysis.

This procedure informed the choice of PPAC threshold of 0.005 V·μs. Integrating the net PPAC spectrum in Fig. 2.5, we obtain the total number of fissions. Since many quantities in fission are affected by the total kinetic energy (TKE) of the fragments, care was taken to ensure that this choice of threshold did not bias the selected fission events: the fission neutron multiplicity and energies, γ-ray multiplicity and energies, and incident neutron energy did

not exhibit any correlations with the threshold choice. We explain this with the geometry of the PPAC: its energy response is highly dependent on the angle of fragment emission with respect to the surface of the plates, which greatly overshadows any correlations between the PPAC signal magnitude and the TKE.

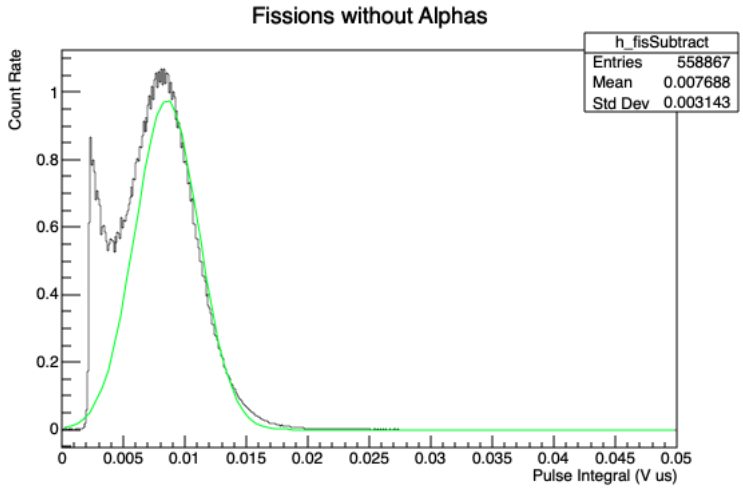

Figure 2.5: Fission spectrum in a PPAC plate upon subtracting α pileup background. The gaussian fit (green line) was not used in the analysis.

Fission γ rays and neutrons, measured in coincidence with beam and PPAC triggers, are discriminated based on pulse shape and time of flight. After applying both discrimination techniques, particle misclassification becomes negligible [45]. We collect γ rays within a window of 5 ns before to 10 ns after the PPAC trigger. The full width at half maximum of this coincidence peak is 3.1 ns. To recover the emitted fission γ-ray spectrum from the detected events, several corrections are applied.

We quantify the effect of chance coincidences between the γ-ray background and the beam trigger by introducing a random coincidence signal in the analysis. Its contribution is small and we subtract it. While multiple γ rays and neutrons are usually emitted in the same fission, pileup can be neglected due to the low absolute efficiency of the detector array: about 2.9%.

The pulsed nature of the broad-spectrum neutron beam results in low-energy neutrons from a beam micropulse arriving at the target simultaneously with high-energy neutrons

from the next micropulse. This effect is called "wraparound." We estimate the amount of fission induced by these low-energy neutrons and subtract. This correction is negligible at low E_i and the proportion of fissions from wraparound never exceeds 3.4% as E_i approaches 40 MeV.

We apply the following unfolding procedure to recover the emitted γ-ray spectrum at each E_i: we first model the system response of the Chi-Nu liquid scintillator array using isotropic, monoenergetic photon sources in MCNPX-POLIMI [46]. We then convolve the resulting response matrix for each PPAC plate with experimentally-determined detector resolution and a scintillator light output threshold of 0.1 MeVee to produce matrices like Fig. 2.6. The simulation, and therefore the response matrix, includes detector crosstalk effects.

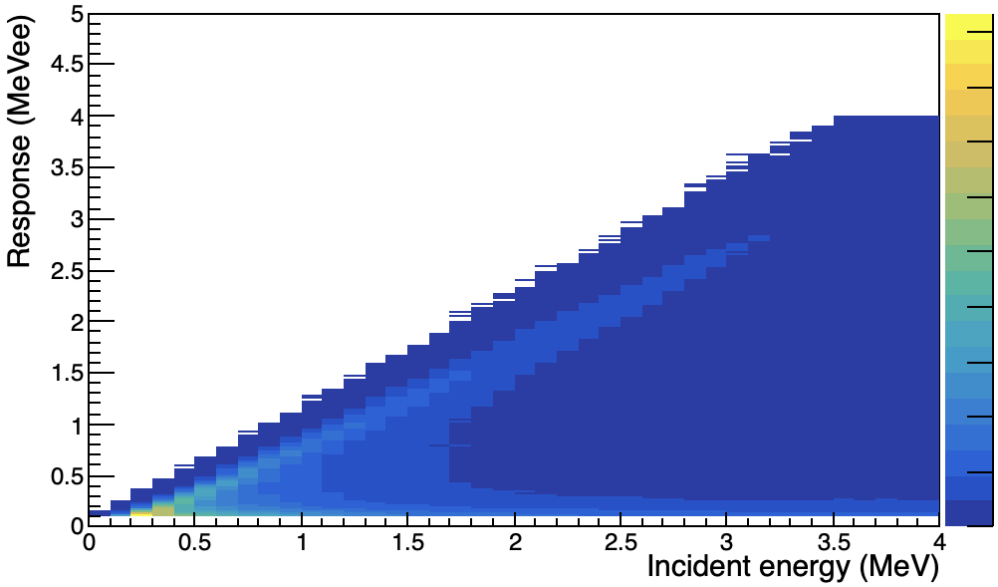

Figure 2.6: Simulated Chi-Nu γ-ray response matrix for a single PPAC plate.

We then invert the response matrix after Tikhonov regularization [47]. This procedure corrects the measured multiplicity for efficiency and unfolds the emitted E_γ spectrum from the measured γ-ray light output spectrum. The regularization parameter, α, was chosen to minimize the difference between the unfolded γ-ray spectrum at our lowest energy bin, $2 < E_i < 3$ MeV and the ENDF/B-VIII.0 evaluated spectrum for ^{239}Pu(n_{th}, f) [48]. We

compare them in Fig. 2.7.

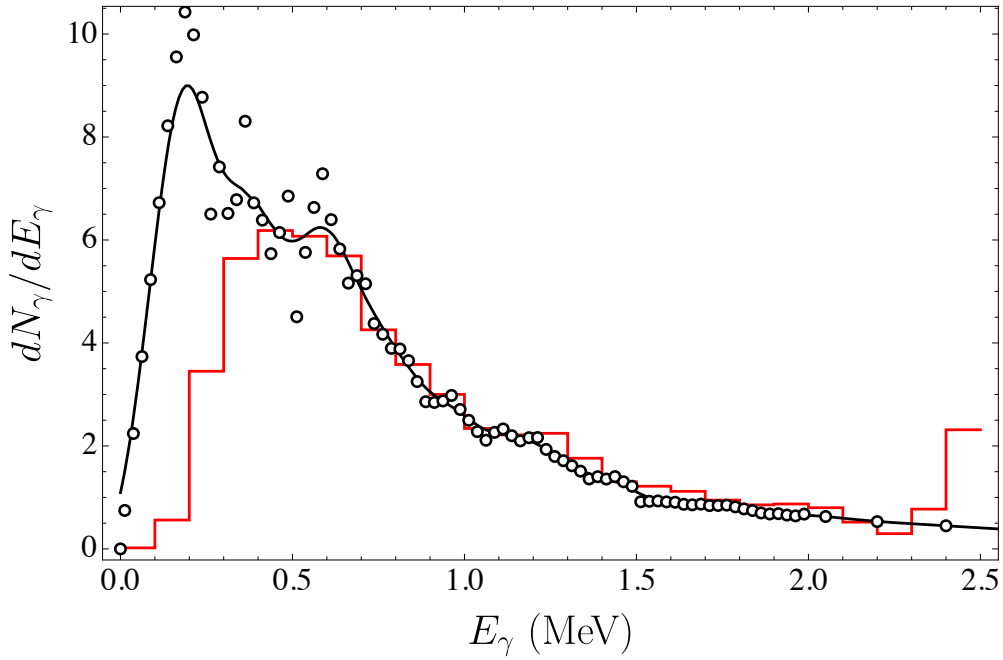

Figure 2.7: E_γ spectrum unfolding. Reference spectrum (black points), Gaussian-smoothed reference (black line), and unfolded spectrum (red histogram) in coincidence with one PPAC plate.

Special attention was given to the region at lower E_γ (< 1 MeV) since that is where most of the structure in the spectrum is expected. The difference between the unfolded spectrum and the reference for some E_γ bins, with centers ranging from 600 keV to 1.8 MeV in 300 keV steps, is shown in Fig. 2.8.

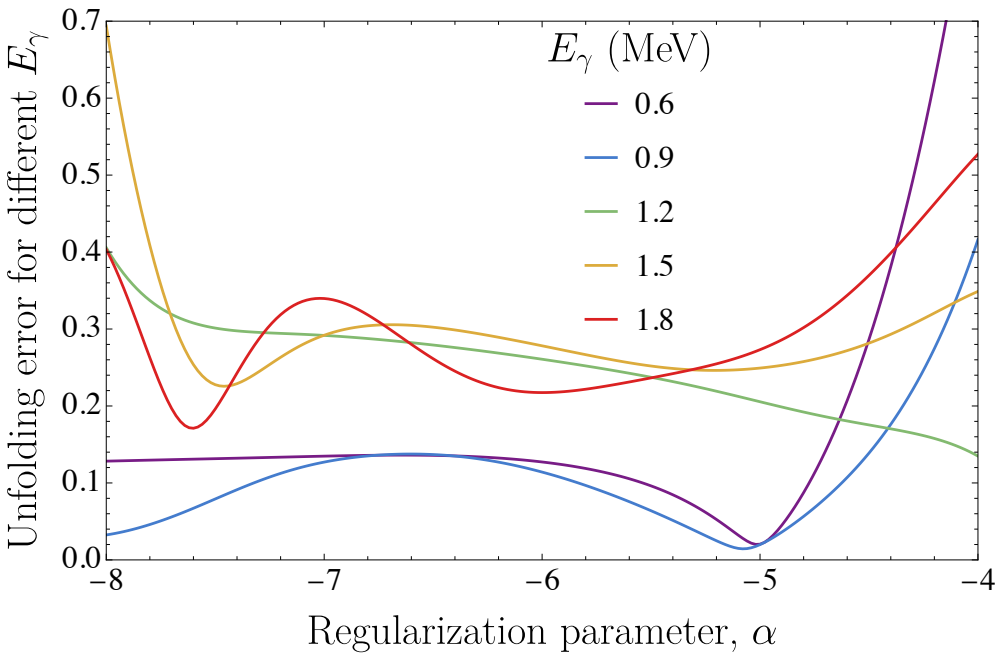

Figure 2.8: The effect of the regularization parameter, α, on the difference between the unfolded spectrum and reference spectrum. The square response matrix R is regularized before inversion by adding a scaled identity matrix, Γ: $R^{-1} \sim (R^T R + \Gamma)^{-1} R^T$. The E_γ bins are 200 keV wide.

The E_γ energy resolution, including both detector resolution and uncertainty introduced by the unfolding procedure, is $\approx 19\%$ in the analyzed γ-ray energy range. Based on comparison with the reference spectrum in Figs. 2.7 and 2.8 we chose $\alpha = 5.5$. We determined that the unfolding procedure reproduced the correct spectral shape and magnitude between $0.4 < E_\gamma < 2.2$ MeV. The measured γ-ray spectra for each E_i bin are shown in Fig. 2.9. This limitation is reflected in Fig. 2.9, where the hatched regions fall outside the acceptance window.

The $\overline{N}_\gamma$ reported throughout this chapter thus includes only γ rays within this acceptance window of $0.4 < E_\gamma < 2.2$ MeV, representing $\approx 60\%$ of the integrated ^{239}Pu$(n_{\text{th}}, \text{f})$ γ-ray spectrum above 0.1 MeV. Almost all of the remaining excluded γ rays fall below the acceptance region. We constructed a covariance matrix by varying the regularization parameter to estimate the unfolding uncertainty in $\overline{N}_\gamma$.

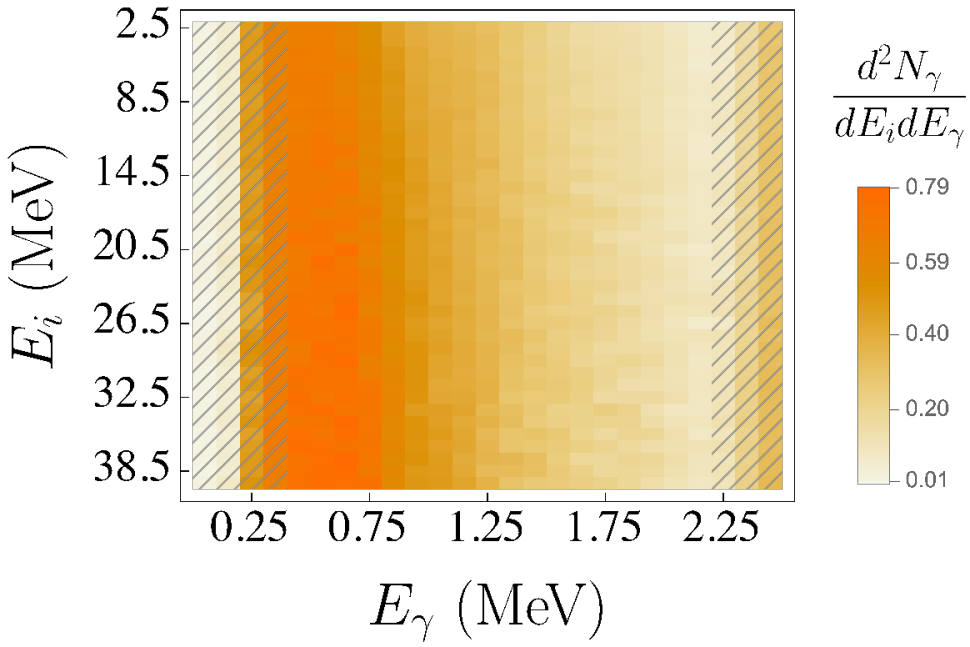

Figure 2.9: Measured γ-ray spectra for each quasi-monoenergetic incident neutron energy bin, E_i. The hatched regions fall outside of the E_γ acceptance window.

2.4 Fission Codes

The fission models CGMF [39], FIFRELIN [40], and FREYA [41] were employed to examine how different treatments of fragment initial conditions and particle emission affect the relationship between γ-ray emission and incident energy. All three codes use phenomenological models and while the underlying principles are sometimes similar, varying treatments of determining the initial fragment properties and their subsequent de-excitation can result in very different predictions of the γ-ray spectrum and multiplicity. We provide short descriptions of each model here, and point to suitable references for more details.

2.4.1 CGMF

CGMF [39] takes as input the pre-neutron fission fragment mass and kinetic energy distributions and samples from these distributions to determine the total excitation energy of

the fragments. This total excitation energy is shared between the fragments based on a mass-dependent nuclear temperature ratio law. The spin of each fragment is subsequently sampled from a spin distribution closely following Bethe's work [49], with a spin cut-off parameter (called B^2 in Ref. [39]) that depends on the moment of inertia of the fragment and is proportional to the fragment temperature. Note that B^2 includes an adjustable scaling factor that depends linearly on E_i and is used to tune the competition between neutrons and photons to fit experimental photon data. CGMF handles pre-fission neutron emission using probabilities calculated with the CoH_3 code [50].

CGMF implements the Hauser-Feshbach statistical nuclear reaction model to follow the de-excitation of fission fragments. It uses a spherical optical model potential to determine neutron transmission coefficients. γ-ray transmission coefficients are determined using the strength function formalism, where the continuum level density follows the Fermi-gas formula at high excitation energies and a constant-temperature formula at lower excitation energies. Discrete levels are imported from the RIPL-3 [51] database where available. More details on the specific models used, as well as a complete list of the input files required to run CGMF, are available in Table 2 of Ref. [39].

2.4.2 FIFRELIN

Similarly to CGMF, the pre-neutron fission fragment mass and kinetic energy distributions are used as inputs in FIFRELIN [40] and sampled, in order to calculate the total excitation energy of the fragments. FIFRELIN also employs an empirical mass-dependent temperature ratio of the fragments to partition the excitation energy between them, and the total spin of each fragment is statistically sampled following Bethe's work. Different models for the spin cut-off parameter can be used [52]; in the Inertia+Shell model used in this work, the spin cut-off depends on the mass, ground-state deformation, and temperature of the nucleus as well as shell effects. This model includes one free scaling parameter that is allowed to vary with E_x. Note that in FIFRELIN, the four free parameters are adjusted to reproduce

the total prompt neutron multiplicity in the JEFF-3.3 library [53]. In other words, there is no explicit dependence on experimental γ-ray data, including in the spin cut-off scaling parameter. FIFRELIN does not include pre-fission neutron emission.

FIFRELIN implements a coupled Hauser-Feshbach algorithm based on the concept of Nuclear Realization, established by Bečvář [54] and implemented by Regnier *et al.* [55] for neutron/γ/electron coupled emission from an excited nucleus. Neutron transmission coefficients are governed by optical model calculations. γ-ray emission is determined by the strength function formalism. Somewhat uniquely, in each realization an artificial set of levels is generated based on expected level densities, and the partial widths of a given transition energy are allowed to fluctuate [55, 56]. This strategy is potentially important for modeling γ-ray observables when the input nuclear structure data files are deficient [57].

2.4.3 FREYA

Just as in the previously mentioned codes the mass, charge, and total kinetic energy distributions of the fragments are sampled at the beginning of a fission event in FREYA [41]. The temperature sharing is directly specified by a free parameter. The spins of the fragments in FREYA are generated based on the "spin temperature," T_S, which is the temperature of the dinuclear system at scission multiplied by a free parameter, c_S. In FREYA, this free parameter does not depend on fragment mass or energy. Contributions from the dinuclear rotational modes available at scission—tilting, twisting, wriggling, and bending—are statistically populated based on this spin temperature [58]. This is in contrast to the previous two models, which sample the fragment spins based on the nascent fragment temperatures after they are separated. Prefission neutron emission is treated the same way as postfission neutron evaporation from the fragments.

The fragments de-excite via neutron evaporation with a black-body spectrum until the available intrinsic energy falls below the neutron separation energy. Statistical photons are then emitted with a black-body spectrum modulated by a giant dipole resonance form factor.

In FREYA, all statistical photons remove 1 $\hbar$ of spin. Once the excitation energy is sufficiently low, evaluated discrete transitions from the RIPL-3 data library [51] are used until the ground state or a sufficiently long-lived isomeric state is reached [59]. The free parameters in FREYA are summarized in Ref. [60].

2.5 Results

In Fig. 2.10, we present the relationship between $\overline{N}_\gamma$ and E_i between $2 < E_i < 40$ MeV. Our data show a clear increase in $\overline{N}_\gamma$ across the entire E_i range. Uncertainties include variation across PPAC foils and unfolding; statistical uncertainties are comparatively negligible. Also plotted in Fig. 2.10(a) are γ-ray multiplicities from the ENDF/B-VIII.0 evaluation [37] and data from Qi [33, 61] and Laborie [34]. These data are scaled down to match our $0.4 < E_\gamma < 2.2$ MeV acceptance region. We integrate the ENDF/B-VIII.0 ^{239}Pu(n,f) and ^{238}U(n,f) γ-ray spectra within our acceptance range, then again for a threshold $E_\gamma > 0.1$ MeV. Most of the experimental results are reported for a 0.1 MeV threshold and extend up to sufficiently high E_γ that their upper limit does not significantly affect $\overline{N}_\gamma$. Thus, the evaluation and experimental data in Fig. 2.10 are scaled down by the ratio of these two integrals for the appropriate reaction. Even with this correction, we do not necessarily expect the Qi ^{238}U(n,f) [33] and Laborie [34] data to agree with our data since they study a different reaction. The ENDF/B-VIII.0 points above thermal fission were inferred from total γ-ray production data, assuming a 20% uncertainty [48].

We note that $\overline{N}_\gamma$ varies linearly with E_i below the 2$^{\mathrm{nd}}$-chance fission threshold with a slope of $\Delta\overline{N}_\gamma/\Delta E_i = 0.085 \pm 0.010$ MeV^{-1}. This behavior was also observed by Gjestvang *et al.* in ^{240}Pu$(d,p\mathrm{f})$, where they found a slope of 0.08 ± 0.03 MeV^{-1}. Extrapolating this fit down to $E_i = 0$ yields good agreement with the well-studied multiplicity at thermal fission [62]. Uncertainty on the slope includes variation across PPAC foils, uncertainty from unfolding, and estimated variance of the fitted slope.

In Fig. 2.10(b), we compare our data to predictions from FIFRELIN and the release versions of CGMF and FREYA for $\overline{N}_\gamma$ within the acceptance window as a function of E_i. Only data below the second-chance fission threshold are shown for FIFRELIN, since it does not include pre-fission emission. CGMF predicts a similar trend, although the discontinuities at the n^{th}-chance fission thresholds are overemphasized compared to experiment. FREYA predicts about 0.5 too few γ rays within the acceptance region. The model uncertainties are statistical.

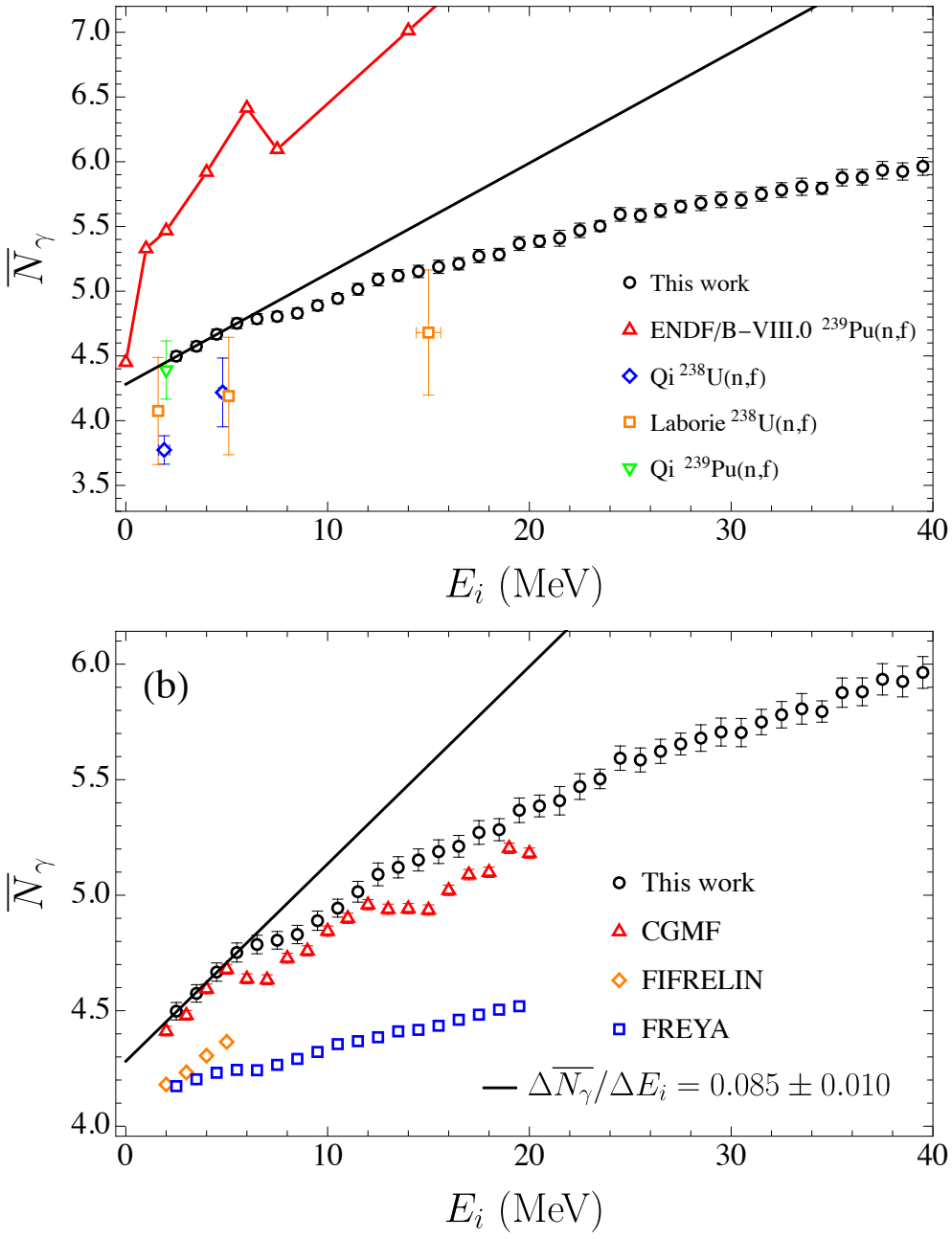

Figure 2.10: $\overline{N}_\gamma$ between $0.4 < E_\gamma < 2.2$ MeV as a function of E_i for $2 < E_i < 40$ MeV. Data where E_i is below the ^{240}Pu inner fission barrier height, $B_\mathrm{f} = 6.05$ MeV [51], are fit with a black line. The bin width is 1 MeV.

The neutron separation energies, S_n, of different fissioning isotopes can vary by several MeV so comparing γ-ray emission from different reactions at a given E_i is not always appropriate. It is instructive to instead look at the excitation energy of the fissioning nucleus,

E_x, which is independent of this variation. If we neglect the small kinetic energy imparted to the CN by the incident neutron, the excitation energy of the pre-fission ^{240}Pu* nucleus is

$$E_x = E_i + S_n^{(240)}, \tag{2.1}$$

where E_i is the incident neutron energy and $S_n^{(240)} = 6.53$ MeV is the neutron separation energy of the compound ^{240}Pu* nucleus. However, the E_x—and in fact, the isotope—of the CN just before fission cannot be uniquely determined once the incident neutron energy exceeds the fission barrier height, B_f, due to the presence of multi-chance fission and pre-equilibrium neutron emission. These processes are illustrated in Fig. 2.11 from Ref. [63].

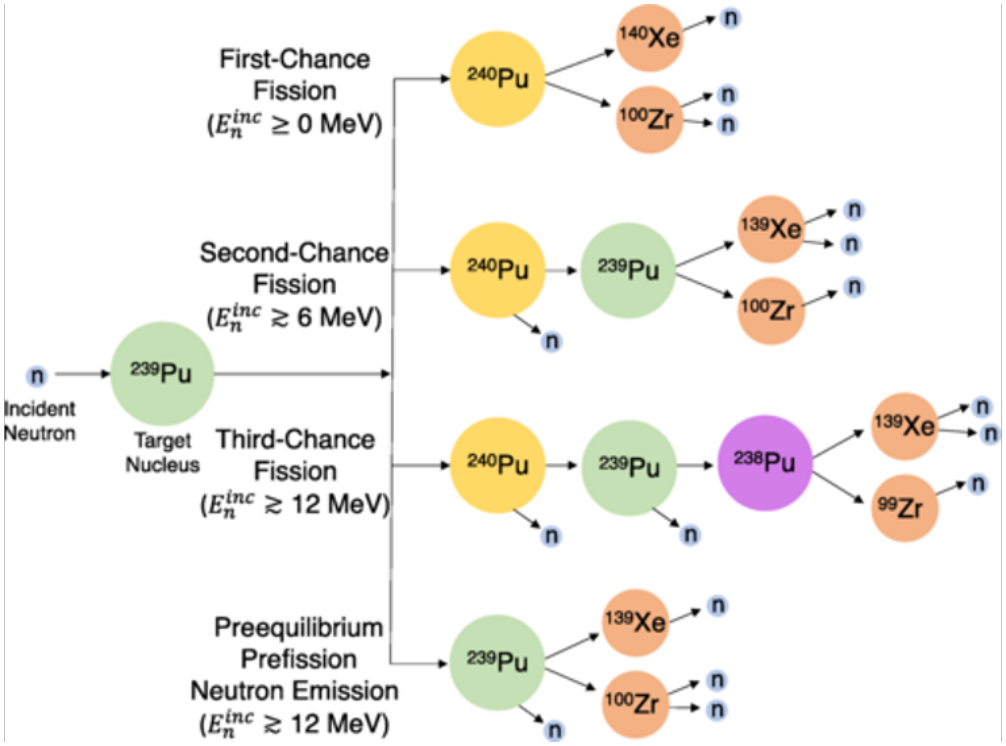

Figure 2.11: Diagram of fission channels with pre-fission processes, from Ref. [63]. It shows the reaction pathways that can lead to fission for different E_i. Note that the choices of fragments in the final states, and the number of neutrons they emit, are arbitrary.

Thus, multiple E_x values are possible for a given $E_i > B_\mathrm{f}$ and the average excitation energy, $\langle E_x \rangle$, of the fissioning nucleus is generally lower than what may be expected from

Eq. (2.1). At a fixed E_i, $\langle E_x \rangle$ can be written

$$\langle E_x \rangle = E_i + S_n^{(240)} - \sum_{j=1} \left[S_n^{(240-j+1)} + \langle k_j \rangle \right] p_j \tag{2.2}$$

where $S_n^{(240-j+1)}$ is the separation energy of the j^{th} neutron, $\langle k_j \rangle \equiv \langle k_j \rangle(E_i)$ is the average kinetic energy of the j^{th} pre-fission neutron, and $p_j \equiv p_j(E_i)$ is the probability of emitting j neutrons prior to fission. Note that Pu isotopes lighter than $^{240}\text{Pu}^*$ contribute to the total observed fissions when prefission neutron emission occurs. For compound nuclei that are close in mass, correlations between $\langle E_x \rangle$ and γ rays should be relatively independent of the isotope. $\langle k_j \rangle$ and p_j are model dependent; $\langle k_j \rangle$ was estimated using CGMF (see Fig. 2.12) and p_j was calculated using the ENDF/B-VII.1 cross sections [64] (see Fig. 2.13). We do not consider pre-equilibrium γ-ray emission since neutron-γ competition is minimal when E_x is high enough for pre-fission processes to occur [28, 65].

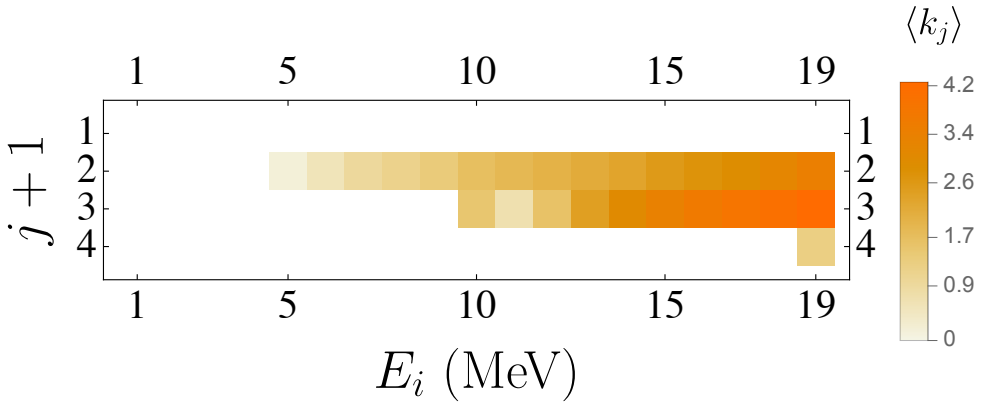

Figure 2.12: Pre-fission neutron energies from CGMF, $\langle k_j \rangle(E_i)$. The horizontal axis is the fission "chance" and the vertical axis is the incident neutron energy, E_i.

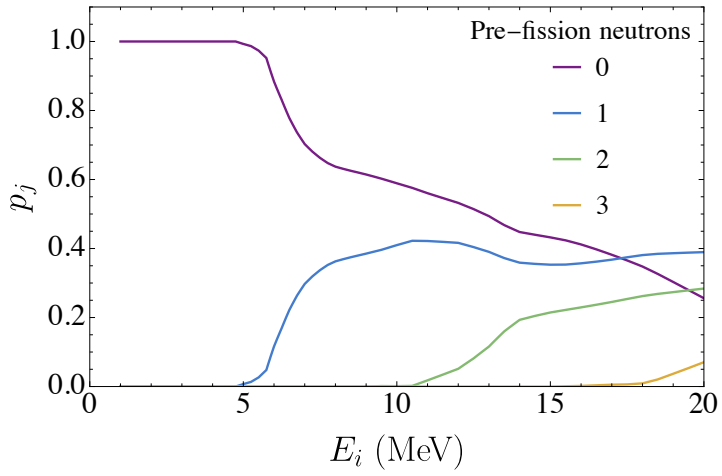

Figure 2.13: Probability of emitting j neutrons before fission as a function of E_i, based on ENDF/B-VII.1 cross sections.

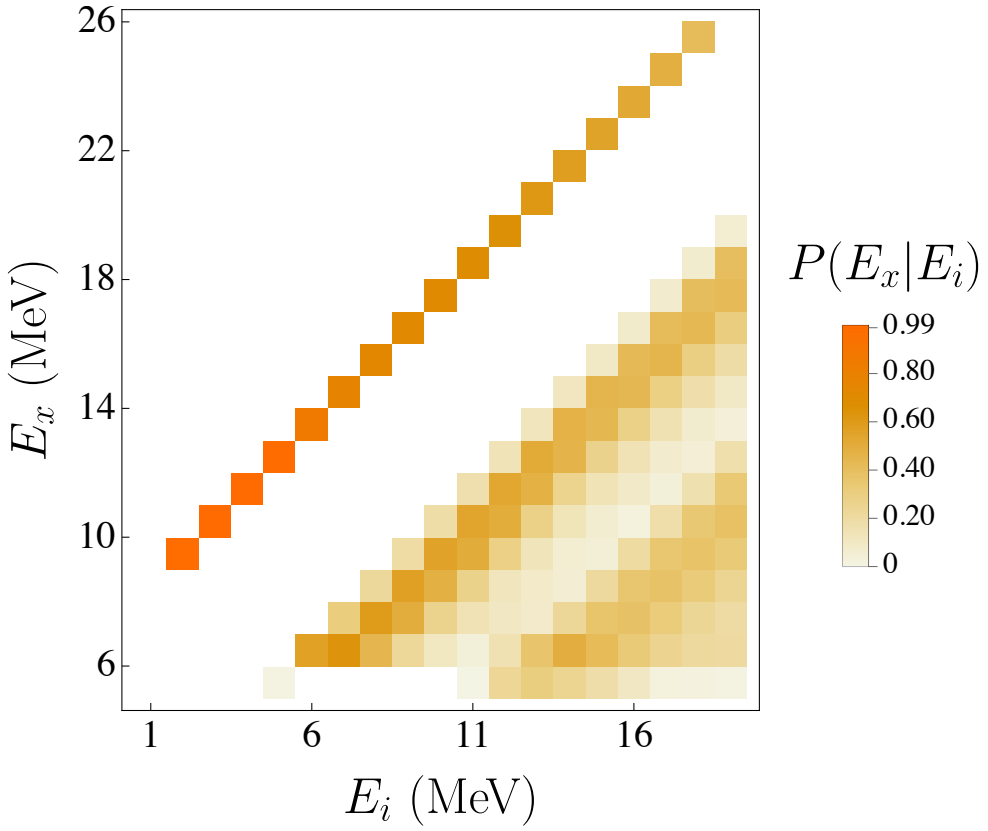

Figure 2.14: Possible E_x as a function of E_i. To obtain $\langle E_x \rangle (E_i)$, we take the average of the vertical slices.

E_x becomes a better description for the state of the CN just before fission once $E_i > B_\mathrm{f}$. To investigate the relationship between $\overline{N}_\gamma$ and E_x, in Fig. 2.15 we translate E_i to $\langle E_x \rangle$ using Eq. (2.2). This translation corrects for the effects introduced by pre-fission neutron emission and reveals the approximate linearity of $\overline{N}_\gamma$ with respect to $\langle E_x \rangle$ for $9 < \langle E_x \rangle < 19$ MeV. The model-dependent parameters p_j and $\langle k_j \rangle$ in Eq. (2.2) bias the translation, so we assign 10% uncertainties to p_j and $\langle k_j \rangle$ which give rise to horizontal uncertainties on the data. The models do not predict these values for $E_i > 20$ MeV, so the data above this limit are excluded from Fig. 2.15.

Also plotted in Fig. 2.15(a) are the ENDF/B-VIII.0 evaluation [37] and the Qi [33], Laborie [34], Rose [36], and Gjestvang [11] data. The energy transformation in Eq. (2.2) was also applied to the ENDF/B-VIII.0 evaluation. The incident energies of Qi and Laborie are shifted using Eq. (2.1) with the appropriate S_n for each reaction. The $E_i = 15.0$ MeV point from Laborie is omitted due to lack of nuclear data for determining p_j and $\langle k_j \rangle$ for $^{238}\mathrm{U}(n,\mathrm{f})$.

Our data agree well with other experiments in the limited range of overlap, although agreement with our extrapolation to lower E_x is mixed. We note in the cases of Rose [36] and Gjestvang [11] that some disagreement could arise from ion-induced fission populating different states of the CN [66, 67]. Recent theoretical work [58], however, concluded that the spin of the CN has little effect on the spins of the fragments, which would decouple the γ-ray multiplicity from the choice of reaction used to form the CN.

In Fig. 2.15(b) we compare our data to predictions from CGMF, FIFRELIN, and FREYA for $\overline{N}_\gamma$ within $0.4 < E_\gamma < 2.2$ MeV as a function of E_x. In CGMF and FREYA, simulated neutron-induced fission events were binned by CN excitation energy. The excitation energy of the CN was directly specified in FIFRELIN. Since FIFRELIN does not include pre-fission neutron emission, multi-chance fission does not occur and only $^{240}\mathrm{Pu}^*$ nuclei contribute. CGMF predicts the $\overline{N}_\gamma$ well across the entire $\langle E_x \rangle$ range—with some deviation at high $\langle E_x \rangle$, where we expect the energy translation in Eq. (2.2) be more uncertain.

CGMF agrees quite well across most of the energy range. FIFRELIN predicts the trend

well, although the absolute multiplicity within the acceptance region is too low by about 0.5 γ rays. FREYA underestimates the positive trend and multiplicity within our acceptance window, although it still predicts positive correlations. Statistical model uncertainties are shown, although they are smaller than the markers.

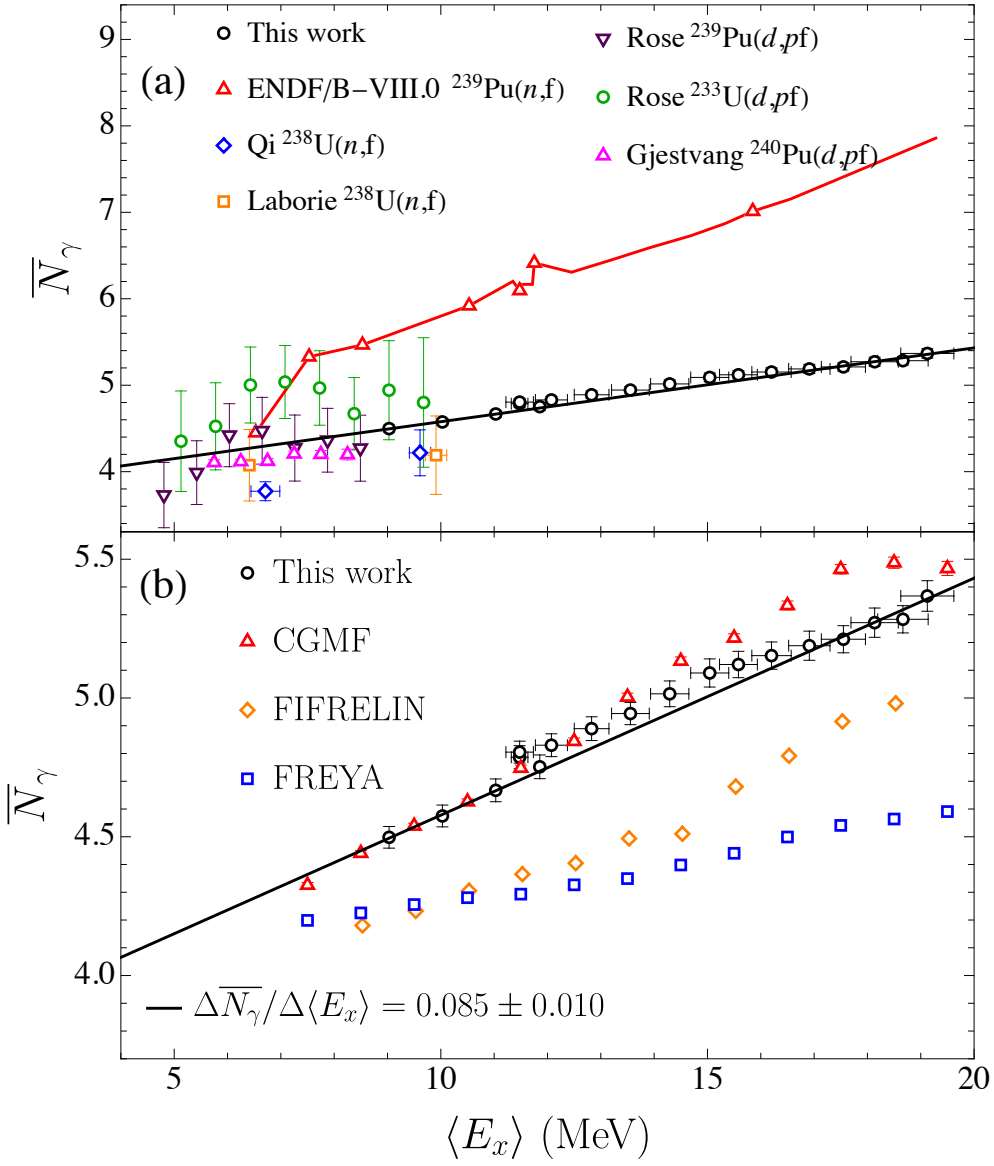

Figure 2.15: $\overline{N}_\gamma$ vs. average CN excitation energy. $\overline{N}_\gamma$ between $0.4 < E_\gamma < 2.2$ MeV as a function of $\langle E_x\rangle$ for $9 < \langle E_x\rangle < 19$ MeV. The black line is the same as in Fig. 2.10, shifted to the right by $S_n^{(240)}$, see Eq. (2.1).

We further characterize the additional γ rays we observe by examining how the spectrum

changes with increasing $\langle E_x \rangle$. We fix E_γ and determine the slope of a linear fit to $\overline{N}_\gamma$ with respect to $\langle E_x \rangle$, or $\Delta\overline{N}_\gamma/\Delta\langle E_x \rangle$, plotted in Fig. 2.17(a). The slopes of fits to the entire $\langle E_x \rangle$ range are plotted for each E_γ, as well as fits to just the data below the 2^{nd}-chance fission threshold, $E_i < B_\text{f}$, to provide a model-independent comparison. The uncertainties include unfolding uncertainty propagated from the covariance matrix and standard fit-parameter uncertainties. We note a particular enhancement around $E_\gamma = 0.7$ MeV, characteristic of $E2$ yrast transitions in the mass range of both light and heavy fragments. This enhancement accounts for the majority of the overall increase in $\overline{N}_\gamma$ with respect to $\langle E_x \rangle$, suggesting most of the additional γ rays observed at higher energies in Figs. 2.10 and 2.15 are $E2$ yrast transitions and remove $2\hbar$ of spin each. This can be seen in Fig. 2.16, where a large amount of the yrast transitions from $6^+, 8^+, 10^+$ states fall in this E_γ region. The measured γ-ray spectra for a few $\langle E_x \rangle$ values are also plotted in Fig. 2.17(a) using the right axis.

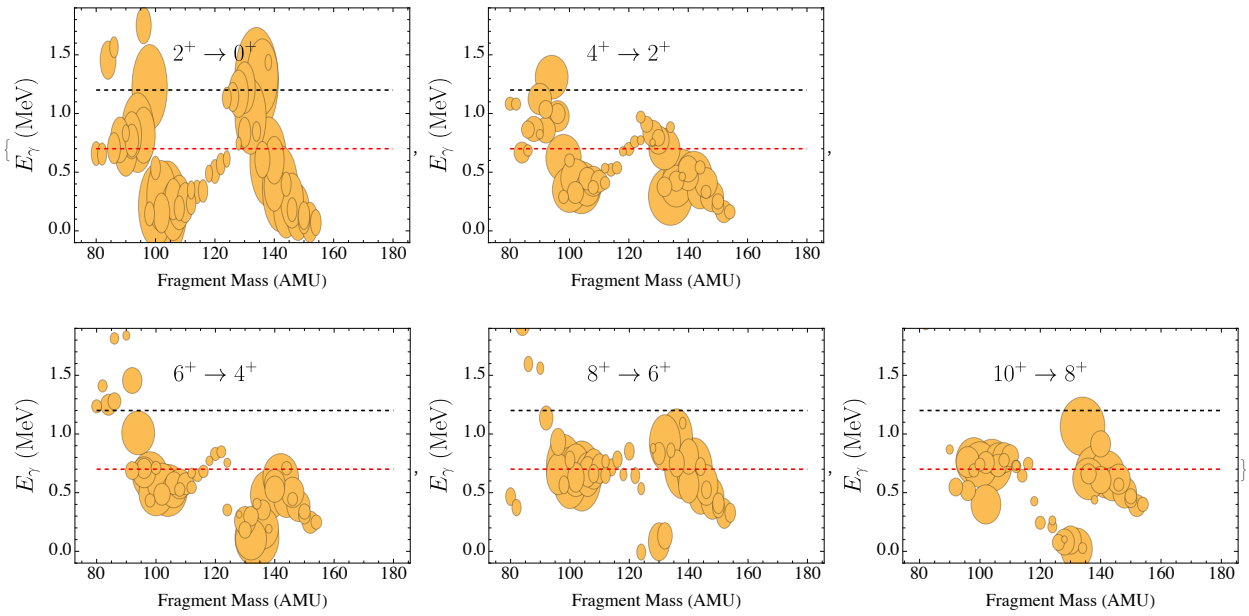

Figure 2.16: Yrast transition energies for even-even nuclei produced in ^{239}Pu(n,f). The marker sizes are proportional to the fragment yields from FIFRELIN.

In Fig. 2.17(b), slopes from fits to models are shown for comparison. The model uncertainties are standard fit-parameter uncertainties. CGMF agrees somewhat around the enhancement, but does not predict the dip around $E_\gamma = 0.5$ MeV that we observe in our

data. We observe good agreement with FIFRELIN using the Inertia+Shell spin cut-off model, which correctly predicts the magnitude of the enhancement around $E_\gamma = 0.7$ MeV. FREYA does not predict the observed enhancement around $E_\gamma = 0.7$ MeV. Most of the additional γ rays that it predicts lie below our acceptance region, explaining the discrepancy between FREYA and our data in Figs. 2.10(b) and 2.15(b). We believe that FIFRELIN agrees well partially because of its nuclear realization methodology, as it creates artificial levels in nuclei where compiled discrete level libraries like RIPL [51] are lacking.

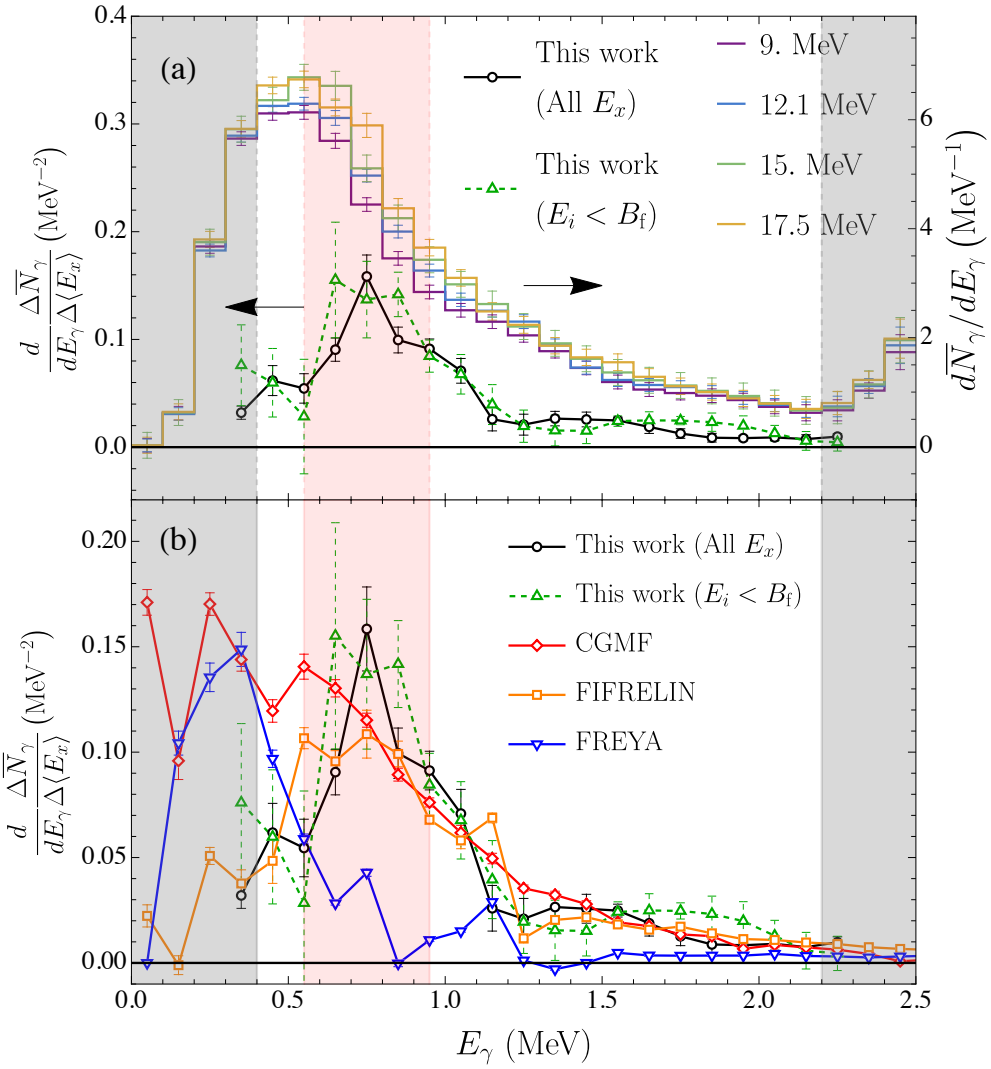

Figure 2.17: Dependence of the slope, $\Delta\overline{N}_\gamma/\Delta\langle E_x\rangle$, on E_γ. In (a), γ-ray spectra from the experiment for $\langle E_x\rangle = 9$, 12.1, 15, and 17.5 MeV are also shown on the right-hand side. The area outside the E_γ acceptance region is shown as the grey shaded region. E_γ bins are 0.1 MeV.

2.6 Discussion

To draw physical conclusions, we discuss the differences between models that cause FIFRELIN to agree well with our experimental data in Fig. 2.17. It is clear from this agreement that the energy-dependent spin distribution is one component of an accurate prediction. In contrast, resampling stages in FREYA eliminate the correlations between fragment excitation energy and the dinuclear temperature that is used to calculate the fragment spins. The disagreement between this experiment and FREYA could be due to this decoupling of spin and energy, although other differences in the models could contribute. CGMF's method for calculating the spin cut-off parameter is similar to that of FIFRELIN; the spin cut-off depends on the fragment's temperature and ground-state moment of inertia in the same way in both codes. The two agree well in magnitude around the enhancement, with the main difference being that CGMF predicts more low-energy γ rays while FIFRELIN and our experiment decrease at lower E_γ. Differences could arise from how the free scaling parameter is chosen. Free parameters in FIFRELIN are chosen solely to match experimental total neutron multiplicity data, while the spin cut-off scaling parameter in CGMF is fitted to total γ-ray energy and multiplicity data [39]. Given the similarity of their treatment, FIFRELIN's implementation of the Nuclear Realizations established by Becvar [54] could lead to more realistic modeling of discrete transitions in fragments with uncertain level schemes, and thus explain the better agreement at low E_γ. FREYA's methodology for selecting the initial spin of fragments is fundamentally different, although it results in similar average spin values. Recent work regarding the angular distribution of statistical γ rays [68] suggests that these transitions are not always stretched, and thus FREYA's treatment may lead to a reduction in fragment spin post-statistical emission. This effect could lead to the observed deficiency in yrast γ rays.

The fragment yield distribution also changes with excitation energy, and must be discussed. We examined the distribution of yrast γ-ray energies as a function of the changing fragment yield to determine whether the energy threshold could bias our results. We used

E_x-dependent fragment yields from FIFRELIN and discrete level libraries from NuDat 3.0 [69] to produce yield-weighted E_γ spectra for yrast band transitions. We found that the average energy of yrast transitions with certain initial spin values, such as $8^+ \rightarrow 6^+$ transitions, increases as E_x increases and fragment mass yield becomes more symmetric. However, these $8^+ \rightarrow 6^+$ transitions still lie within the E_γ acceptance region at low E_x, so we do not suspect the $\overline{N}_\gamma$ increase around $E_\gamma = 0.7$ MeV is due to the changing fragment yields. This conclusion is consistent with our agreement with FIFRELIN (Inertia+Shell), where we can examine specific fragments and observe positive correlations between the number of yrast band transitions, and E_x.

2.7 Conclusion

We have presented the first direct measurement of γ-ray multiplicity, $\overline{N}_\gamma$, for fast neutron-induced fission of ^{239}Pu, across a large incident neutron energy range, $2 < E_i < 40$ MeV. We observe a clear increase in $\overline{N}_\gamma$ over the entire range. We find an approximately linear relationship between $\overline{N}_\gamma$ and E_i below the 2$^{\text{nd}}$-chance fission threshold, with a slope of 0.085 ± 0.010 MeV^{-1}. This relationship is preserved upon translating incident neutron energy to CN excitation energy in the range $9 < \langle E_x \rangle < 19$ MeV. These extra γ rays are found around energies characteristic of stretched electric quadrupole transitions, experimentally confirming positive correlations between the excitation energy of the CN and the total spins of the fragments. This assertion is supported by comparisons with fission model calculations. While the trend appears linear in this E_x range, it is not necessarily incompatible with the statistical model of spin generation. A larger range in E_x, particularly lower in energy, must be explored to determine the functional form.

In future experiments, we plan to probe lower E_x, which will be more sensitive to the functional form of the spin dependence, by examining the relationship between γ-ray emission from ^{252}Cf(sf) and fragment mass, as well as total kinetic energy. We also suggest induced-

fission experiments with higher-resolution γ-ray detectors to resolve the low-energy region of the E_γ spectrum, as well as unambiguously identify known $E2$ transitions on an event-by-event basis. Such experiments will provide comparatively model-independent correlations between the spin distributions of fragments post-statistical emission, and their masses and excitation energies.

2.8 Contributions

Chapter 2 is based on the following article published in Phys. Rev. C:

> N. P. Giha, S. Marin, J. A. Baker, I. E. Hernandez, K. J. Kelly, M. Devlin, J. M. O'Donnell, R. Vogt, J. Randrup, P. Talou, I. Stetcu, A. E. Lovell, O. Litaize, O. Serot, A. Chebboubi, C.-Y. Wu, S. D. Clarke, and S. A. Pozzi, "Correlations between energy and γ-ray emission in ^{239}Pu(n,f)", Phys. Rev. C **107**, 014612 (2023)

Scientists at Los Alamos National Laboratory (including authors Keegan Kelly, Matt Devlin, and John O'Donnell) performed this experiment for the purpose of measuring the fission neutron energy spectrum as a function of incident neutron energy [38] and gave us the raw data for this analysis. Stefano Marin converted the raw list-mode data from the experiment into ROOT trees of fission events. With tips from the LANL team, Stefano, James Baker, and I developed the corrections for the α-pileup in the PPAC and neutron beam wraparound discussed later in the Chapter. Keegan Kelly provided an exceptionally detailed MCNP model of the Chi-Nu detector array, which I used to simulate the detector response on the Great Lakes HPC cluster at U-M. James led the construction of the analysis back-end that produced histograms and .csv files from the processed ROOT trees. I performed the last stages of analysis, as well as manuscript writing, with plenty of guidance from Stefano. A myriad of theorists helped interpret the experimental results: Ramona, Jørgen, Patrick, Ionel, Amy, and the Oliviers Serot and Litaize. Thank you to all who made this work possible.

CHAPTER 3

The TFGIC at Argonne: Detecting Fragment Properties in Coincidence with n/γ Emission

3.1 Introduction

In Chapter 2 we varied the energy available to the fission fragments by increasing the incident neutron energy. While effective at raising the overall excitation energy available to the fragments, the fission process muddies the connection between the excitation of the compound nucleus and the excitation energies of the fission fragments. For a given compound nucleus excitation energy, many different fission channels are possible [70]. Those channels will have different shapes at the scission point and lead to different fragmentations. As a result, the total energy available (Q of the reaction) and the amount that goes to the total fragment kinetic energy (TKE) will vary. In Chapter 3, we introduce an approach where we measure the fragments directly in coincidence with the particles they emit [8, 13]. The biggest advantage over the approach in Chapter 2 is direct access to the TKE and fragmentation, and thus more detail about the fission channel and total excitation energy (TXE) of the fragments. The relationship between spin and energy is therefore much easier to access and to quantify.

We built a twin Frisch-gridded ionization chamber (TFGIC) with two identical volumes separated by a common cathode. The TFGIC measures the kinetic energies of both fragments emitted back-to-back. From that information, we can reconstruct the fragment masses

and the angle that the fission axis makes with the symmetry axis of the TFGIC. These instruments have been used extensively on their own to measure fragment mass and TKE distributions [71]; here, we realize a "flange-less" design that minimizes the attenuating material, making our TFGIC well-suited to be placed inside detector arrays. During the commissioning and characterization of the TFGIC, we placed it inside FS-3 [72], an array of 40 ø2"×2" *trans*-stilbene organic scintillator detectors.

Frisch-gridded ionization chambers have been broadly used in nuclear physics applications, among them the measurement of fission fragments [73]. Arrays of organic scintillators have been used to simultaneously measure neutrons and γ rays emitted during the fission fragment de-excitation [8, 68]. Combining the two systems allows us to correlate the emission of particles with fragment properties such as masses, kinetic energies, and ultimately, excitation energies. We provide technical descriptions of the two instruments individually as well as the methodology and performance of the combined system. In Section 3.2 we provide details on the TFGIC and FS-3 detector systems, in Section 3.3, discuss the TFGIC analysis and resolutions, in Section 3.4 we show some results from the TFGIC+FS-3 experiment that validate our method, and conclude in Section 3.5.

3.2 Instruments

3.2.1 Twin Frisch-gridded ionization chamber (TFGIC)

TFGICs have become popular in fission studies since they are straightforward to build and operate and can provide a complete measurement of the fragments: their energies, masses, and directions [74]. There is an extensive literature describing their function and modes of operation [8, 73, 75, 76]. The TFGIC design used in this experiment was inspired by the design by Dana Duke [71], with a few significant modifications to the vacuum chamber surrounding the detector and the readout boards to reduce the attenuation of neutrons and γ rays.

A CAD drawing of the TFGIC is shown in Fig. 3.1. The fragment detector is composed of two identical volumes enclosed between the central cathode plate and the two anode plates. The inner diameter of the chamber is 140 mm and the distance between cathode and anode boards is 47 mm. Each anode and its associated circuitry are combined in a single printed circuit board (PCB). Similarly, the cathode and the associated electronic circuitry, as well as the preamplifiers for all the TFGIC signals, are contained on a single PCB. To minimize neutron and γ-ray attenuation, the anodes' circuit boards are used to enclose the chamber volume, thus avoiding the use of metal flanges.

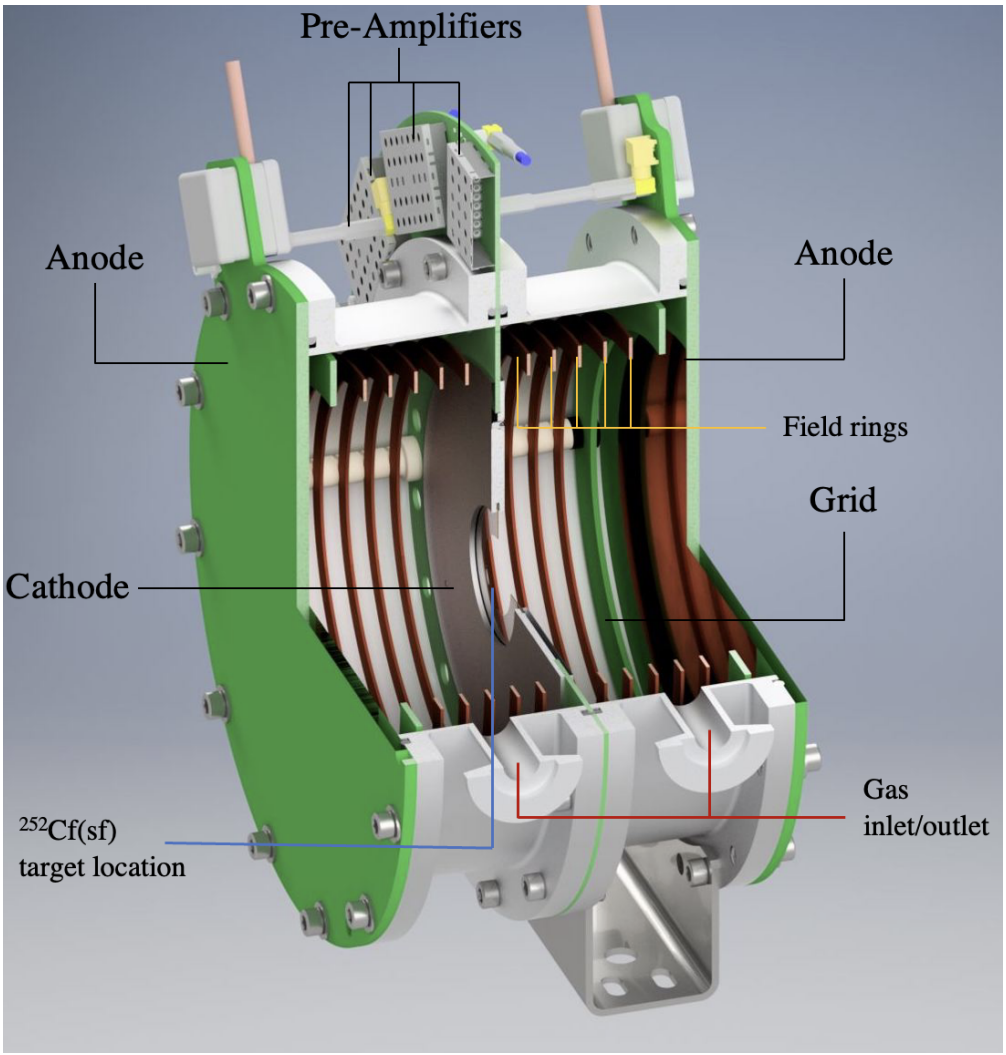

Figure 3.1: CAD diagram of the TFGIC.

Frisch grids are used in ionization chambers to eliminate the geometric dependence of the anode signal, and to improve the time resolution of the detector [77]. We use the conventional approach of using the ratio of grid to anode signals to extract the polar angle of emission of fragments with respect to the chamber axis. The grids are made of 20 μm gold-plated tungsten wires spaced 1 mm apart and soldered to PCB disks. These grids are placed between the cathode and each anode at a distance of 7 mm from the anode.

The anodes are 4 layer PCBs constructed from FR4 laminate substrate with an active area diameter of 108 mm. The anodes are 3.175 mm thick to support operation with a differential working pressure of up to 0.3 atm. The anode uses 28.3 g copper, 34.8 μm thick, on the outer conductive surface that is finished with an electroless nickel immersion gold (ENIG) process. A guard ring energized to the same potential as the anode surface encircles the anode to improve field uniformity at the edge of the anode's active area. Each anode provides a shielded high voltage (HV) hookup that includes an HV filter, signal decoupling capacitor, and the necessary biasing resistors for the anode and its guard ring. The anode signal is connected via a short $\sim$ 5 cm cable to the preamplifier located on the cathode. Collecting all the preamplifiers on the cathode board keeps them in close proximity, while simplifying the electronics and cabling, and also allows the anode design to be modified and swapped out more freely than if they were directly on PCB.

The ionization chamber volume is filled with P-10 gas, Ar(90%)+CH_4(10%) at 950 torr with continuous flow of $\sim$ 100 cc/min. Each section of the twin chamber has a gas port, which are respectively used as inlet and outlet. To facilitate the gas circulation between the two sections, 8 holes of 6.5 mm diameter are located on the cathode board on the opposite side of the gas ports. The gas pressure is monitored, and variations on the order of 10 torr have been observed, but the electrodes' signals were not significantly influenced by these small variations.

The TFGIC detector volume is electrified by holding the cathode at a potential of -1500 V, the two grids grounded at 0 V, and the anode plates at +1000 V. These voltages were

provided by CAEN N1470 power supplies. The produced electric field is rectified and made uniform across the chamber with copper field rings, five in each chamber section. The field rings are held by three PEEK columns that are mounted directly on the cathode board.

The Gmsh finite-element mesh generating software [78] was used to develop the geometry and to perform a mesh generation throughout the volume of the ionization chamber. Due to the symmetry, only half of the chamber is used for modeling the detector. The uniformity of the electric field inside the chamber was investigated using the Elmer finite-element software [79] and a previously generated mesh. The electrostatic problem is defined by assigning the dielectric properties of the materials in each sub-volume. The calculated magnitude of the electric field and orientation inside the detector are shown for two cases with (Fig. 3.2, left) and without (Fig. 3.2, right) field rings.

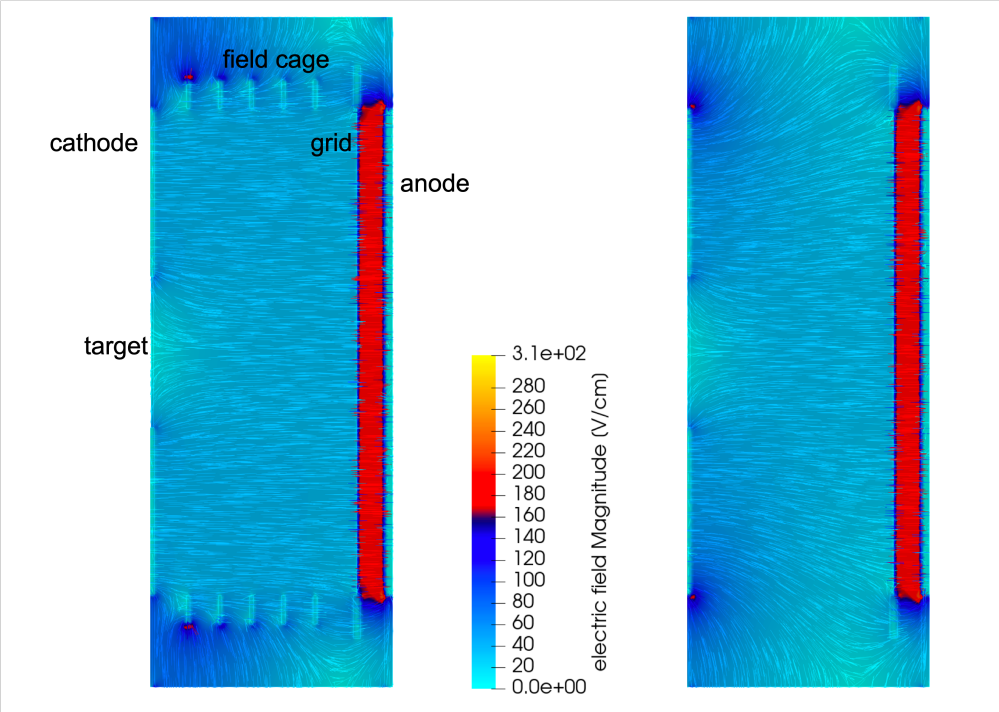

Figure 3.2: Calculated magnitude of the electric field with (left) and without (right) field cage rings.

The five signals generated by the TFGIC: one cathode, two grids and two anodes, are passed through Cremat CR-110 preamplifiers mounted directly on the cathode board, outside

of the aluminum walls of the chamber. The preamplified signals have a short rise time, around $200 - 250$ ns, and a long decay time of 150 μs. The grid signals are digitized using a CAEN V1740D, 64-channel digitizer, with 12-bit resolution over a 2 V dynamic range and a 62.5-MHz sampling rate. The signals from the anodes and the cathode are cloned using a CAEN N454 fan-in/fan-out module, with one of the copies of each channel being digitized in the V1740D. Clones of both anode signals are provided in channels 0 and 1 of the three V1730 digitizers, for coincidence purposes. A clone of the cathode signal is provided to one of the V1730 digitizers, also used as the FS-3 signal digitizers, where a digital CFD algorithm determines its timing. We have determined a time resolution of $\approx 5 - 6$ ns FWHM between the chamber and a stilbene detector based on the broadening of the γ-ray coincident timing spectrum. Another copy of the cathode signal is provided to an oscilloscope for use as a diagnostic.

We have designed an aluminum bracket and holder system that allows the chamber to be vertically repositioned and rotated. The chamber was aligned such that the ^{252}Cf(sf) target was at the geometric center of the FS-3 array, and the axis of the chamber—the line of shortest distance between cathode and anode—was pointed in the direction of one of the *trans*-stilbene detectors.

A spontaneous fission source was prepared by molecular plating of 9 kBq of ^{252}Cf on a ~ 100 μg/cm^2 carbon foil at Oregon State University. The diameter of the deposit on the backing is 10 mm, and it was determined that the source was geometrically offset by about 2 mm with respect to the center of the carbon foil. This offset was deemed negligible, since this distance is much shorter than both typical fragment ranges and the dimension of the detector active volume.

Data were collected from the detectors and TFGIC only when signals from both anodes were observed in coincidence, *i.e.*, the trigger condition. This coincidence AND logic significantly lowers the background, and virtually eliminates the α-particle background, as can be determined by pulse-height spectroscopy and comparison of the chamber throughput to the

nominal source activity.

3.2.2 FS-3 array

The FS-3 detector array, shown in Fig. 3.3, consists of forty organic scintillator detectors arranged in spherical configuration. Each detector consists of a 5.08 cm by 5.08 cm right circular cylinder *trans*-stilbene crystal manufactured by Inrad-Optics to our specifications [80]. Each crystal is optically coupled to a ElectronTube 9214B photo-multiplier tube (PMT), and is individually wrapped in insulating tape and teflon to reduce optical noise, and mu-metal to reduce the effects of external magnetic fields. Finally, the assembly is placed inside a 3-D printed case, which further reduces optical noise and makes it easier to handle.

Figure 3.3: The FS-3 detector array at Argonne National Laboratory. The TFGIC is shown in the center of the array. Also visible (background, right) is the electronic readout and high-voltage supply.

The detectors are arranged in a spherical configuration, with detector holders placed around three concentric rings. The rings are held in place by adjustable aluminum columns, so the height of the detector array can be changed. The support structure allows each detector to be placed at a variable distance from the center of the source, independently from one another, from a minimum of 14 cm between the center and detector face, up to 27 cm. An intermediate distance of 22.5 cm was used in the present experiment. A detailed model of the detectors, the aluminum structure, and the surrounding room was generated in MCNPX-PoliMi [46, 81]. The FS-3 detectors are individually powered by seven CAEN

V6533 negative polarity power supplies. The power supplies are connected via USB to the DAQ, and are operated using the CAEN GECO2020 control software. The HV on each PMT is adjusted to calibrate all detectors on the Compton edge of a ^{137}Cs source. The calibration was repeated daily, but only minor corrections on the order of 2% were observed after the detectors reached thermal equilibrium. The signal of each detector is individually digitized with CAEN V1730 digitizers, with 500 MHz digitization rate, and 2 V dynamic range. Each digitizer reads out 16 channels, and three V1730 digitizers were used in this experiment. The three digitizer clocks are synchronized with one another and with the clock of the V1740D digitizer collecting the TFGIC data.

3.2.3 DAQ and signal processing

The FS-3 detector signals are analyzed on the digitizer boards using charge integration. The time integral of the voltage signals is proportional to the light output generated by the interaction. The total light output is calibrated using the Compton edge of ^{137}Cs, which provides a conversion of the light output to energy deposited. We measure light output in units of eV electron-equivalent, or eVee. The protons that are scattered in neutron interactions generate significantly less scintillation light and a greater portion of this light is produced as delayed scintillation [82]. By comparing the amount of scintillation light produced a few ns after the interaction, more characteristic of delayed fluorescence, to the total light output, we can distinguish interactions caused by γ rays and neutrons on an event-by-event basis. This procedure is known as pulse shape discrimination (PSD). A PSD plot is shown in Fig. 3.4. We have written an algorithm that computes the optimal discrimination as a function of the total light output, and we optimized the region of integration for the tail of the pulse, where delayed fluorescence is expected to be stronger.

A threshold of 50 keVee is applied to the scintillator signals. This threshold results in a γ-ray incident-energy threshold of γ-ray of 0.15 MeV and a larger neutron threshold of approximately 0.5 MeV. The larger neutron threshold results in a bias in this experiment to

observe neutrons of higher energies.

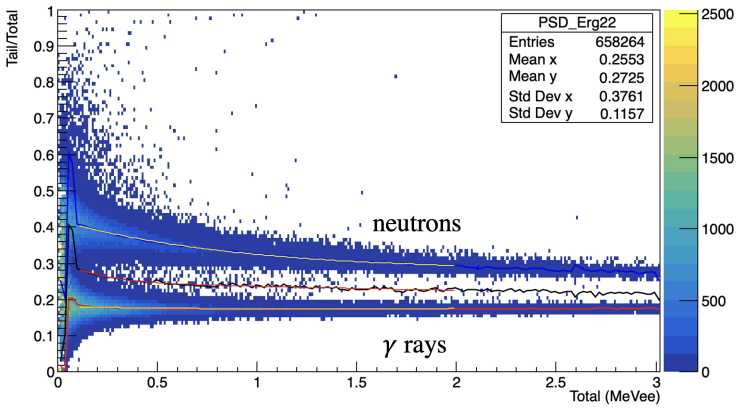

Figure 3.4: Neutron and γ-ray PSD from one of the detectors in FS-3. Neutrons (top) and γ rays (bottom) separate into two bands when we take the ratio of the integral of the tail of the scintillation pulse to the total integral. An energy-dependent discrimination line is shown between the two distributions.

The system's time resolution is good enough for time-of-flight (ToF)-based particle classification and, to a limited degree, for neutron spectroscopy. The ToF distribution of the measured particles, with respect to the measured cathode time, is shown in Fig. 3.5. The simultaneous use of both PSD and ToF for particle classification results in a negligible misclassification rate. The neutrons that arrive the earliest, simultaneosuly with γ rays, are also the most energetic neutrons, the easiest to discriminate using PSD.

3.3 Analysis

We analyze the TFGIC signals using the $2E$ method, which determines the masses of the fission fragments based on the measurement of the two fragment kinetic energies and the conservation of linear momentum. The $2E$ procedure has been presented in several past publications; in the following we will briefly summarize the main analysis steps, and focus on the improvements we have performed with this procedure. We include a diagram of the TFGIC in Fig. 3.6 and example waveforms from the electrodes in Fig. 3.7. We refer the

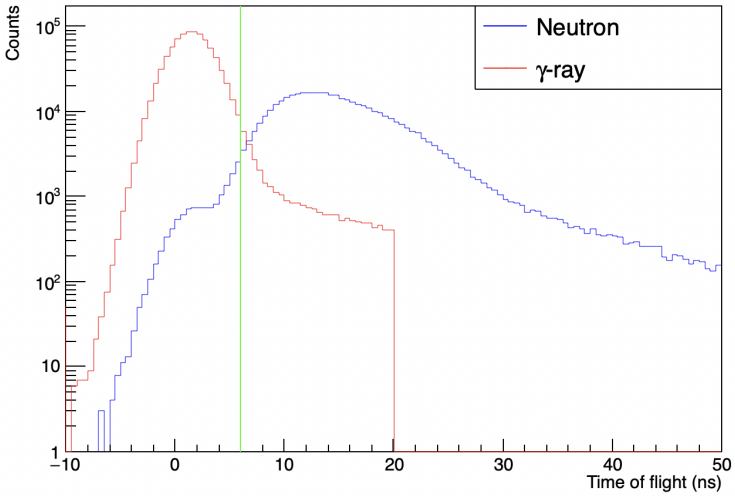

Figure 3.5: Time-of-flight distribution from the TFGIC to a detector in FS-3. Neutrons and γ rays are discriminated based on both PSD and ToF. Limited neutron ToF spectroscopy can be applied to the measured neutrons. The vertical green line, at 6 ns shows the timing separation between γ rays and neutrons.

reader to Refs. [8, 71, 83, 84] for detailed descriptions of this technique.

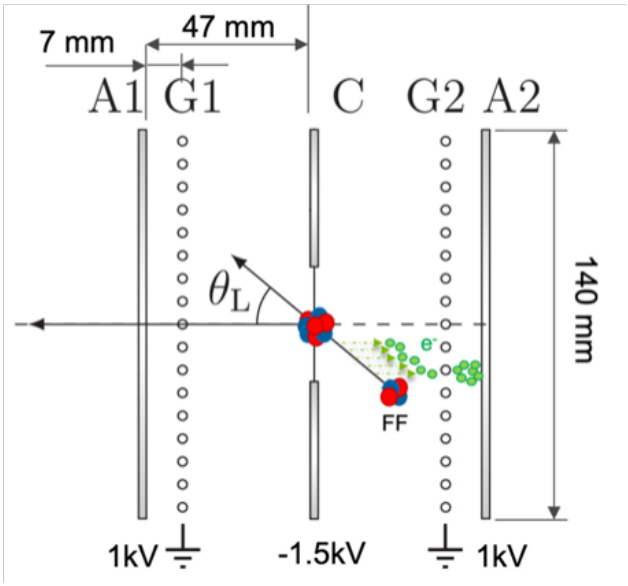

Figure 3.6: A simplified diagram of the TFGIC, taken from Ref. [10]. The fission source is mounted in the cathode (C) plane and the fragments are emitted back-to-back in volumes 1 and 2, each with their respective grids (G1,2) and anodes (A1,2).

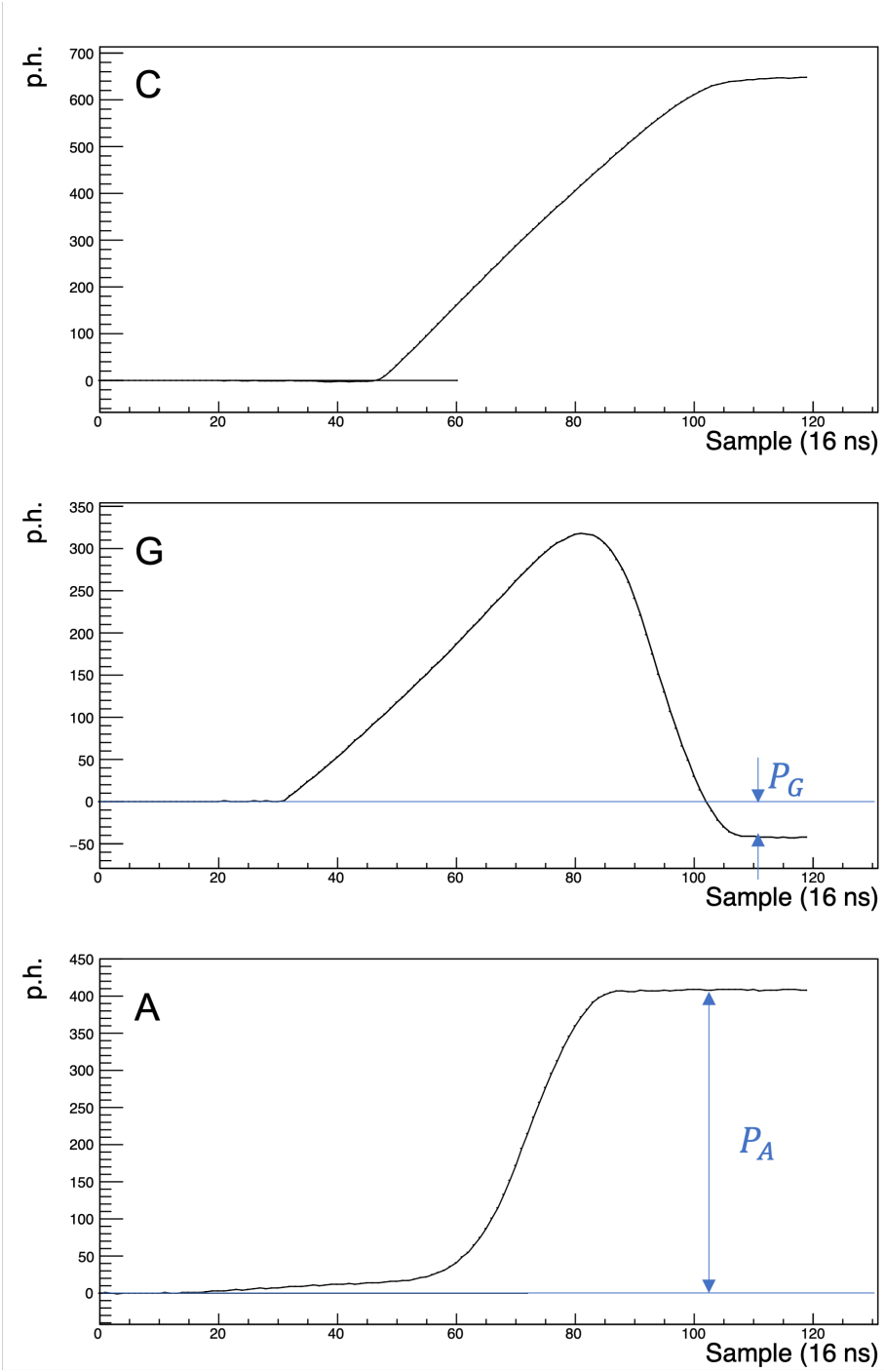

Figure 3.7: Example cathode (C), grid (G), and anode (A) waveforms from the TFGIC. The horizontal axis is in units of digitizer period (16 ns) and the vertical is in digitizer units. P_A and P_G are the reconstructed heights of the anode and grid waveforms—their ratio is proportional to the angle that the fission axis makes with the chamber axis, θ_L in Fig. 3.6.

The analysis begins with the reconstruction of the fission fragment kinetic energy from

the anode signal. The stray signal induced on the anode by charges drifting between cathode and grid, visible between about 20-35 units in the third panel of Fig. 3.7, is an effect known as grid inefficiency [8]. It is corrected for by comparing the event-by-event signals of anode and grid from the same side of the chamber. Secondly, the energy lost by the fragments in the carbon backing and within the source deposit itself is estimated. This estimate depends on the reconstructed fragment angle, as determined from the ratio of grid signals to anode signals [73]. We find that the average anode pulse height correlates approximately linearly with $(\cos\theta)^{-1}$, for both sides of the chamber, see Fig. 3.8.

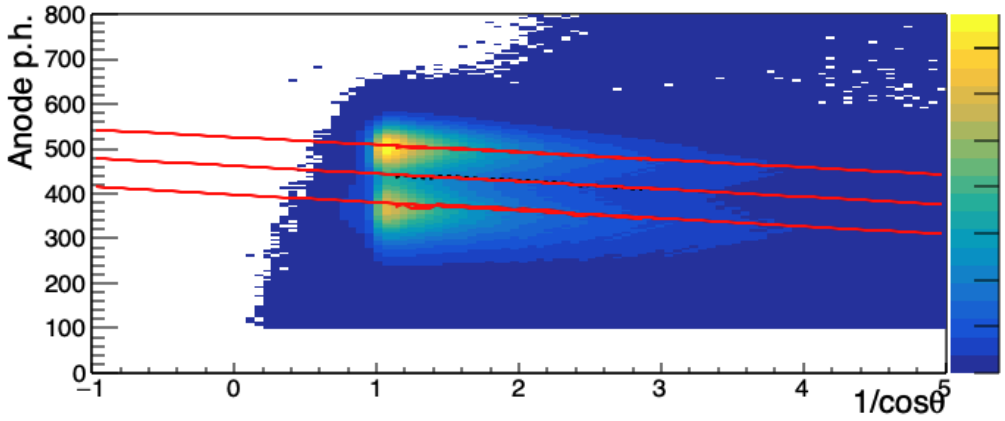

Figure 3.8: Attenuation of fragment kinetic energies as a function of $(\cos\theta)^{-1}$ for the source-side anode.

This relationship is expected if we assume that the energy lost by the fragments in the sample and backing is proportional to the distance traveled within the material. By extrapolating the linear relation to its y-intercept, which represents a vanishing material thickness, we estimate an angle-dependent energy loss. This quantity is added back on an event-by-event basis to the fission fragments, depending on their angle of emission.

The fragment masses are found by conservation of linear momentum, which requires the two fragments to have equal and opposite momenta in spontaneous fission. This relation dictates that the ratio of fragment kinetic energies is inversely proportional to the ratio of their masses. Because the total nucleon number of the system is known, up to the few neutrons emitted before the fragments are measured, the individual fragment masses can

be estimated. However, fragments lose kinetic energy via non-ionizing collisions in the P-10 gas as well, an effect known as pulse-height defect (PHD). The PHD correction, taken from Ref.[85] is independent of the angle of fragment emission and it only requires the mass estimated by the $2E$ method. We do not use an energy-dependent PHD, but instead use an average value over the fragment energies. Finally, the fragment masses are recursively determined by calculating, at each step in the recursion, the mass- and energy-dependent neutron multiplicity [8] and PHD.

The quantities of interest we want to extract from the ionization chamber are the yield observables: the fragment masses, A, and the total kinetic energy release, TKE. However, while not directly reported, the angle of emission of the fragments with respect to the TFGIC cylindrical symmetry axis is an important auxiliary variable in the analysis of fragment features. Specifically, the fragment angle determines the corrections that need to be applied to correct for the attenuation of the fragments in the target backing.

The fragment angle-of-emission can be determined by the ratio of the signal induced on the grid to the signal induced in the anode. Thus, the angle can be determined independently by each side of the fission chamber. Because fragments in spontaneous fission are emitted back-to-back, the variations between the two independent measurements can be used to assess the resolution of the TFGIC to the fragment direction. Fig. 3.9 shows the difference between the angle determined from the two sides of the chamber. An angular resolution of 0.11 FWHM in cosine bins was determined, approximately 27 degrees. However, by combining the information from both sides of the chamber, the angular resolution can be reduced by half.

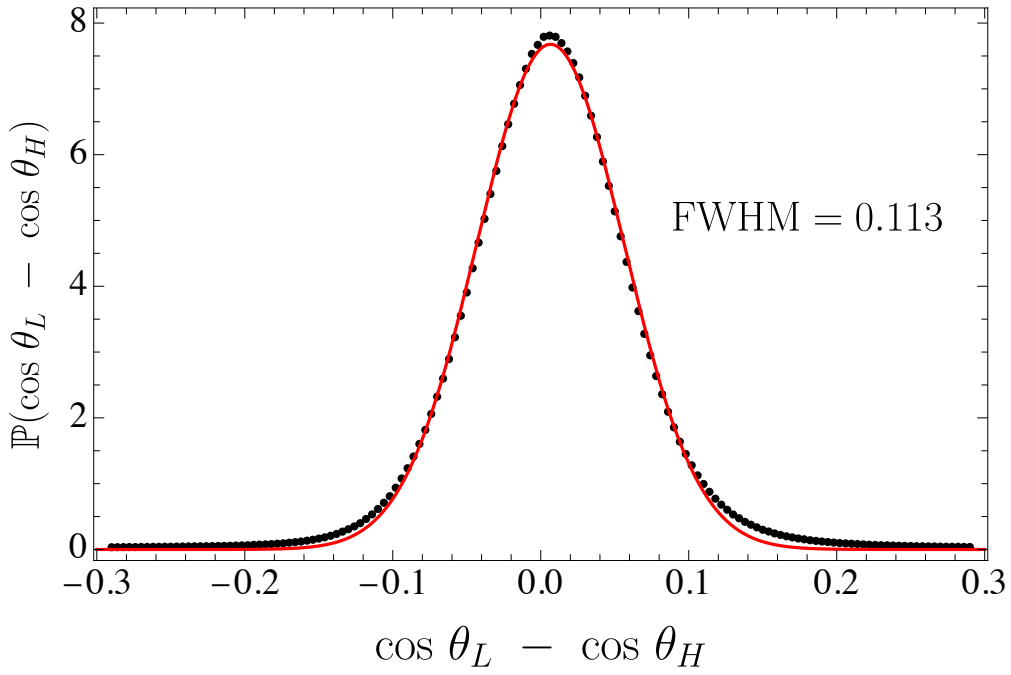

Figure 3.9: Angular response of the TFGIC. The difference between the angles determined by either side of the chamber would ideally be identical. The width of this distribution is indicative of the angular resolution of the TFGIC. The red line is an illustrative Gaussian fit applied to the data

The kinetic energy of fission fragments is determined primarily by the signal induced on the anodes. These signals are corrected for grid inefficiencies, the angle-dependent energy loss in the ^{252}Cf sample, and its backing, and the pulse height defect in P-10. The kinetic energy is further corrected by reconstructing the energies prior to neutron emission using the mean value $\langle N|A, \mathrm{TKE}\rangle$ determined by Göök *et al.*[8]. However, the mass A is determined by comparing the fragment kinetic energies, and thus masses and kinetic energies are simultaneously determined in a recursive loop, as explained above. The recursive loop was interrupted when masses differed by less than 0.2 % between iterations.

Due to the large attenuation of the fragments in the target and its backing, we find that data still contain angle dependence in the kinetic energy distributions, even after these effects are addressed with the method indicated in Ref. [71]. To avoid these problems, we selected a narrow range of emission angles, $|\cos\theta| > 0.9$, where the angle is determined from the arithmetic average of the angles determined from each side independently.

The mass measured by the TFGIC is shown in Fig. 3.10, where it is compared to the data obtained by Göök *et al.*[8]. We note that because of symmetry, we only need to plot the yield as a function of the light fragment mass since the same yield would be observed for the complementary of pre-emission masses $A_0 - A$, where $A_0 = 252$ is the fissioning nucleus mass number. The agreement between the two experiments is quite good across the mass yield, with some deviations in the symmetric fission region above $A \approx 120$. Our distribution is slightly larger than the one inferred by Göök *et al.*, indicating a worse mass resolution.

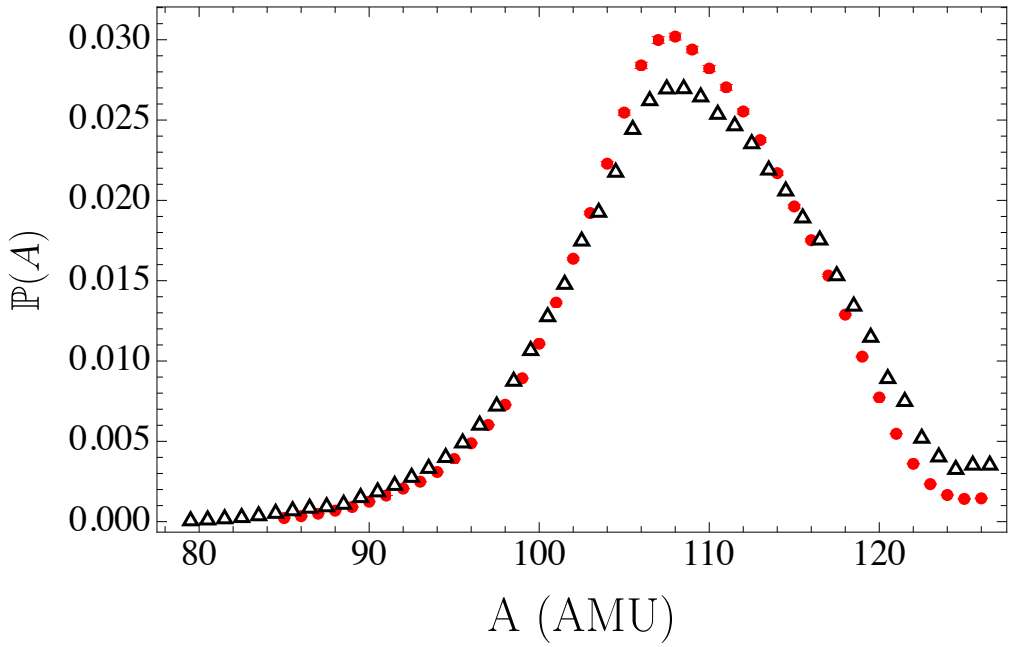

Figure 3.10: Fragment mass response of the TFGIC, black points (triangle), compared to the yield determined by Göök *et al.*, shown as red points (circle).

Using the setup in Chapter 4 with Gammasphere [86], we were able to directly measure the mass resolution of a TFGIC for the first time. By gating on two γ rays in the $^{1}44$Ba cascade (199-keV ($2^+ \rightarrow 0^+$) and 331-keV ($4^+ \rightarrow 2^+$) and fitting the observed fragment masses, we extract a mass resolution of 5.9 amu FWHM.

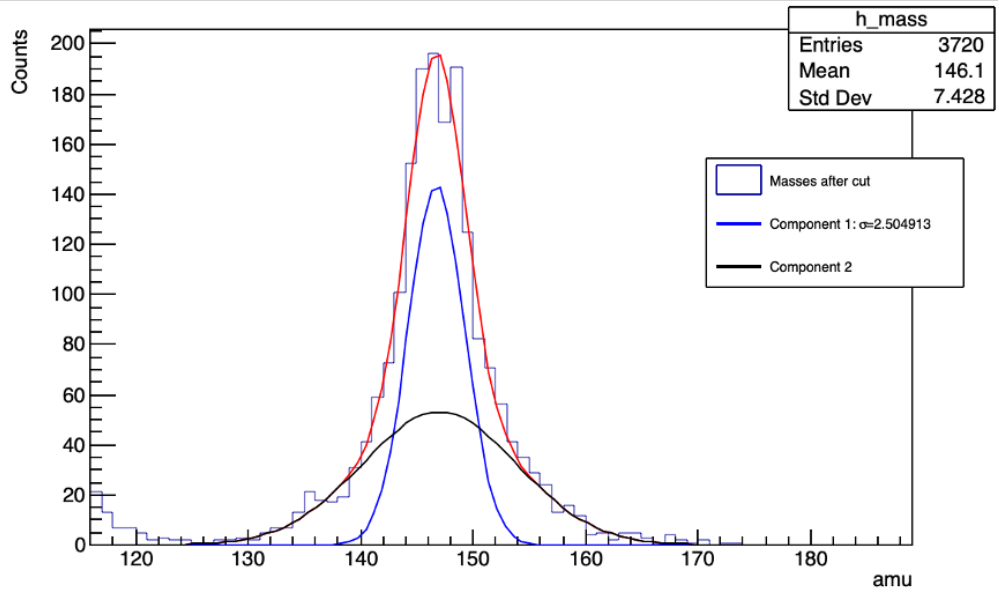

Figure 3.11: Measurement of TFGIC (post-neutron) mass resolution for ^{144}Ba.

The fission TKE, conditioned on the light fragment mass is shown in Fig. 3.12. The figure shows both the mean and the standard deviation of the determined kinetic energy release, with the former indicative of the accuracy of the TFGIC, and the latter indicative of its kinetic-energy resolution. The determined mean $\langle \mathrm{TKE}|A\rangle$ was found to be in good agreement with Göök *et al.*, with slight deviations at $A \approx 120$ and $A < 95$. The width of the TKE distribution is comparable to the reference experiment throughout most of the mass yields, but it is larger near symmetric fission. These results indicate a kinetic energy resolution of approximately $3-4$ MeV FWHM.

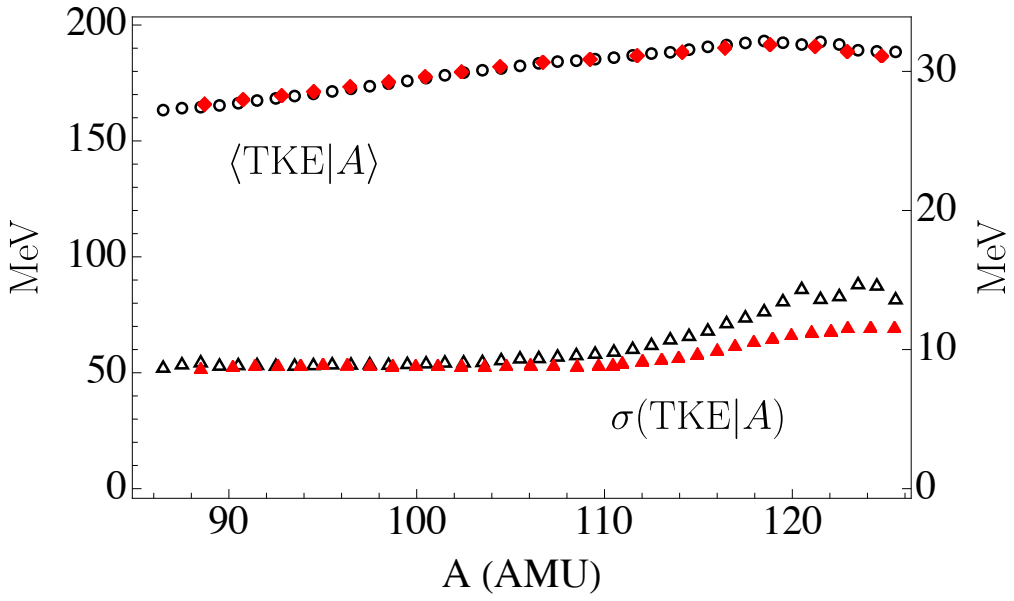

Figure 3.12: Average and standard deviation of the TKE distribution determined by the TFGIC, black points, compared to the yield determined by Göök *et al.*, shown as red points.

3.4 Results

As an illustrative example of the results that this combined system can produce, we present here the conditional differentiation of neutrons and γ rays with respect to total kinetic energy and fragment mass, in Figs. 3.13 and 3.14 respectively. On the same figures as our experimental results, we compare the neutron emission results to Göök *et al.* [8] and Travar *et al.* [9], for neutrons and γ-ray results, respectively. Both of these previous results used a very similar setup, employing a TFGIC in coincidence with radiation detectors, but only one particle type was analyzed in each of those experiments. The results of this comparison show that due to the resolution achieved by our system so far, slightly larger than the resolutions achieved by Göök *et al.*, the features of the multiplicity distributions are slightly broadened, and the correlations of particle multiplicities with fragment masses and kinetic energy are slightly weakened.

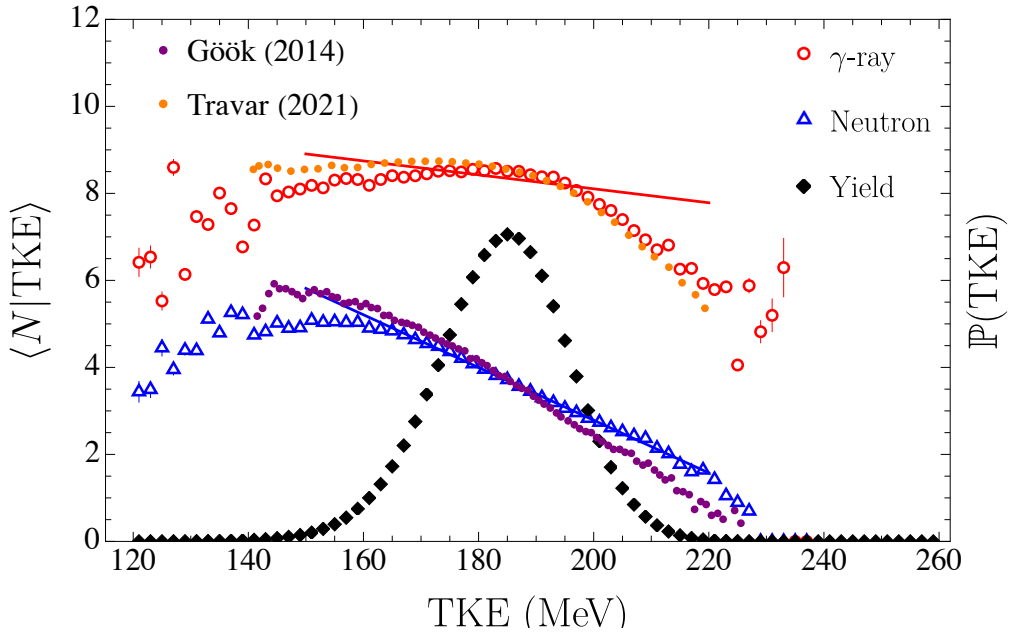

Figure 3.13: Total neutron- and γ-ray-multiplicity dependence on fragment TKE, compared to previous work by Göök *et al.* [8] and Travar *et al.* [9], respectively. The measured TKE yield is shown in black.

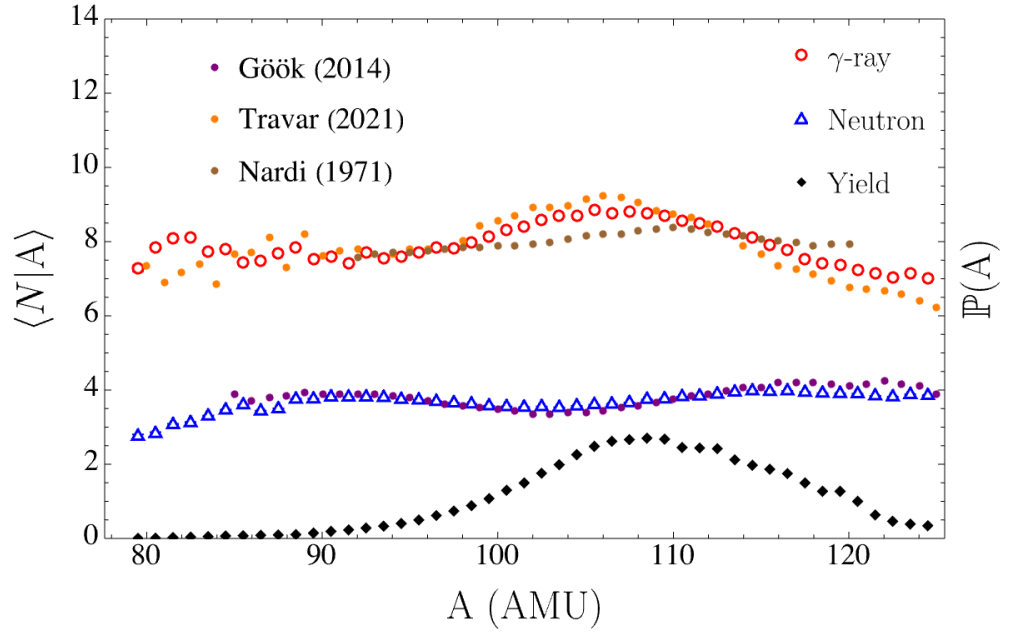

Figure 3.14: Total neutron- and γ-ray-multiplicity dependence on the light fragment mass, compared to previous work by Göök *et al.* [8] and Travar *et al.* [9], respectively. The measured mass yield is shown in black.

When conditioned on TKE, we observe the same behavior already observed by Travar *et*

al., the γ-ray multiplicity increases with decreasing TKE until TKE $\approx$ 180 MeV, below which the γ ray multiplicity stops growing and levels off, and even starts to slightly decrease.

While improvements can still be made to the fragment detection system, the results shown in Figs. 3.13 and 3.14 illustrate that coincident measurements of neutrons, γ rays, and fission fragments are possible with the system presented here.

3.5 Conclusion

The TFGIC+FS-3 experimental setup we presented in this Chapter was used to analyze the event-by-event n-γ emission correlations in fission in coincidence with measurements of fragment masses and excitation energy [10]. These results provide insight into the questions of fragment spins, the dependence of spin on mass and TKE, and spin polarization relative to the fission axis. This system improves on the current available technologies by greatly increasing the number of available detectors, forty in this experiment, and by simultaneously gaining access to both neutrons and γ rays in coincidence with fragments.

In Chapter 4 we perform a measurement at the Argonne National Laboratory ATLAS facility with the TFGIC inside Gammasphere [86], an array of Compton-suppressed, high-purity germanium detectors, to obtain detailed spectroscopic and angular information correlating γ rays with fragment properties. The TFGIC+Gammasphere combined system marries the capabilities shown in this Chapter with high-resolution γ-ray spectroscopy. As is discussed in Chapter 4, this enables (i) the identification of fragment Z and (ii) measurement of spin distributions.

In the future, we plan to segment one of the anodes of the TFGIC to obtain a measurement of the azimuthal angle of the fission axis, completely constraining its direction. This iteration of the TFGIC, coupled with both measurements within FS-3 and Gammasphere, will yield some of the most complete data on fission correlations to date. In particular, this segmentation could improve the event acceptance rate in the TFGIC+Gammasphere

configuration by as much as 10×. In future research, we also plan to use these instruments to investigate the event-by-event n-γ correlations in neutron- and photon-induced fission, leveraging the recent investigation of fragment yields in these reactions [87–89].

3.6 Contributions

Chapter 3 is based on the following article published in NIM:A:

> S. Marin, I. A. Tolstukhin, N. Giha, M. Oberling, R. Knaack, B. Kay, D. Duke, K. Montoya, D. Connolly, W. Loveland, A. Chemey, S. Pozzi, and F. Tovesson, "Instrumentation for correlated prompt n-γ emission studies in coincidence with fission fragments", Nuclear Instruments and Methods in Physics Research Section A: Accelerators, Spectrometers, Detectors and Associated Equipment **1048**, 168027 (2023)

The building of the chamber described in Chapter 3 was made possible by the Low Energy Technical Support team at Argonne National Lab. I did not help design the chamber—Michael Oberling designed the printed circuit boards, Russell Knaack designed the hardware components and all of the mounting equipment, Ivan Tolstukhin performed the electric field simulations, and Stefano performed n/γ attenuation simulations. Matt Gott loaded the first two ^{252}Cf sources, and Claus Mueller-Gatermann loaded the last and most nerve-wracking, which was used in Chapter 4. Walt Loveland and his team at Oregon State University prepared all three ^{252}Cf(sf) sources. And of course, Fredrik Tovesson made sure that all of this work could happen.

For the rest of this 2022 experimental campaign, Stefano and I worked together with he as the leader and I the protégé. We spent many hours at Argonne working on the waveform processing codes (sped up tremendously by Dana Duke, who shared her scripts from LANL with us), implementing the $2E$ method, and combining the fragment data with those from the FS-3 array. We spent what felt like even longer building and debugging the chamber,

and wondering where it all went wrong when we turned it on and didn't see fragments. It turns out, we had flipped the cathode during the first ^{252}Cf source installation such that the cathode vents were right next to the gas in/outlets in Fig. 3.1. We had to wait several days for the air impurity in the P-10 fill gas come down to a manageable concentration—mostly by diffusion due to the mistake—to see fragments. Stefano, Ivan, and I were involved in running the experiments after everything was set up.

Stefano wrote the original manuscript that was the basis for this Chapter. I've made changes and additions to add new information that was not available when the manuscript was published, to provide more information on the chamber and how it relates to Chapter 4, and to suit my style preferences.

CHAPTER 4

TKE-Dependence of Spin with the TFGIC+Gammasphere

4.1 Introduction

The analysis in Chapter 2 attempted to form a connection between γ-ray multiplicity and rough spectral features, and the spins of the fission fragments. While they are undoubtedly positively correlated, any conclusions made with γ-ray multiplicity data on E^*, J correlations are necessarily model-dependent. In contrast, the experiment in Chapter 4 allows us to find the spin distribution of specific fission fragments in a nearly model-independent way. After neutron and statistical γ-ray emission, which we argued in Chapter 1 does not dissipate a significant amount of spin, the fragments decay toward the ground state by emitting γ rays of characteristic energies. These γ rays can be discerned thanks to the excellent energy resolution of Gammasphere, then correlated with the kinetic energy and mass measurements from the TFGIC to quantify E^*, J correlations for specific fission fragments.

This experiment was designed to yield perhaps the most complete data set of fission events yet. Combining three detector systems, it is sensitive to all of the prompt particles emitted in fission: (i) the TFGIC [90] provides a fission trigger measurements of fission fragment masses, kinetic energies, and direction, (ii) Gammasphere [86] provides high-granularity, high-resolution γ-ray energy measurements, and (iii) the FS-3 [91], an array of ø2" × 2" *trans*-stilbene organic scintillators, provides neutron detection and time-of-flight

spectroscopy capabilities. It is an incredibly rich data set with myriad eventual uses. This Chapter focuses on measuring correlations between the fragment properties and the γ rays measured in Gammasphere.

We investigate correlations between the spin and energy generated in fission for ^{144}Ba, a fragment commonly produced in ^{252}Cf(sf) and fission of other actinides. We simultaneously measure prompt fission γ rays—believed to carry most of a fission fragment's spin—and total kinetic energy (TKE) of the fragments. Leveraging the spectroscopic capabilities of Gammasphere, we measure the intensities of known transitions and infer the relative initial population of several low-lying discrete nuclear levels in ^{144}Ba, as a function of TKE.

We describe the experiment in Section 4.2 and the analysis in Section 4.3. In Section 4.4, we present the average spin of ^{144}Ba as a function of TKE, $\langle I \rangle$(TKE). We discuss the implications of this result in Section 4.5 and conclude in Section 4.6.

4.2 Experimental setup and procedure

For the experiment, we combined a twin Frisch-gridded ionization chamber with Gammasphere to measure both fragments and γ rays. The setup is rendered in Fig. 4.1.

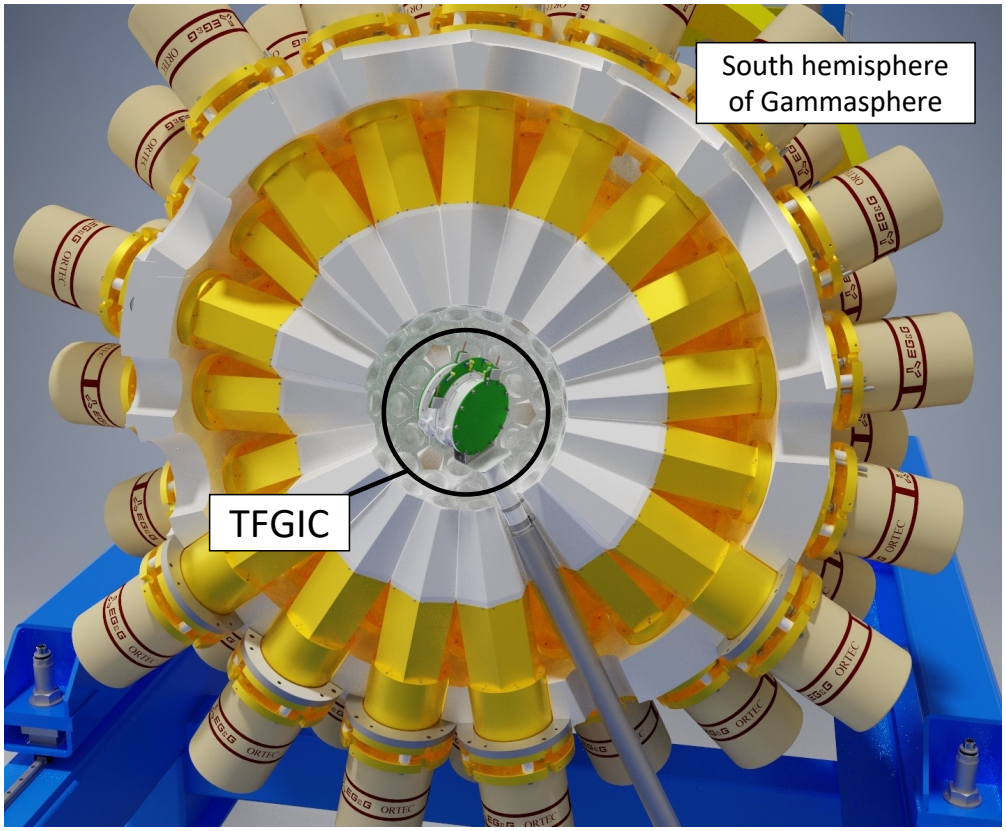

Figure 4.1: Rendering of the TFGIC inside Gammasphere.

The twin Frisch-gridded ionization chamber (TFGIC) at Argonne National Laboratory (ANL) [90] consists of two identical volumes enclosed between the central cathode plate and the two anode plates. The inner diameter of the chamber is 140 mm, and the distance between the cathode and anode boards is 47 mm. Frisch grids are positioned between the cathode and each anode at a distance of 7 mm from the anode. The TFGIC was loaded with a $\sim 4,000$ fissions/s ^{252}Cf spontaneous fission source deposited on a 100 μg/cm^2 carbon foil and placed inside the Compton-suppressed high-purity germanium (HPGe) detector array Gammasphere [86] at the Argonne Tandem Linear Accelerator System (ATLAS) Facility at ANL. The setup enabled simultaneous measurement of (i) both pre-neutron fission fragment masses $A_{L,H}$, kinetic energies $KE_{L,H}$, and the fission axis orientation with respect to TFGIC axis $\cos\theta_{\mathrm{f}}$ and (ii) the energies E_γ and angles of prompt γ rays emitted following fission.

The TFGIC was centered inside the array with the Gammasphere Universal Laser Align-

ment Gauge (GULAG) [92] such that the target was at the center of Gammasphere. The central axis of the TFGIC was aligned such that it would pass through the center of two of the HPGe ports, marked in green in Figures 4.2 and 4.3. This detector pair (ports C7 and C30 in the engineering drawings) was chosen so that an unbroken ring of HPGe detectors, sharing a common plane that intersects the center of Gammasphere, could be formed. Twelve ø2" × 2" *trans*-stilbene detectors, marked in orange, were placed around these two central HPGe detectors for neutron sensitivity. They are not included in the analysis in this Chapter.

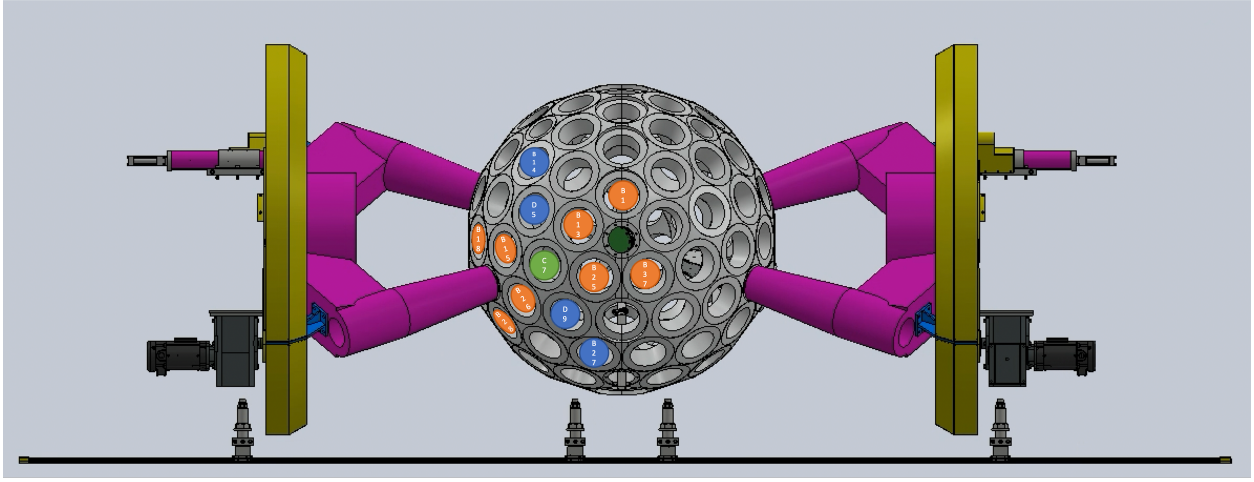

Figure 4.2: Front side of Gammasphere. Green ports are HPGes along the TFGIC axis. Orange ports are stilbenes. Blue and unlabeled ports are either filled with an HPGe detector, or are left empty.

4.2.1 Data acquisition

The data acquisition for this experiment necessitated the syncing of two separate digitizer systems: the digital data acquisition for Gammasphere (DGS) for the Gammasphere detectors and the "CAEN stack" for the TFGIC and stilbene detectors.

The signals from the Gammasphere detectors were read out with its DAQ system [93], consisting of 12 VME crates, each with 4 digitizer boards (10 channels, 14 bit, 100 MS/s). DGS was operated in triggerless mode, wherein all events which surpass the discriminator

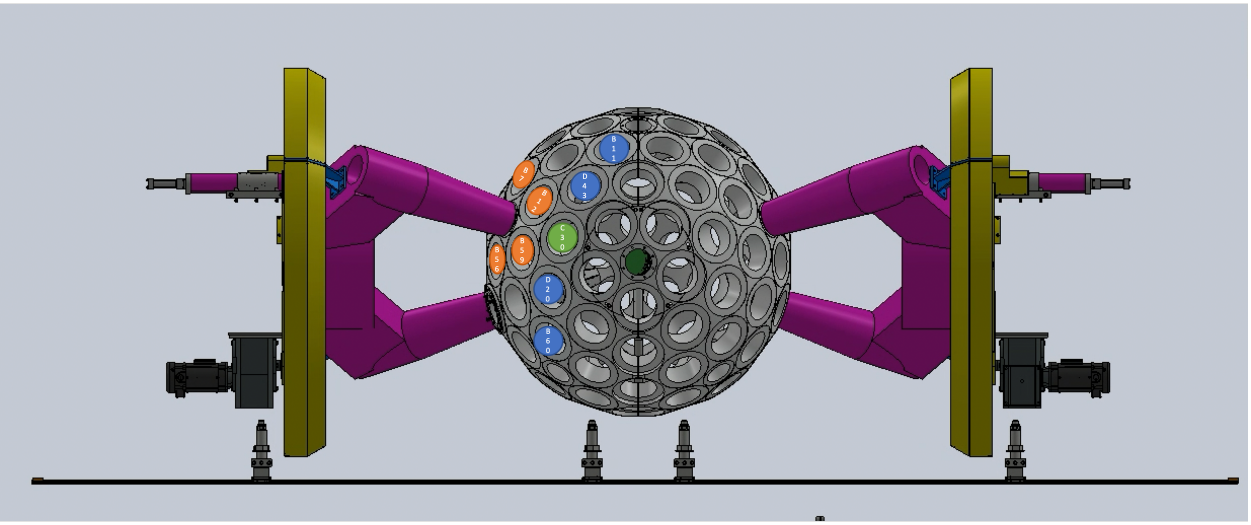

Figure 4.3: Back side of Gammasphere. Green ports are HPGes along the TFGIC axis. Orange ports are stilbenes. Blue and unlabeled ports are either filled with an HPGe detector, or are left empty.

of a given channel are written to disk in list mode. The GEBSort code [94], developed at Argonne, was used to merge the data from the the Gammasphere DAQ, calibrate and perform pole-zero corrections, and form coincidence events. The GEBMerge code time-sorted and merged the files of all digitizer channels, including HPGe, BGO, and TFGIC anode, into a single large file of list-mode hits. In GEBSort, the first event begins with the first hit. A time window of user-specified length, dTS, is opened after the timestamp of the first hit, and every hit that lies within the window is added to the event and reopens the time window. We chose $dTS = 1500$ ns. This choice avoids cutting real coincidences, especially since the anode and γ-ray triggers were offset by about 700 ns, without permitting noticeable pileup for our fission rate of ~ 4000 s^{-1}. BGO anti-coincidence is then applied: if an HPGe and its corresponding BGO detector receive hits within 500 ns of each other, the HPGe hit is tagged as "dirty". We modified the source code to output a ROOT [95] tree of these events.

All five TFGIC electrode waveforms were digitized with a CAEN V1740D (64 channels, 12 bit, 62.5 MS/s, 2 V dynamic range) and stored on disk. The CAEN stack applied coincidence logic in real time and output a ROOT tree of events. We recorded coincidence events in the *trans*-stilbene detectors with a CAEN V1730 (16 channels, 14 bit, 500 MS/s, 2 V dynamic

range) with DPP-PSD firmware for online waveform analysis—no stilbene waveforms were recorded. The two anode signals from each side of the TFGIC were cloned with a CAEN N625 fan-in fan-out unit and routed to two empty digitizer channels in the Gammasphere DAQ to provide a coincidence fission trigger in post-processing.

To synchronize the separate digital DAQ systems, we propagated a 50-MHz clock from the Gammasphere DAQ to the CAEN V1740D and a pulser signal was injected into both systems at the start of each run to measure the overall timestamp offset. The ROOT trees were correspondingly combined to form a tree of fission events containing all of the above information about the fragments and the γ rays detected in coincidence with them. Fig. 4.4 shows a 2-D histogram of the time difference between fission timestamps measured in the CAEN and DGS systems. The $\sim$ 700 ns offset arises from the earlier rise time of the cathode in the CAEN stack, which is used as the fission timestamp, compared to the later rise time of the anode in the DGS system. It is apparent that the clocks are synchronized since the offset does not change as a function of measurement time. About 2.5×10^9 fission events were recorded over approximately 180 h of experiment live time.

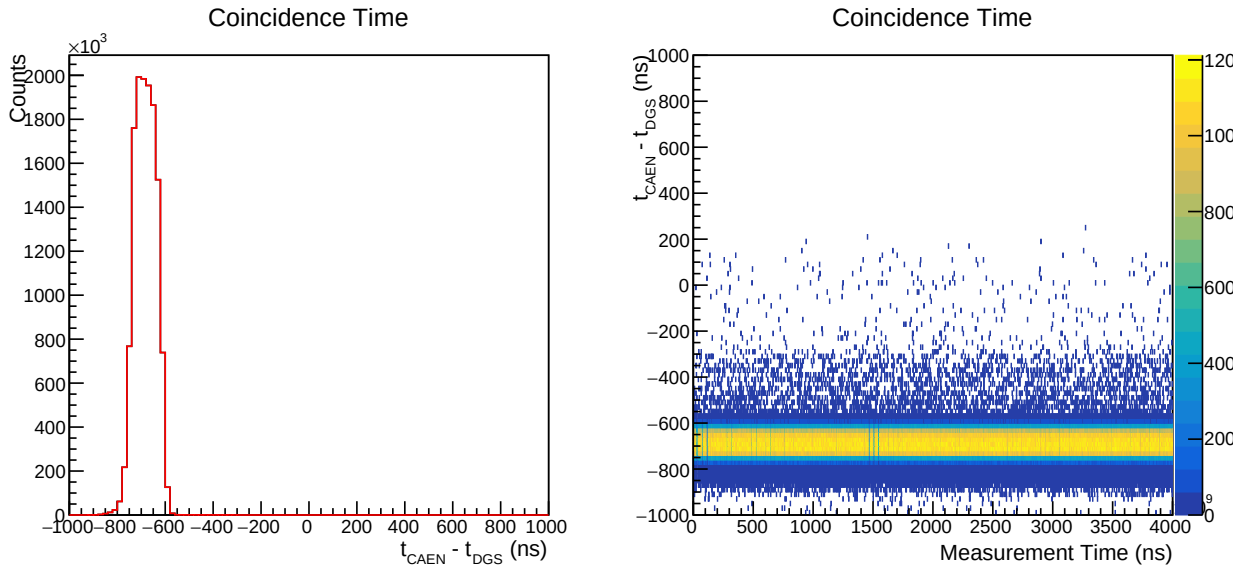

Figure 4.4: Time difference between fragment timestamp in CAEN system (cathode in V1740D) and average of both anode timestamps in the DGS system.

4.2.2 Detector calibration

The energy response of each HPGe detector was linearly calibrated with a ^{207}Bi radioactive source suspended in the geometric center of each hemisphere for about 30 minutes, in turn (see Figure 4.5). Argonne-developed software was used to find the peak locations and fit linear energy calibrations for each HPGe detector. The stilbene detectors were calibrated by matching the 477 keV Compton edge from a ^{137}Cs source, in the same configuration.

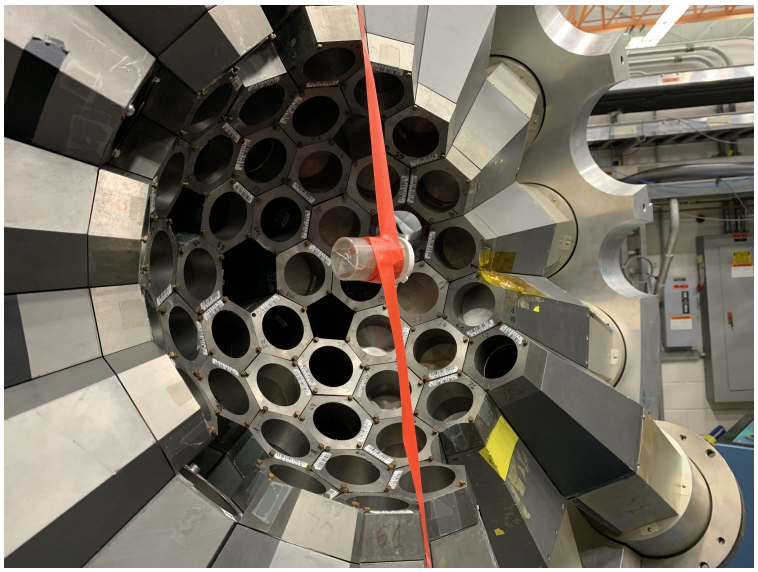

Figure 4.5: Energy calibration measurement with ^{207}Bi for the HPGe detectors in the north hemisphere of Gammasphere.

The full-energy peak efficiency was calibrated by placing a sealed 195.8 kBq ^{226}Ra source (certified March 1, 2023)—in equilibrium with its daughters—inside the TFGIC prior to loading the ^{252}Cf source, shown in Figure 4.6.

The TFGIC was installed inside Gammasphere in the chosen orientation (without fill-gas lines and bias/readout cables) and the HPGe response was recorded for 30 minutes. The total full-energy peak efficiency for the entire array was determined for energies ranging from the 74.8 keV $K\alpha$ x-ray to the 2447.9-keV ^{214}Bi γ ray, and comparing the measured counts to the expected total emission. Uncertainties in the integrals from RadWare, and in the expected counts from the data sheet [96], are propagated to the measured points in

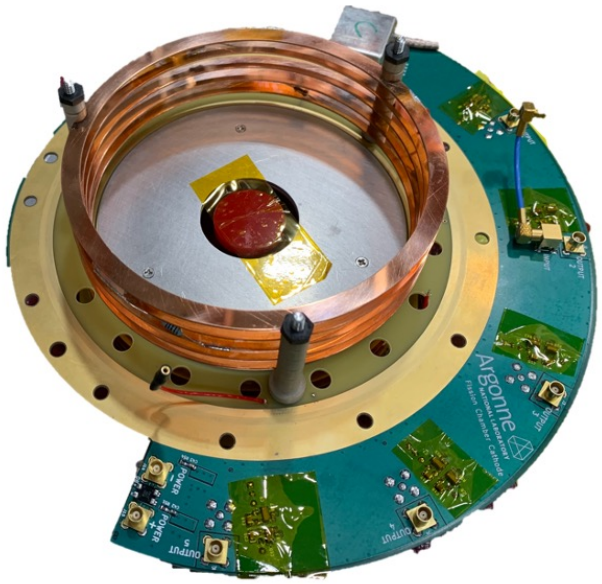

Figure 4.6: ^{226}Ra installed in the TFGIC, where the ^{252}Cf target would usually be.

Figure 4.7. The points were fit to Equation 4.1 using curve_fit from Python's SciPy package,

$$\log \epsilon = [(A + Bx)^{-G} + (D + Ey + Fy^2)^{-G}]^{-1/G}, \tag{4.1}$$

where $x = \log(E_\gamma/100 \text{ keV})$ describes the behavior at low E_γ and $y = \log(E_\gamma/1000 \text{ keV})$ the behavior at high E_γ, and G the sharpness of the interaction between the regions [97]. In this analysis, $G = 15$ was fixed to improve convergence. While Gammasphere holds up to 110 HPGe detectors, 63 were placed in the array and 54 were used in the final analysis. The others were discarded due to poor resolution or peak-to-total ratios. The total full-energy peak efficiency of the array is shown in Fig. 4.7.

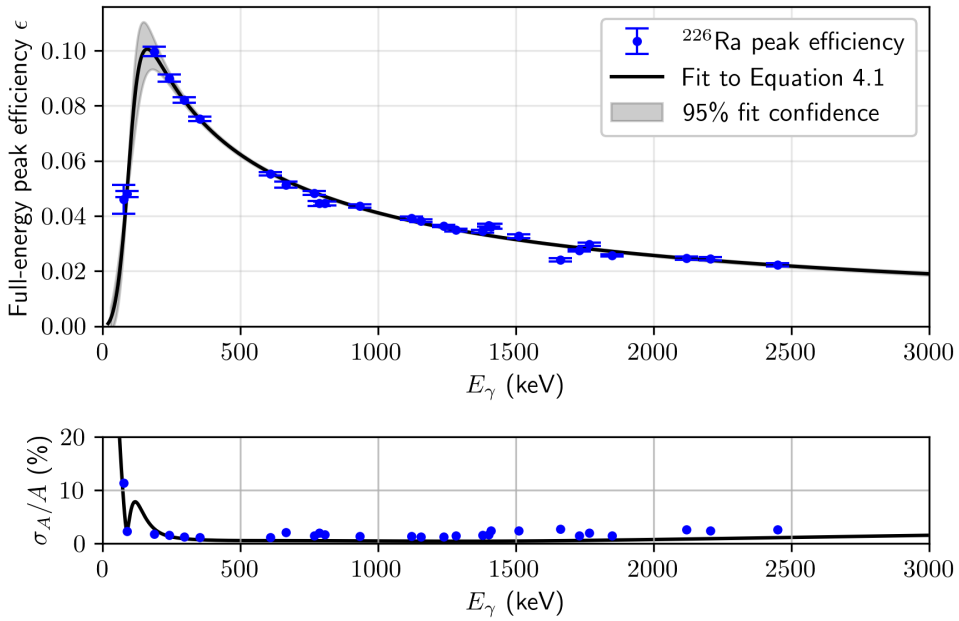

Figure 4.7: Full-energy peak efficiency of Gammasphere. The upper panel shows the measured full-energy peak efficiency of Gammasphere for many E_γ and the resulting $\epsilon(E_\gamma)$ fit. The grey band represents the spread of the fit as a function of E_γ, found by generating many efficiency curves from the fit covariance matrix. The lower panel shows the relative uncertainty (%) for the measured points and the fit.

To estimate the uncertainty on ϵ, or σ_ϵ, the fit parameter covariance matrix from curve_fit was used to randomly sample 10^5 alternative efficiency curves. The standard deviation of all fits ϵ from the original fit at each E_γ was used to construct the 2σ uncertainty band. The full-energy peak efficiency is a significant source of uncertainty in the experiment, up to $\sim 10\%$ at $E_\gamma \sim 145$ keV.

To appropriately correct for the non-uniform angular efficiency, we binned the Gammasphere detectors by $\cos\theta_{C7}$ (the opening angle between each detector and the C7 port—the location of the HPGe detector aligned with the chamber axis on the "source" side of the TFGIC). We then repeated the efficiency curve fitting procedure for each angle bin. The results are shown in Figure 4.8.

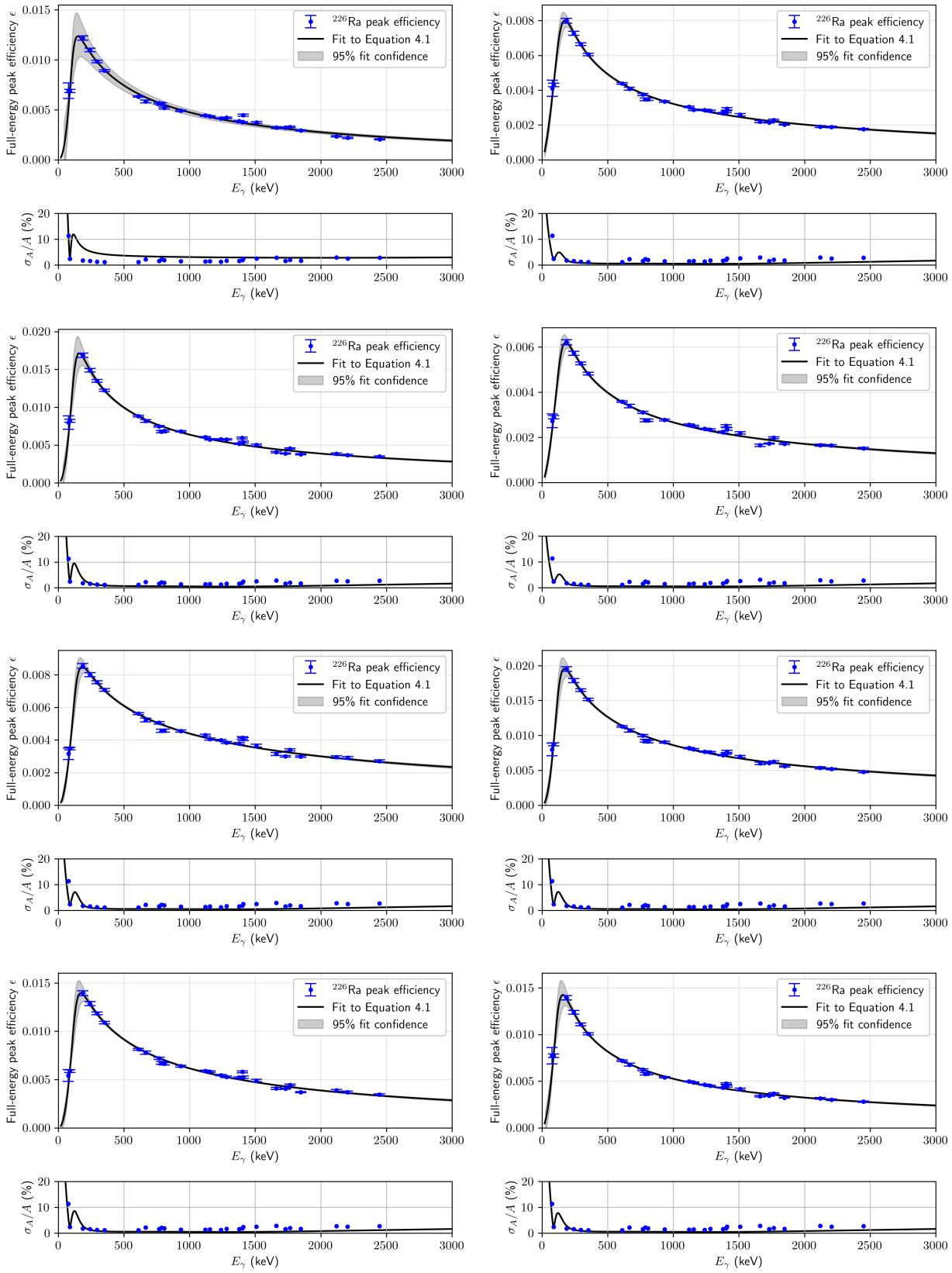

Figure 4.8: Full-energy peak efficiency curves for each cos bin. The eight bins are of uniform width from $\cos\theta = -1$ to 1.

I include some photographs of the experiment here. Fig. 4.9 shows the TFGIC during the ^{252}Cf target installation, with one of the chamber sides removed. Fig. 4.9 shows the TFGIC mounted inside an open Gammasphere, with aluminum foil surrounding the anodes to reduce electromagnetic noise from the environment. Fig. 4.9 shows the running configuration with Gammasphere closed, our rack of electronics, and the gas handling system.

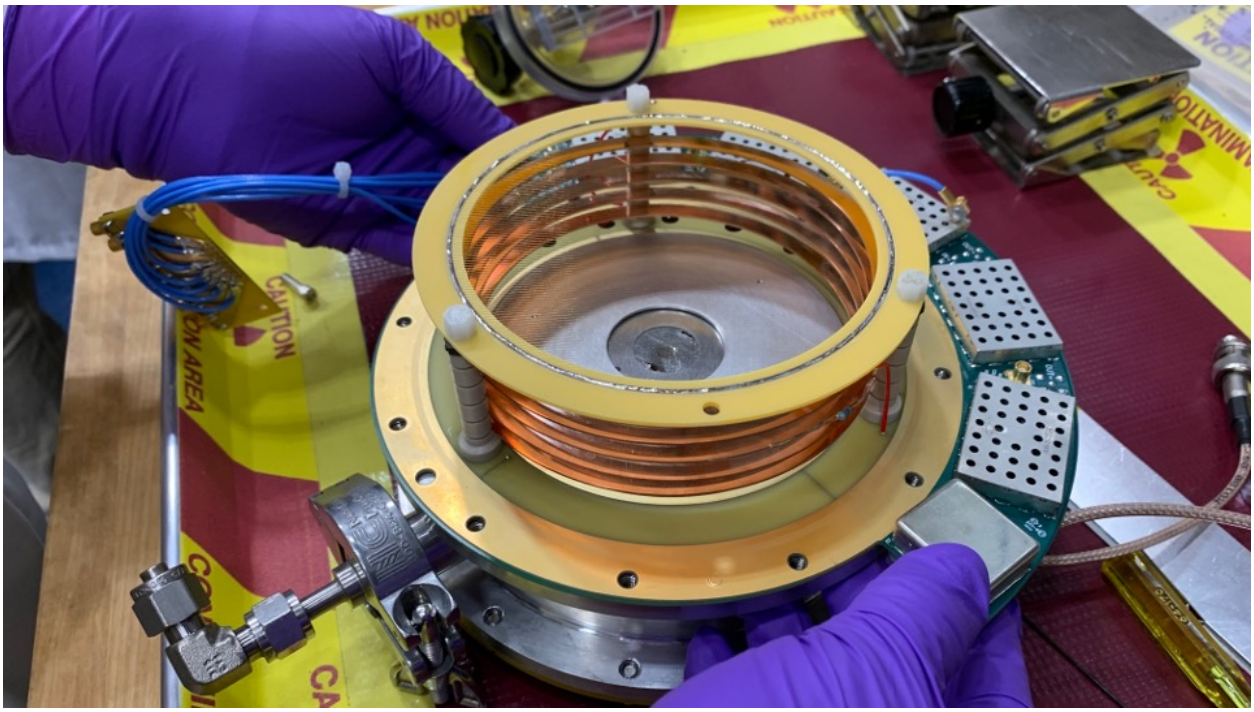

Figure 4.9: Photograph of open TFGIC, with ^{252}Cf source deposited on thin carbon backing visible.

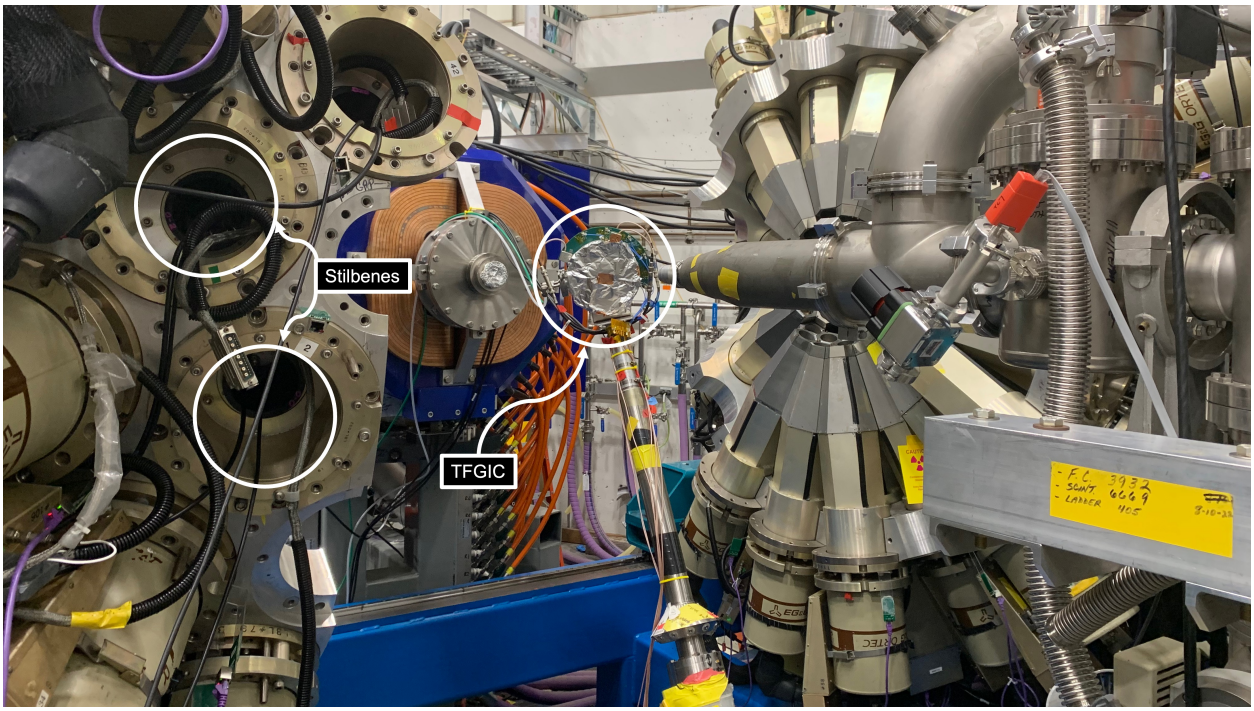

Figure 4.10: Photograph of TFGIC installed in Gammasphere. Locations of some of the *trans*-stilbene detectors are pointed out.

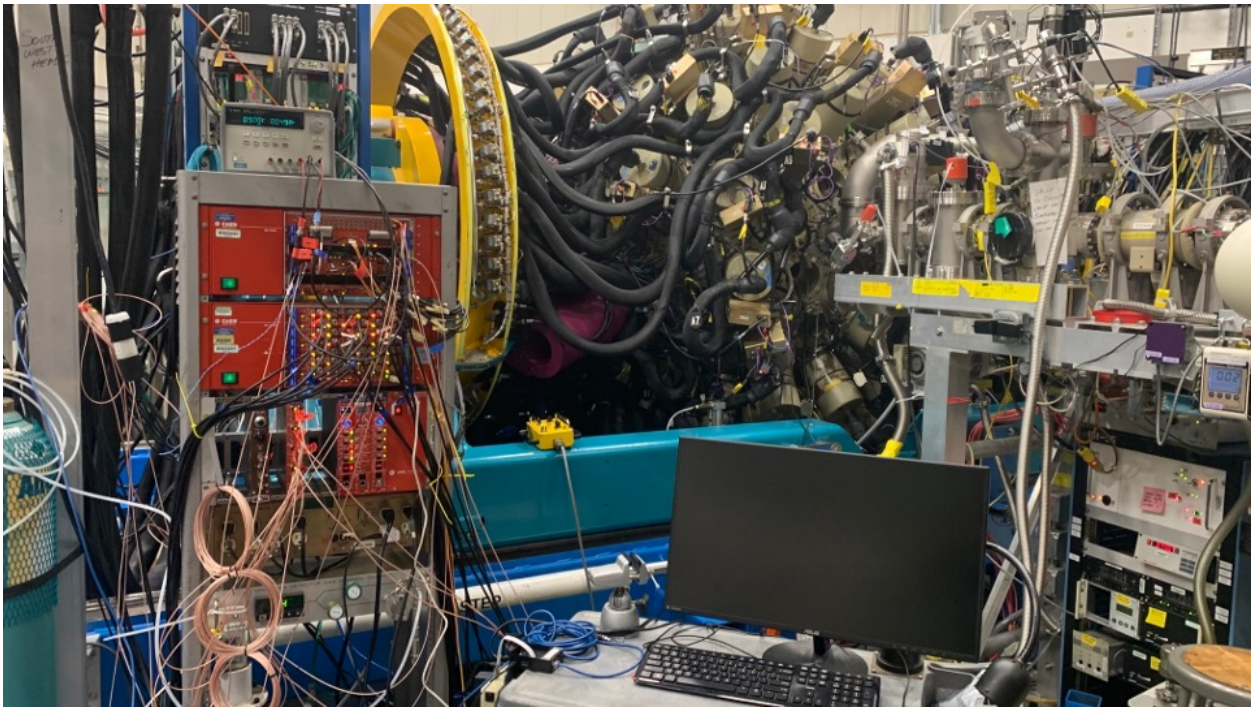

Figure 4.11: Experiment configuration, with Gammasphere closed around the TFGIC.

4.3 Analysis

The following method was employed to reconstruct the post-statistical spin distribution of ^{144}Ba, a high-yield fragment (3.37% [98]) resulting from ^{252}Cf spontaneous fission, as a function of TKE. This approach is applicable to other fragments for which there are sufficient statistics.

4.3.1 Selecting events with ^{144}Ba

Several cuts are applied to isolate fission events that contain ^{144}Ba in the final state. The first cut is a fragment mass cut: fission events for which the reconstructed pre-neutron-emission mass of the heavy fragment, A_H, is within 3 u of the post-neutron-emission mass ($A'_H = 144$ u) plus the average neutron multiplicity, $\bar{\nu}(A, \mathrm{TKE})$ from Göök *et al.* [8], are accepted [90]. The second is a fission axis angle cut, where only fission events that are aligned with the cylindrical axis of TFGIC, $|\cos\theta_\mathrm{f}| > 0.9$ are accepted. This step is essential to fully constrain the fission axis and perform Doppler correction of the prompt γ rays, as the TFGIC does not provide a measurement of the azimuthal angle of the fission axis.

Since ^{144}Ba is a heavy fragment, all γ rays from a fission event that passes the mass and angle cuts are Doppler-corrected as if they originated from the heavy fragment. The overall effect is that peaks from heavy fragment transitions are sharpened, and those from light fragments are broadened further. Fission events are tagged for further analysis if they contain a γ ray with corrected E_γ^H in the heavy fragment frame that overlaps with the first-excited-state transition of ^{144}Ba at 199 keV. Binning the remaining γ rays by their E_γ, the opening angle they make with the light fragment's direction of travel, $\cos\theta_L$, and the total kinetic energy of the fission event, TKE, we obtain the 3-D histogram that contains all of the necessary information to reconstruct the post-statistical-emission spin distribution of ^{144}Ba as a function of TKE. Such a histogram is shown in Fig. 4.12. Since the fragments are emitted back-to-back in spontaneous fission, the choice of $\cos\theta_L$ instead of $\cos\theta_H$ is arbitrary

and does not affect the analysis. Each bin entry is adjusted using angle-dependent efficiency curves to enable the reconstruction of angular distributions of discrete transitions relative to the fission axis.

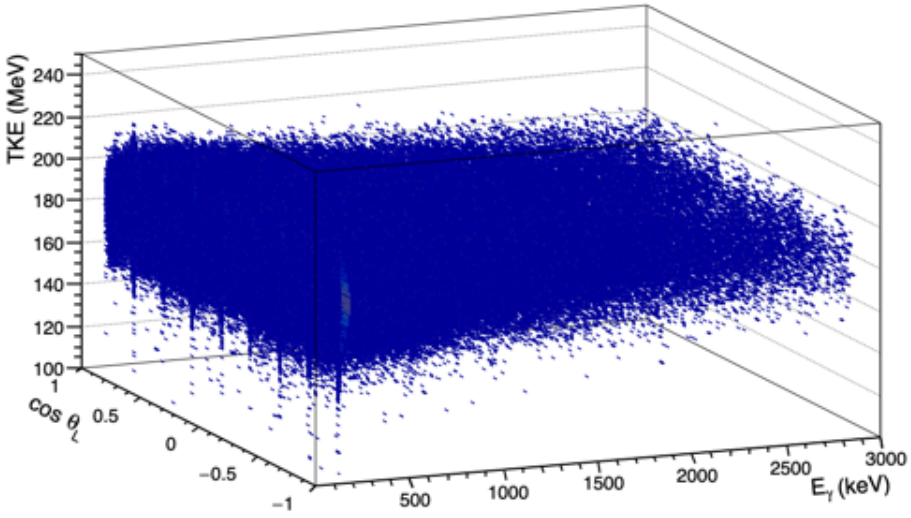

Figure 4.12: Measured 3-D γ-ray spectrum, gated on ^{144}Ba events.

4.3.2 Total kinetic energy binning

The 3-D spectrum is sliced by total kinetic energy (TKE) to examine correlations between energy and spin. Selected events in the median 98% of the TKE distribution shown in Fig. 4.13 are binned such that each TKE bin contains about the same amount of fissions. This step minimizes systematic uncertainties that could arise from bins of uniform width, but non-uniform statistics. There are about 10^5 fissions in each of the seven TKE bins.

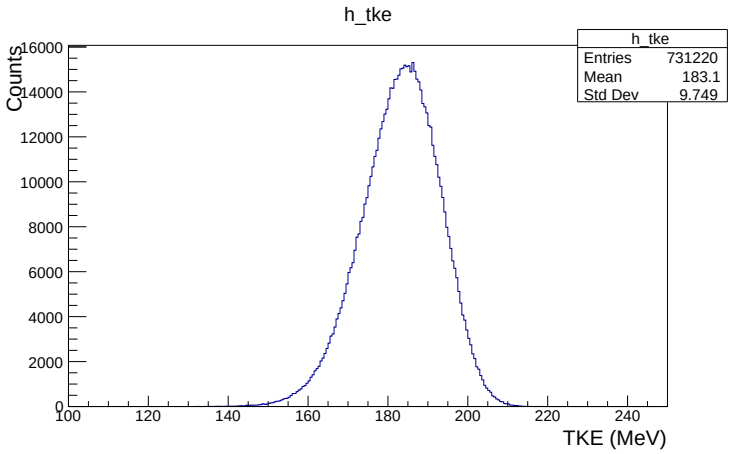

Figure 4.13: TKE distribution of accepted ^{144}Ba events.

4.3.3 Spectrum fitting

Each TKE slice is a 2-D spectrum, shown for example in Fig. 4.14, with axes E_γ and $\cos\theta_L$. Transitions from ^{144}Ba, as well as some from its common partner fragments, ^{102,104,106}Mo, appear as "tilted" lines with respect to $\cos\theta_L$. Most prompt γ rays are emitted before the fragments slow substantially, so fragment $\beta \sim 0.03 - 0.05$ are typical. The Doppler-shifted energies are accordingly shifted by a few % depending on the opening angle between the γ-ray and fragment directions, as is apparent in Equation 4.2

$$E_\gamma^{\mathrm{CM}} = E_\gamma^{\mathrm{lab}}\gamma(1 - \beta\cos\theta_{\mathrm{lab}}), \tag{4.2}$$

where E_γ^{CM} is the γ-ray energy in the fragment frame, E_γ^{lab} is the measured γ-ray energy in the lab frame, β is the speed of the fragment in natural units, and θ_{lab} is the opening angle between the fragment and γ ray in the lab frame.

Since the transitions from the light and heavy fragments are Doppler-shifted in opposite directions with respect to $\cos\theta_L$, the two can be separated based on the direction of the bend: the light fragment lines are tilted forward such that a higher lab-frame E_γ is observed at large $\cos\theta_L$, while the heavy fragment lines are tilted backward.

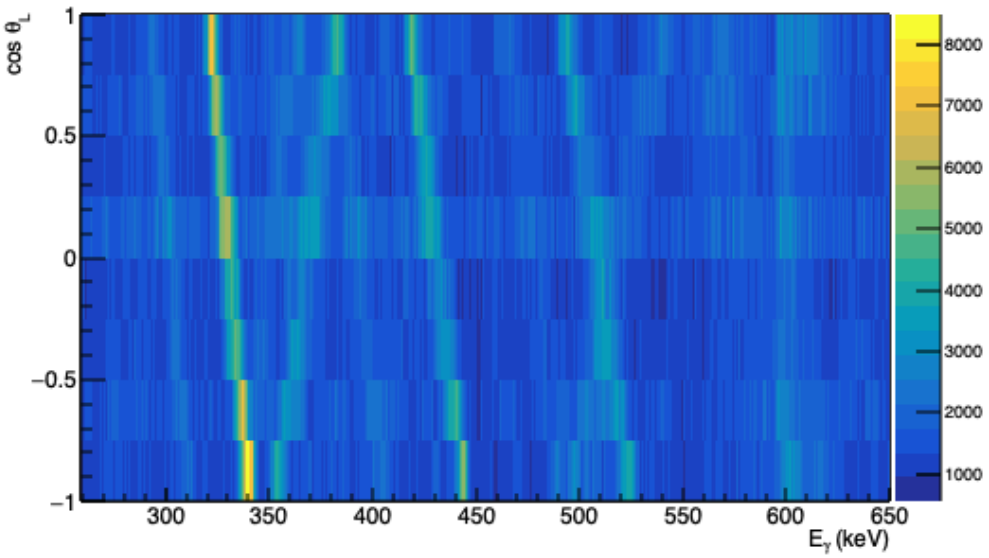

Figure 4.14: 2-D γ-ray spectrum of ^{144}Ba after projecting along the TKE axis. Heavy fragment lines with $E_\gamma = 331, 431,$ and 509 keV are clearly visible, as is a light fragment line with $E_\gamma = 369$ keV.

To achieve the best possible E_γ resolution for ^{144}Ba transitions, all measured γ rays were Doppler-corrected to the heavy fragment center-of-mass frame. The velocities of the fragments were determined from the mass and TKE, and $\cos\theta_L$ was determined from the opening angle between the TFGIC cylindrical axis and the position of the HPGe detector that registered the count. The result, shown in Fig. 4.15, is vertical ^{144}Ba lines and further tilted Mo lines.

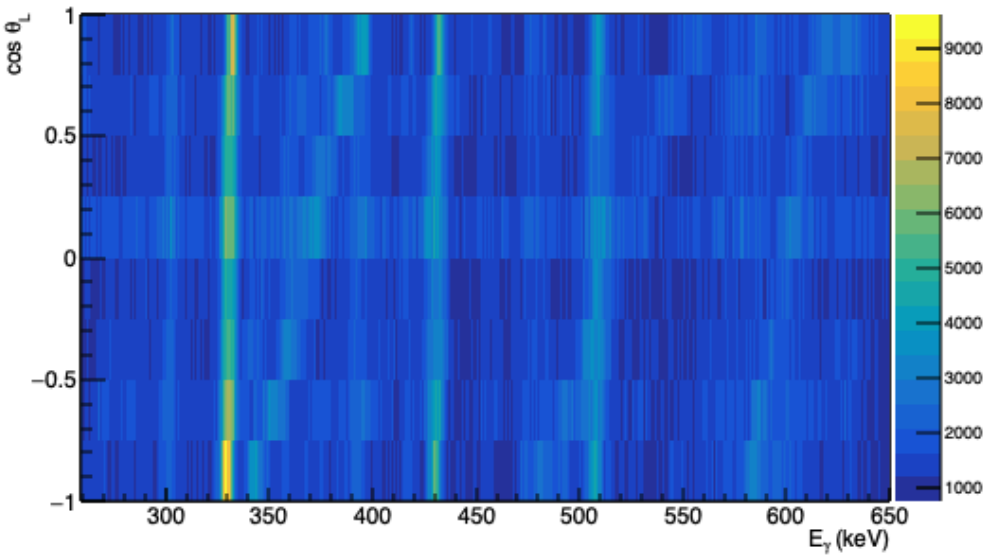

Figure 4.15: 2-D γ-ray spectrum of ^{144}Ba, Doppler-corrected to the heavy fragment frame.

The γ-ray background is estimated using a statistics-sensitive non-linear iterative peak-clipping (SNIP) algorithm [99], implemented in ROOT's TSpectrum class, and subtracted, see Fig. 4.16. The net 2-D spectrum in Fig. 4.17 is globally fit with a model containing lines that are gaussian broadened for the discrete ^{144}Ba and ^{104,106}Mo transitions. The peak energies in the center-of-mass frame are fixed based on the transition energies in ENSDF [29, 100, 101]. As all γ rays have been Doppler-corrected to the heavy fragment frame, an additional $\cos\theta_L$-dependent term is included for the partner fragment peak locations. The peak areas are left to be fit simultaneously, where the former comprises the first three Legendre polynomials with appropriate coefficients $C_0P_0+C_1P_1(\cos\theta_L)+C_2P_2(\cos\theta_L)$. $C_1 \neq 0$ results from residual Doppler asymmetries, while $C_2 \neq 0$ is necessary in cases where the fragment spin is polarized with respect to the fission axis and γ rays are emitted anisotropically (such as stretched E_2 γ rays). Higher-order P_n are not included to avoid overfitting to few noisy angular bins. Interestingly, the 330.8-keV $4^+ \rightarrow 2^+$ ground-state-band transition, exhibits a $C_2/C_0 \sim 1/3$, indicating a high degree of polarization in the substates of the 4^+ state, see Fig. 4.19. The resulting fit for the first TKE bin is shown in Fig. 4.18. The integrals of these peaks, and the uncertainties thereof, are calculated from the fit parameters and used to determine the

relative intensities of the transitions.

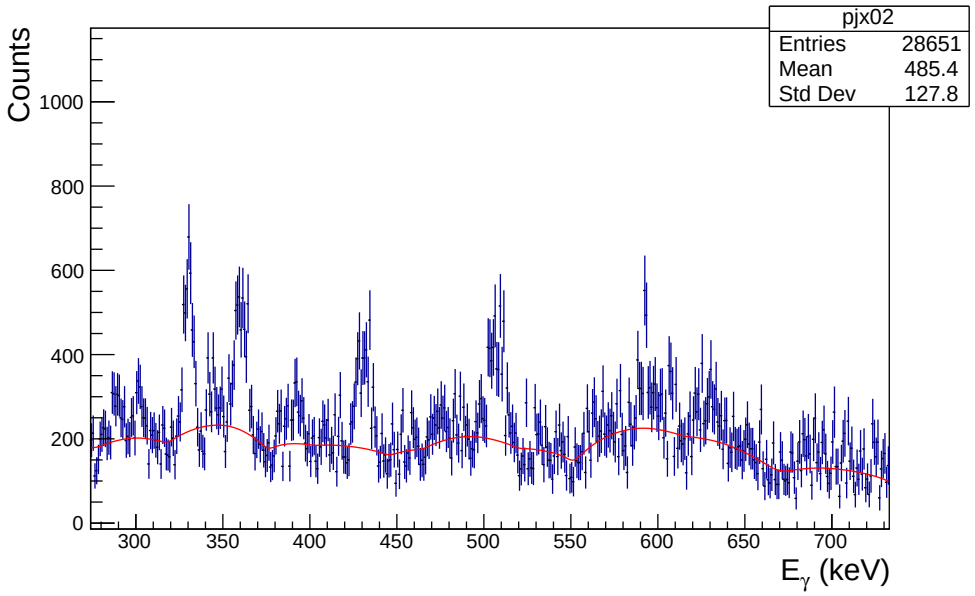

Figure 4.16: Background from SNIP algorithm. 1-D γ-ray spectrum of ^{144}Ba, for $-0.5 < \cos\theta_L < -0.25$ and $158.5 < \text{TKE} < 173$ MeV.

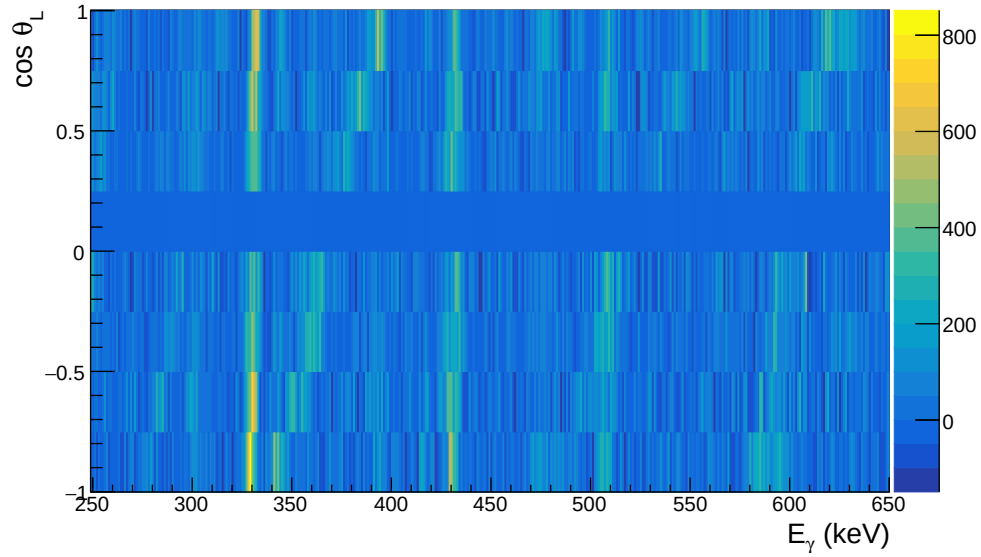

Figure 4.17: Background-subtracted 2-D γ-ray spectrum of ^{144}Ba for $158.5 < \text{TKE} < 173$ MeV. Horizontal axis is E_γ (keV) and vertical axis is $\cos\theta_L$.

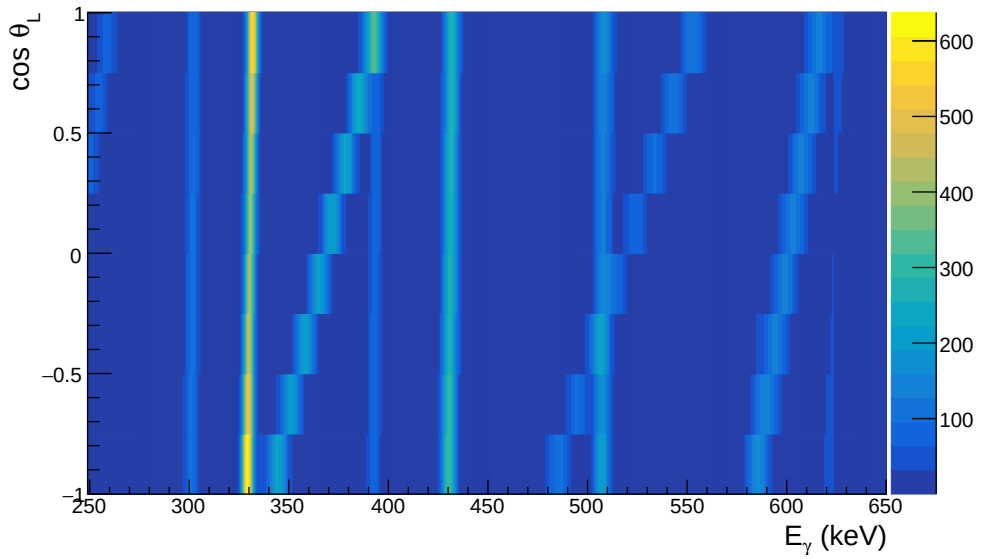

Figure 4.18: 2-D fit to background-subtracted 2-D γ-ray spectrum. Horizontal axis is E_γ (keV) and vertical axis is $\cos\theta_L$.

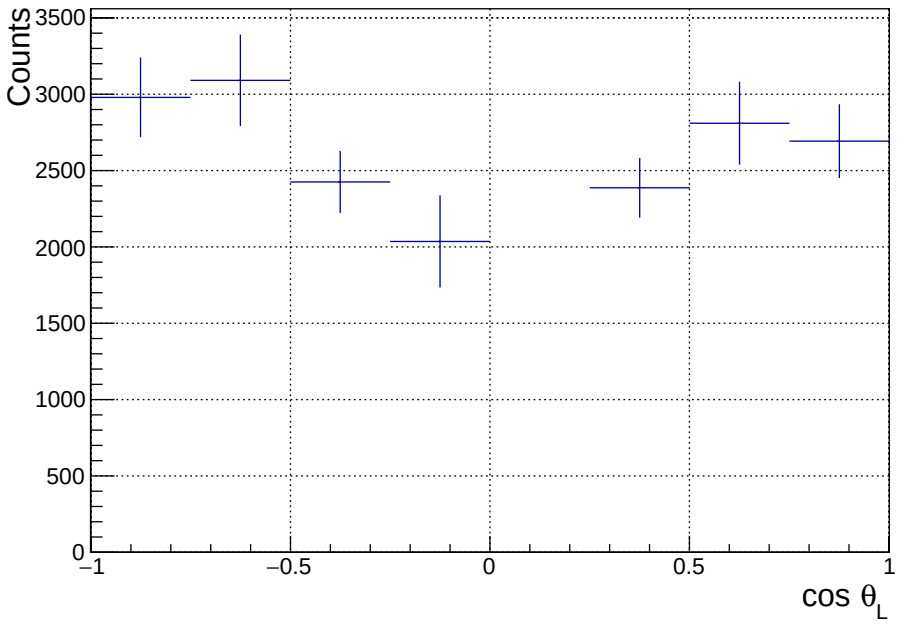

Figure 4.19: Angular distribution of the 330.8-keV $4^+ \rightarrow 2^+$ ground-state-band transition for the $158.5 < \text{TKE} < 173$ MeV bin. There is a clear P_2 presence.

Because we gate on the $2^+ \rightarrow 0^+$ 199-keV transition, its intensity cannot be measured

from this spectrum. We instead perform a similar gating procedure on a common partner fragment, ^{104}Mo, so that both the ^{144}Ba $2^+ \rightarrow 0^+$ transition and the $4^+ \rightarrow 2^+$, 330.8-keV transition feeding that state can be fit. Their ratio is used to reconstruct the 199-keV transition intensity. The overlapping $4^+ \rightarrow 2^+$ 332.4-keV transition from ^{146}Ba was accounted for by measuring the ^{146}Ba $2^+ \rightarrow 0^+$ transition as well, see Fig. 4.21.

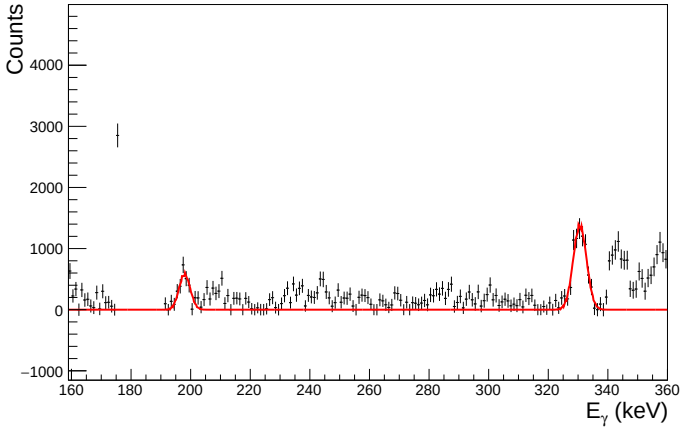

Figure 4.20: 199-keV and 331-keV ^{144}Ba lines visible after gating on ^{104}Mo. There is a contaminant from 332.4-keV transition from ^{146}Ba. The contamination is estimated based on Fig. 4.21.

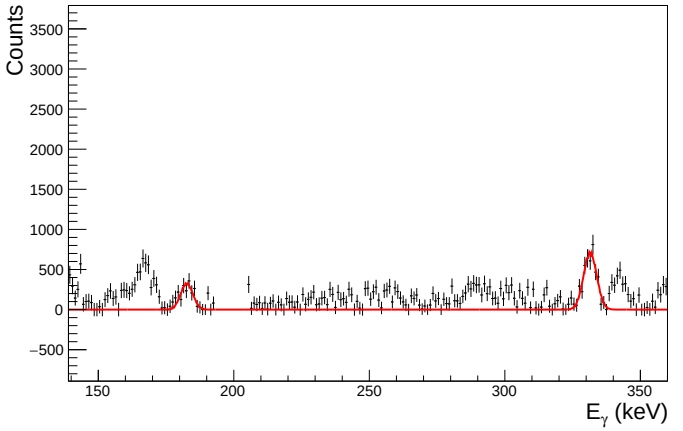

Figure 4.21: 182-keV and 332-keV ^{146}Ba lines visible after gating on ^{104}Mo. The 332-keV contamination is subtracted based on the relative intensity of the 182-keV compared to the 199-keV from ^{144}Ba.

4.3.4 Intensity balance

The measured γ-ray intensities are combined with the well-studied structure of low-lying levels in ^{144}Ba from the ENSDF database [29]. Determining the amount of side-feeding S_i from the continuum to a low-lying level i, through transitions of known energy, gives direct access to the post-statistical-emission spin distribution of the fragment. The S_i to a level i is simply the sum of all incoming intensities from higher-energy discrete levels subtracted from the sum of all outgoing intensities [14]. The measured γ-ray intensities are appropriately adjusted for electron-conversion coefficients taken from BrIcc tables with the Frozen Orbital approximation [102]. Statistical uncertainties from the fitted spectra are propagated through the fit parameters, to the calculated peak intensities.

4.3.5 Reconstructing average spin

After calculating the side-feeding to each low-lying level, the feedings were correlated to the spin of that level, I, and normalized to form a spin probability distribution $P(I)$ like in Fig. 4.23. The average of the distribution $\langle I \rangle$ is simply $\sum_i I_i S_i$, where i runs across the low-lying levels.

The statistical uncertainty in the intensities and the uncertainty in the efficiency, which is between 1-5% for most yrast γ rays, were propagated in the following manner to preserve the effect of potentially large covariances in the side-feedings S_i. An ensemble of possible intensity "measurements" were randomly generated based on (i) their statistical uncertainties and (ii) the covariance matrix of the efficiency curve fit parameters. In other words, each intensity was sampled from a normal distribution, then the efficiency curve was perturbed and the intensities adjusted accordingly. The S_i for all levels were calculated for each of these generated sets of intensities, such that a covariance matrix $\mathrm{cov}(S_i, S_j)$ could be constructed and used in the calculation of $\langle I \rangle$. The corresponding correlation matrix, $\rho(S_i, S_j) = \mathrm{cov}(S_i, S_j)/\sigma_{S_i}\sigma_{S_j}$, is shown in Fig. 4.22. Typical non-diagonal values in these $\rho(S_i, S_j) \in [-1, 1]$ are negative; most positive correlations are on the order of 0.02, whereas

negative correlations reach $\sim (-0.75)$. While unsurprising, it highlights the importance of including the covariances. Failure to do so would lead to a substantial overestimation in uncertainty.

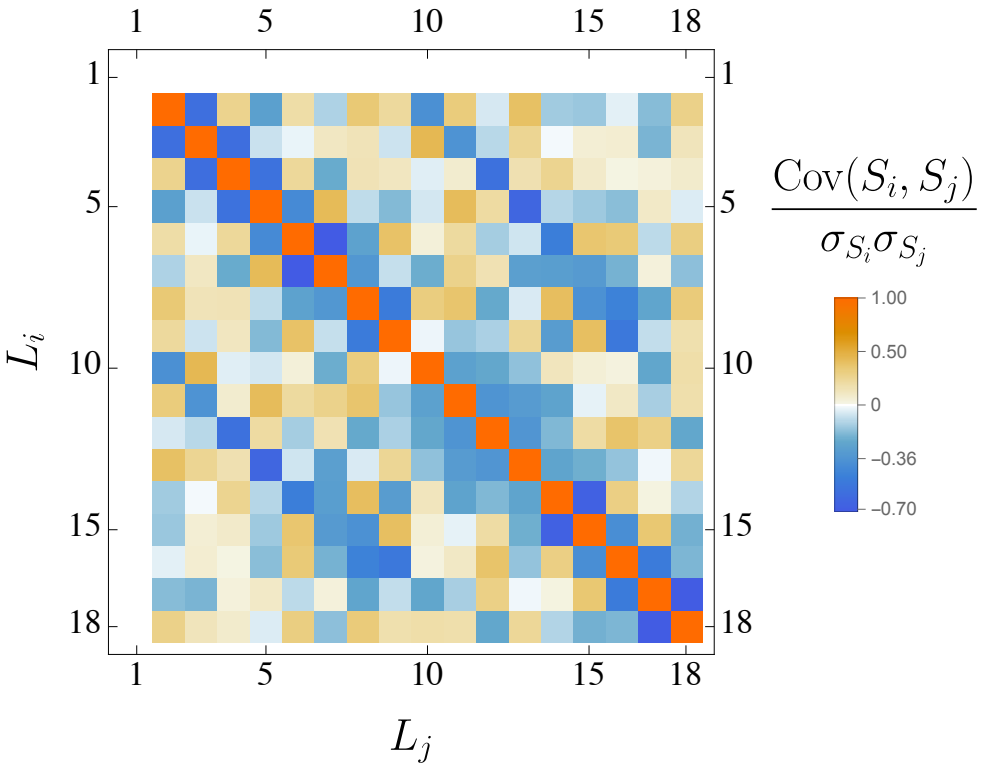

Figure 4.22: Correlation matrix for side-feeding S to levels $L_{i,j}$ for a single TKE bin.

The direct feeding from the quasi-continuum to the ground state is not directly measurable through classical γ-ray spectroscopy. We estimate the ground-state feeding by fitting the ground-state-band feeding with a statistical spin distribution [49] and extrapolating to $I = 0$. The distribution is shown for one TKE bin in Fig. 4.23. Interestingly, the side-feeding to the ground-state band in black, and the octupole band in blue that is built on the 785-keV 1^- state, appear to have distinct shapes. The distributions for all TKE bins are shown in Fig. 4.24. While in some cases the reconstructed distributions are not smooth, this behavior does not significantly impact the conclusions since we take only the first moment of the distribution.

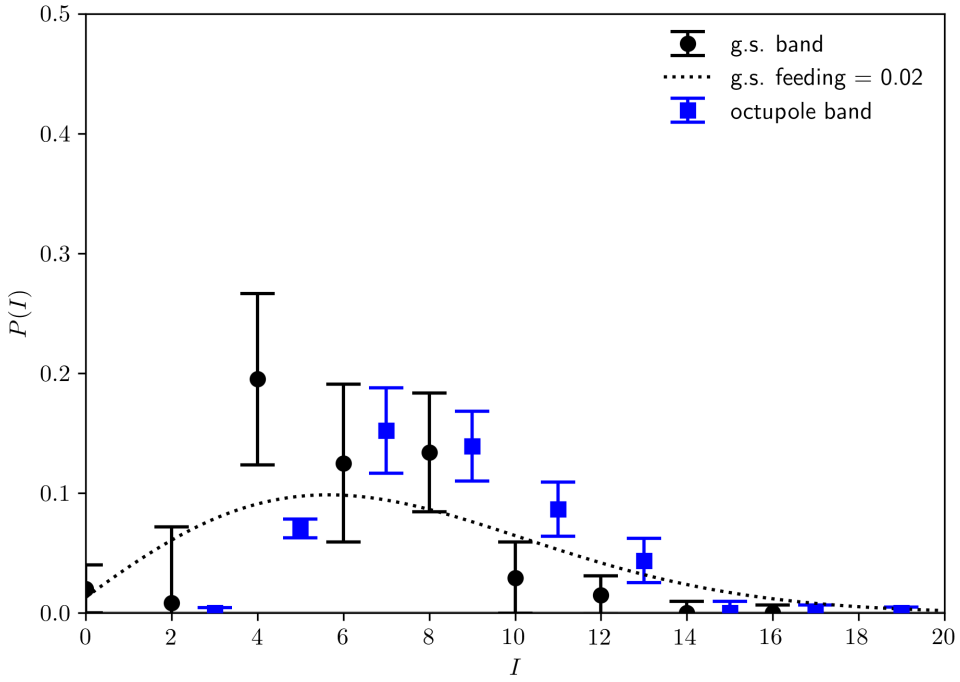

Figure 4.23: Reconstructed spin feeding distribution for a TKE bin, 173 – 178 MeV.

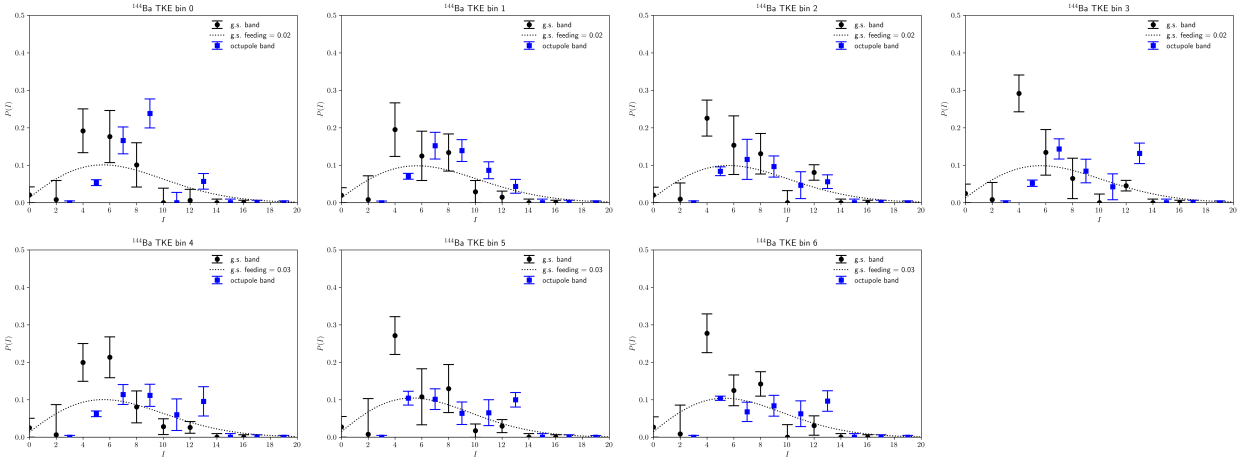

Figure 4.24: Spin distributions for all TKE bins.

4.4 Results

The average spin, $\langle I \rangle$ of ^{144}Ba was reconstructed for TKE bins with a total range of 158 - 203 MeV (roughly equivalent to a total excitation energy (TXE) range of 12 - 58 MeV). The

results are shown in Fig. 4.25, where the TKE probability distribution (green histogram) is included in the background. $\langle I \rangle$ changes only by about $0.5\hbar$ across the entire TKE range. The uncertainties in $\langle I \rangle$ include the statistical and fit uncertainties of the measured intensities, as well as the efficiency uncertainty, as described in Section 4.3.5. The horizontal bars denote the widths of the TKE bins, while the horizontal location of the points indicates the average TKE in that bin.

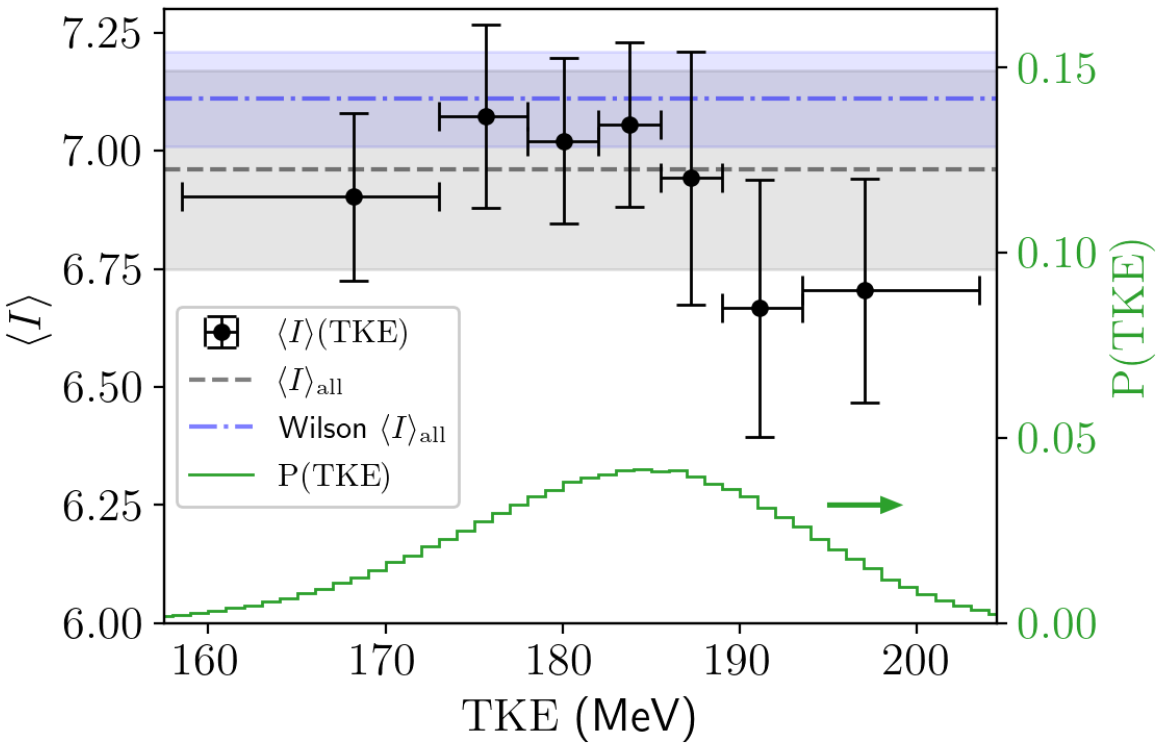

Figure 4.25: Measured $\langle I \rangle$ as a function of TKE for ^{144}Ba. The TKE-integrated value of $\langle I \rangle_{\text{all}} = 6.96 \pm 0.21$ (black dashed) agrees well with that of Wilson *et al.* [14], 7.11 ± 0.09 (post-statistical emission, blue dash-dotted). The horizontal bars signify the widths of the TKE bins. The underlying TKE distribution is shown in green on the right axis.

4.5 Discussion

We interpret the minimal dependence of ^{144}Ba $\langle I \rangle$ on TKE as indicative of its insensitivity of the spin to the fragment's initial excitation energy. The TKE is complementary to the TXE of the fragments for a given mass split, and since we know from neutron multiplicity measurements [8] that ^{144}Ba receives about half of the total TXE, this behavior indicates that the spin of ^{144}Ba does not change significantly with excitation energy. This result is in agreement with the measurement by Wilhelmy *et al.* [13], who have also observed a spin-TKE independence, although they were sensitive only to the first few ground-state-band transitions and had three TKE bins. This interpretation is validated in view of a previous γ-ray multiplicity measurement: the $A = 106$ panel in Fig. 6 of Ref. [10] shows that the γ-ray multiplicity of heavy fragments around the mass of ^{144}Ba is nearly flat as a function of excitation energy, especially in the TXE = 12 - 58 MeV range. The insensitivity of $\langle I \rangle$ in ^{144}Ba to energy could indicate that the spin generated in fission is not statistically generated based on the fragment temperature—at least primarily—but through other means. In the statistical model, the scale of the average spin is approximately dependent on $(E^*)^{1/4}$, which should result in a change of $\approx$ 50% as the E^* is increased by a factor of 5, the range we have examined in this work. The relative change we have observed, approximately $5-10$ % at most, is not compatible with this simple prediction.

This analysis introduces some potential sources of bias. Those sources and their effects on the results are discussed here.

Background subtraction and fitting—Transitions from ^{144}Ba, as well as strong transitions from partner fragments and other sources, produce features in the γ-ray spectra that can be fit simultaneously. However, the background of statistical and weak, unrelated γ-ray transitions cannot be easily separated and subtracted. This background was estimated with the Background method of ROOT's TSpectrum class, and parameters were chosen to prevent

overfitting. The most important parameter, the clipping window width, was perturbed to assess the sensitivity of the results to the choice of window width. It was found to be relatively insensitive.

Incomplete level scheme knowledge—One potential source is incomplete level-scheme knowledge. Only known ^{144}Ba transitions in the level scheme were fit, and thus this analysis is insensitive to side-feeding of levels that are absent in the evaluation. This source was considered negligible since all peaks with substantial intensity were identified, and thus the feeding to some unknown state—and its impact on the reconstructed average spin—would be insignificant for any reasonable level spin.

Intensity bypassing the first excited state—This method is insensitive to any flow of intensity that bypasses the first-excited state. For ^{144}Ba, two such paths exist to bypass the 199-keV first excited state: the 758.9 keV (1^-) and 1864.2 keV (2^+) states have been observed to decay directly to the ground state. Neither of these direct-to-ground-state transitions, however, were observed alongside the 199 keV transition when gating on common partner fragment ^{104}Mo. We concluded that for ^{144}Ba, the impact of any missed intensity due to gating on the first-excited state was negligible.

Ground-state feeding estimation—The method for estimating feeding from the statistical regime directly to the ground state described in Section 4.3.5 relies on the assumption that the shape of the real spin probability distribution resembles that of Bethe's work from statistical considerations [49]. This assumption results in an estimation of small ground-state feeding ($\sim$ few %) in ^{144}Ba, which is reasonable since ^{144}Ba is easily deformed. We abscribe a large relative uncertainty to this point due to the model dependence.

Overlapping γ rays—In some cases, transitions from the same nucleus are too close in

energy to resolve. The total intensity of these E_γ multiplets is divided among the transitions in a way that avoids reconstructing unphysical negative side-feedings. The side-feeding distribution is calculated for all possible partitions, and among the allowed partitions, and best estimate is taken as the mean allowed strength. Transitions that are close in energy but originate from a partner fragment or another stationary background source can be separated based on Doppler considerations, so this estimation only needs to be done for ^{144}Ba lines.

Contamination from other fragments—Potential contamination from heavy fragments other than ^{144}Ba could arise if that contaminant is i) similar in mass and ii) shares two transition energies with ^{144}Ba, one being the 199-keV first-excited-state transition. The potential for contamination in the case of ^{144}Ba was evaluated with FIFRELIN [40], a Monte Carlo code which models the de-excitation of fission fragments. It was determined that no heavy fragments would exhibit appreciable contamination: even the most likely candidates of ^{145}Ba and ^{147}La would produce doublets of two to three orders of magnitude weaker intensity, well within statistical uncertainty.

4.6 Conclusion

We combined for the first time a twin Frisch-gridded ionization chamber with a world-class γ-ray spectrometer to measure the average spin of fission fragments produced in ^{252}Cf(sf) as a function of TKE, or $\langle I \rangle$(TKE). In ^{144}Ba, the average spin increased as TKE decreased, but only by about $0.5\hbar$ over the measured TKE range of 158.5 to 203.5 MeV. This result aligns with that of Marin *et al.* [10], which showed that the heavy fragment γ-ray multiplicity—often used as an indirect measure of fragment spins—for this mass split quickly plateaued with increasing excitation energy. We suggest that this insensitivity to TKE, and therefore to excitation energy for ^{144}Ba, points toward a more complex spin generation mechanism than

the statistical feeding that is included in some modern fragment de-excitation models.

In the near future we will apply the developed method to other fission fragments in this dataset to build a picture of the "spin-energy surface," or the average spin as a function of both TKE and fragment. Upon including more fragments, we expect to reveal whether the spin-energy correlations are sensitive to fragment mass, ground-state deformation, or other properties.

4.7 Contributions

This Chapter is based on a paper that was submitted to Physical Review C in June 2024.

Stefano Marin and Fredrik Tovesson made this experiment happen, and credit for the long-range planning goes to them. I led the short-term planning on-site, the experimental run, and performed all of the analysis in the Chapter.

This experiment and the resulting Chapter are simultaneously my greatest personal triumph as a scientist, and also that which I would have least been able to complete without the efforts and advice of my colleagues. Khushi Bhatt, Mike Carpenter, Chloé Fougères, Vasil Karayonchev, Ben Kay, Torben Lauritsen, Darek Seweryniak, Nate Watwood, and Dana Duke all lent their time and wisdom during the two-week-long experimental run. I would like to give special acknowledgement to Ivan Tolstukhin, Michael Oberling, Claus Mueller-Gatermann, Russ Knaack, and Amel Korichi for their great contributions during the experiment, helping me debug the stream of issues we faced—often at odd hours—and for picking up some of the less desirable shift times. Lastly, this experiment was the brainchild of Stefano and Fredrik. Thank you for entrusting me with the experiment's success.

CHAPTER 5

Summary, Conclusions, and Outlook

In this dissertation, we have presented new experimental evidence on correlations between the spin and energy generated in fission fragments. We briefly summarize the previous Chapters in Section 5.1 and discuss the implications of the results on our understanding of fission and how they fit into the corpus of fission experiments in 5.2. We discuss future work and give closing remarks in 5.3 and 5.4.

5.1 Summary of experiments

In Chapter 2 we measured the fission γ-ray spectrum of ^{239}Pu(n,f) as a function of incident neutron energy, E_i. After translating the incident neutron energy to the average compound nucleus excitation energy at each E_i, or $\langle E_x \rangle$, we reached two important observations: (i) the total γ-ray multiplicity, $\overline{N}_\gamma$ increases approximately linearly with $\langle E_x \rangle$, with a slope of 0.085 ± 0.010 MeV^{-1} and (ii) the spectrum of the additional γ rays is strongest around $E_\gamma \sim 0.7$ MeV. This change in the spectrum is consistent with increased feeding to higher-spin states in the fragments, so we concluded that we found evidence of positive spin-energy correlations. While these correlations appeared linear within $9 < \langle E_x \rangle < 19$ MeV, there was insufficient evidence to claim that the spin-energy correlations were linear as well.

We presented the flange-less twin Frisch-gridded ionization chamber (TFGIC) in Chapter 3. We characterized its resolutions in TKE ($\sim$ 3-4 MeV FWHM), fragment mass ($\sim$ 5 AMU FWHM), and fission axis angle ($\sim$ 0.11 FWHM in cosine) and demonstrated that

we could recreate previous measurements from Göök *et al.* [8] and Travar *et al.* [9] that correlated fragment properties, like TKE and mass, with neutron and γ-ray multiplicities.

In Chapter 4, we combined the TFGIC with Gammasphere, a spherical array of 110 Compton-suppressed high-purity germanium detectors. We simultaneously measured the fragment properties (TKE, mass, and polar angle) and the energies and angles of the prompt γ rays. The major difference between this experiment and previous experiments correlating fragment properties with n/γ emission is the ability to do high-resolution γ-ray spectroscopy. After performing fragment angle cuts and Doppler correcting the γ rays, we can observe and set E_γ gates on specific transitions between low-lying nuclear states in specific fragments. This capability allows us to (i) select specific fragments, fully constraining the (Z, A) and (ii) measure the distribution of feeding to low-lying levels. Since the spins of these low-lying levels is well-documented in the ENSDF database for common fragments, we can reconstruct the distribution of spins that are fed as a function of TKE for specific nuclei. We perform this analysis for ^{144}Ba and find that its spin varies little with TKE, and therefore, with excitation energy. This result provides the first conclusive evidence from the modern era of experiments that the spin generation mechanism is not purely statistical.

5.2 Past and present experiments

The corpus of fission experiments on correlations is extensive. In this Section, we highlight a subset of them and discuss how our results fit in. The subset is summarized below and in Table 5.1 below.

- Wilhelmy *et al.* (1972) [13] measured $\langle I\rangle(Z, A)$ and $d\langle I\rangle/d\mathrm{TKE}$ for many fragments, but only used 2 to 4 levels from the ground-state band for each fragment. They did not see a sawtooth in $\langle I\rangle(Z, A)$ or a TKE-dependence. The former is inconsistent with modern experiments that were performed with better instruments.

- Göök *et al.* (2014) [8] measured $\overline{N}_n(A, \mathrm{TKE})$. Since $\overline{N}_n$ is strongly correlated with E^*,

we can refer to these results for estimates of excitation energy sharing as a function of mass and TKE.

- Gjestvang *et al.* (2021) [11] observed small positive correlations between $\overline{N}_\gamma$ and E_x in ^{240}Pu(d, pf). This result seems to imply energy-dependence of spin generation, but is not sufficient on its own.

- Travar *et al.* (2021) [9] observed the γ-ray multiplicity sawtooth $\overline{N}_\gamma(A)$ and found that $\overline{N}_\gamma$(TKE) saturated upon moving from higher to lower TKE. The latter would suggest spin saturation, but is not mass-differentiated.

- Wilson *et al.* (2021) [14] measured the spin sawtooth, analogous to the neutron and γ-ray multiplicity sawtooths: $\langle I \rangle(Z, A)$. This measurement calls into question the validity of Wilhelmy *et al.*

- Gjestvang *et al.* (2023) [15] measured the isomeric yield ratio (IYR) of ^{134}Te and saw no spin-energy correlations, although the extraction of the spin distribution from the IYR depends on the statistical model of spin feeding.

- Marin *et al.* (2024) [10] measured several things, among them the equivalent of Göök's neutron, but for γ rays: $\overline{N}_\gamma(A, \text{TKE})$. This measurement determined that some fragment masses were more susceptible to the saturation from Travar *et al.* than others.

Table 5.1: Summary of selected correlated fission measurements. The measurements in this dissertation are included at the bottom.

Reference	Reaction	Measurement	Notes
Wilhelmy *et al.* [13]	^{252}Cf(sf)	$\langle I\rangle(Z,A)$, $d\langle I\rangle/d\mathrm{TKE}$	Superseded by Wilson
Göök *et al.* [8]	^{252}Cf(sf)	$\overline{N}_n(A,\mathrm{TKE})$	
Gjestvang *et al.* (2021) [11]	^{240}Pu$(d,p\mathrm{f})$	$\overline{N}_\gamma(E_x)$	
Travar *et al.* [9]	^{252}Cf(sf)	$\overline{N}_\gamma(A)$ and $\overline{N}_\gamma(\mathrm{TKE})$	
Wilson *et al.* [14]	Many	$\langle I\rangle(Z,A)$	Spin sawtooth
Gjestvang *et al.* (2023) [15]	Many	$d\mathrm{IYR}/dE_x$	
Marin *et al.* [10]	^{252}Cf(sf)	$\overline{N}_\gamma(A,\mathrm{TXE})$	Unifies Travar *et al.* results
Giha *et al.* [12]	^{239}Pu(n,f)	$\overline{N}_\gamma(\langle E_x\rangle)$	
Giha *et al.* (tbd)	^{252}Cf(sf)	$\langle I\rangle(Z,A,\mathrm{TKE})$	^{144}Ba only

The ^{239}Pu(n,f) experiment and Gjestvang *et al.* (2021) [11] agree well on the slope $d\overline{N}_\gamma/dE_x$, despite populating the compound nuclear states with different reactions: we measured 0.085 ± 0.010 MeV^{-1} and they measured 0.08 ± 0.03 MeV^{-1}. Gjestvang *et al.* did not observe any change in the γ-ray spectrum shape, so connecting this multiplicity increase to spin would be tenuous. In contrast, we observed a disproportionate growth in the spectrum around $E_\gamma \sim 0.7$ MeV and connected it back to positive spin-energy correlations. Positive as they may be, the fact remains that this multiplicity dependence is slight. Further obfuscating our ability to quantify the spin-energy correlations are the complete summing over all fragment masses and the non-trivial relationship between E_x and the E^* of the fragments. We refined both of these deficiencies in our next experiment.

Wilhelmy *et al.* [13] performed a correlated measurement with two HPGe detectors and a fragment detector that measures TKE. They performed a similar analysis to those of Wilson *et al.* [14] and of Chapter 4, but with an extremely important difference: they were only sensitive to the first two to four ground-state-band transitions in each nucleus

they studied. This leaves out a tremendous amount of information on high-spin states and explains why they did not see the spin sawtooth of Wilson *et al.*. Furthermore, it renders them insensitive to all but the largest changes in spin as a function of TKE, $d\langle I\rangle/d\text{TKE}$.

Travar *et al.* and Wilson *et al.* were released in quick succession, unambiguously demonstrating the γ-ray and spin sawtooths in fission as a function of fragment mass. Wilson *et al.* had no energy dependence, but Travar *et al.* did. They showed that the γ-ray multiplicity saturates at low TKE (high TXE), but did not differentiate this saturation as a function of fragment mass. Marin *et al.* [10] succeeded in differentiating $\overline{N}_\gamma$ with respect to both fragment mass and TXE, $\overline{N}_\gamma(A, \text{TXE})$ and set the stage for Chapter 4.

Marin *et al.* found that the $\overline{N}_\gamma(\text{TXE})$ saturated, and even decreased, at high TXE for some fragment mass ranges. In other mass ranges, it continued to grow. If (i) the spin were generated statistically, (ii) the change in $\overline{N}_\gamma$ is proportional to a change in spin, and (iii) the TXE is shared somewhat evenly between the fragments, the spin should increase with TXE for all mass ranges. We can verify (iii) for some mass splits with the neutron multiplicity results of Göök *et al.* [8]. For heavy fragments around ^{144}Ba the average $\overline{N}_n(\text{TKE})$ is split evenly between the fragments, indicating a nearly equal partition of excitation energy. So, either (i) or (ii) must be false, but $\overline{N}_\gamma$ measurements alone cannot validate (ii).

This gap is where the experiment of Chapter 4 fits. Instead of measuring $\overline{N}_\gamma$, we measured $\langle I\rangle(Z, A, \text{TKE})$ for a specific fragment that is expected to receive an even share of the TXE. Yet, the spin appears insensitive to TKE. This measurement supports the interpretation that statistical excitation is insufficient to explain the picture of spin generation in nuclear fission.

The next step for filling out $\langle I\rangle(Z, A, \text{TKE})$ is to apply the analysis of Chapter 4 to more fragments, with the goal of covering a broad fragment mass range. These data, combined with IYR measurements like Gjestvang *et al.* (2023) [15], will eventually be combined to complete the picture of fragment initial conditions.

5.3 Future work

The obvious next step is to perform the Chapter 4 analysis on more fragments—the original goal of this dissertation, but one that was cut short by time constraints. The result would be akin to the spin sawtooth of Wilson *et al.* [14], $\langle I \rangle(A)$, but with an energy axis—the spin-energy surface, $\langle I \rangle(A, \mathrm{TKE})$. Completing this analysis would be a significant step toward measuring everything that can be accessed in experiment for ^{252}Cf(sf), at least from the perspective of spin-energy correlations. From there, I propose three extensions—upgrading the chamber, including statistical emission in the analysis, and looking at angular correlations.

The first extension is upgrading the TFGIC from Chapter 3. Experiments like Chapter 4 require time on in-demand user facilities like Gammasphere, so the efficiency with which we accept fission events is incredibly important and determines which fragments we can reasonably perform γ-ray spectroscopy on. If we radially segment one or both of the anodes, we can measure both the polar and azimuthal angles of the fission axis, fully defining it and eliminating the need for a $\cos\theta_\mathrm{f}$ cut. This change alone would increase our statistics by almost an order of magnitude. The next upgrade would be to add a beam window. The TFGIC is relatively robust to false triggers from α pileup since it requires coincidence in both sides, but α decay during the rising edge of a fragment anode pulse can still degrade the TKE resolution, and therefore the mass and angular resolutions as well. This fact is not much of a concern for ^{252}Cf(sf), but other spontaneously fissioning actinides have much less favorable sf/α branching ratios. This pileup concern limits a comparable ^{240}Pu(sf) experiment to about 0.01 fissions$\cdot s^{-1}$ or less (see Fig. 5.1), compared to our 4000 fissions$\cdot s^{-1}$ for ^{252}Cf(sf). A beam window would allow us to perform similar experiments with other fissionable targets, via neutron-, photon-, or ion-induced fission where targets could be made with less material and α pileup less of a concern. It also presents an opportunity to access completely different fragment initial conditions, and in the case of photon- or ion-induced fission, a new set of independent variables like beam polarization.

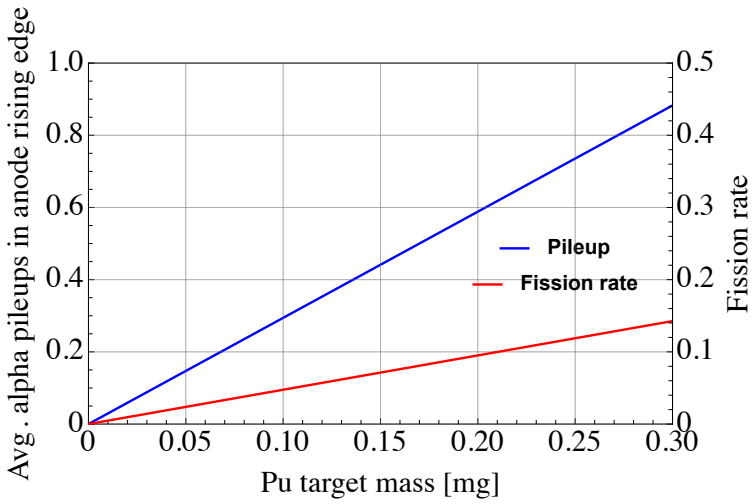

Figure 5.1: Expected number of α pileups in anode rising edge and fission rate (s^{-1}) as a function of ^{240}Pu target mass.

I would make efforts to improve the target deposition and backing. The target was apparently of nonuniform thickness, as even fragments exiting the source side were noticeably broadened in energy. As evidenced by two ^{252}Cf targets breaking in the chamber under, the carbon backing was very flimsy and a constant source of worry. A more uniform source spot on a Au-coated polyamide backing would perform better and be more robust.

The second extension is more difficult. While we have good reason to believe that statistical emission has little effect on the fragment spin, it is not confirmed—and could be correlated with fragment (Z, A) or energy. To get closer than we already have to the fragment initial conditions on Fig. 5.2, we must include statistical γ rays, and then neutrons, in our analysis. Statistical γ rays connect levels in the quasi-continuum and therefore measuring their energies means little in the way of reconstructing spin. One could measure the angular distribution of the E_γ continuum to find the average ΔI for a statistical γ, but separating the statistical γ rays of one fragment from those of its partner and other contaminants has no obvious answer. One potential solution is relying on a de-excitation code like RAINIER [103] to build a response matrix between fragment initial conditions and statistical γ-ray spectrum that could then be inverted, but that introduces model dependence. The

problem of simultaneously doing γ-ray spectroscopy has been considered at length, but no obvious solution exists. We placed some *trans*-stilbene scintillators inside of Gammasphere during our experiment, but the combined efficiency for detecting yrast γ rays and fission neutrons means that just adding scintillators is not a practical solution. One could imagine surrounding Gammasphere with segmented, high-efficiency neutron capture detectors: the neutron angular distribution could give ΔI, and the multiplicity could give a decent idea of the total neutron ΔE^* since most of it is due to the separation energy anyway.

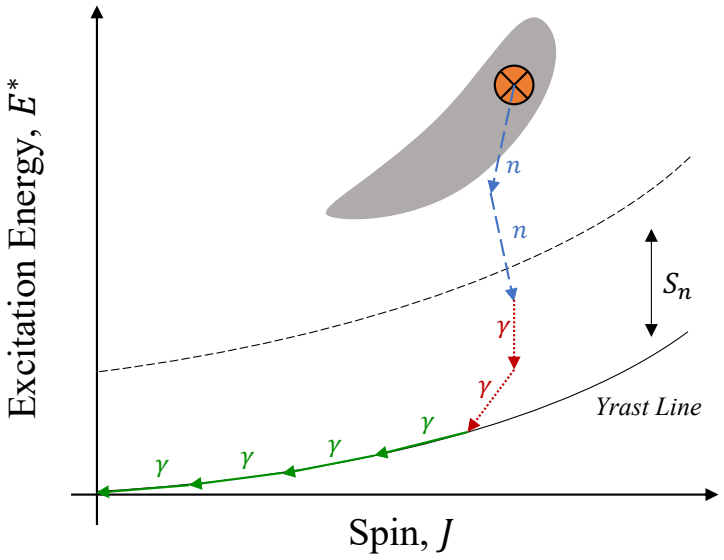

Figure 5.2: The fission fragment de-excitation diagram, again.

Lastly, angular correlations between the fragment axis and the emitted neutrons and γ rays deserve some attention. We briefly alluded to the fact that ^{144}Ba appeared to still be polarized relative to the fission axis, based on the angular distribution of the 331-keV ($4^+ \rightarrow 2^+$) transition. If an isotropic neutron distribution were measured in coincidence with γ rays that indicate polarization, it would confirm that neutrons remove little spin. Simply looking at the angular distributions of discrete transitions in other nuclei, as well as statistical γ rays, we could learn much about whether polarization evolves with fragment mass or energy. Finally, by enforcing coincidence on two transitions from common partner fragments, we can check for correlations between the polarization of fragments in the same

fission event. These correlations should be accessible with the data from Chapter 4.

5.4 Final remarks

Fission research is in an exciting era due to advances in computational modeling and a few groundbreaking experiments—I feel lucky that my time as a graduate student matched up so well with this era. As these correlated measurements become more sophisticated, it does seem that a major breakthrough is on the horizon. We start to feel that the picture is nearly filled in as we piece together several experiments in Section 5.2. Yet, despite our efforts in Chapter 4, the "ultimate fission experiment" in which we can reconstruct everything about the fragments, neutrons, and γ rays still eludes us.

This dissertation ultimately yields a negative result: the spin generation mechanism is not simply statistical. To help our theorist colleagues construct a positive result, *i.e.*, conclude what it actually is, we need to finish measuring the energy-dependent spin sawtooth, $\langle I \rangle(Z, A, \mathrm{TKE})$. That, and more, are almost within our grasp.

Bibliography

[1] O. Hahn and F. Strassmann, "Über den nachweis und das verhalten der bei der bestrahlung des urans mittels neutronen entstehenden erdalkalimetalle", Naturwissenschaften **27**, 11–15 (1939).

[2] L. Meitner and O. R. Frisch, "Products of the fission of the uranium nucleus", Nature **143**, 471–472 (1939).

[3] S. Goriely, "The fundamental role of fission during r-process nucleosynthesis in neutron star mergers", The European Physical Journal A **51**, 22 (2015).

[4] N. Vassh, R. Vogt, R. Surman, J. Randrup, T. M. Sprouse, M. R. Mumpower, P. Jaffke, D. Shaw, E. M. Holmbeck, Y. Zhu, and G. C. McLaughlin, "Using excitation-energy dependent fission yields to identify key fissioning nuclei in r-process nucleosynthesis", Journal of Physics G: Nuclear and Particle Physics **46**, 065202 (2019).

[5] M. R. Mumpower, P. Jaffke, M. Verriere, and J. Randrup, "Primary fission fragment mass yields across the chart of nuclides", Phys. Rev. C **101**, 054607 (2020).

[6] N. Vassh, M. R. Mumpower, G. C. McLaughlin, T. M. Sprouse, and R. Surman, "Coproduction of light and heavy r-process elements via fission deposition", The Astrophysical Journal **896**, 28 (2020).

[7] X. Wang, N. Vassh, T. Sprouse, M. Mumpower, R. Vogt, J. Randrup, and R. Surman, "MeV gamma rays from fission: a distinct signature of actinide production in neutron star mergers", The Astrophysical Journal **903**, L3 (2020).

[8] A. Göök, F.-J. Hambsch, and M. Vidali, "Prompt neutron multiplicity in correlation with fragments from spontaneous fission of 252Cf", Physical Review C **90**, 064611 (2014).

[9] M. Travar, V. Piau, A. Göök, O. Litaize, J. Nikolov, A. Oberstedt, S. Oberstedt, J. Enders, M. Peck, W. Geerts, and M. Vidali, "Experimental information on mass- and TKE-dependence of the prompt fission γ-ray multiplicity", Physics Letters B **817**, 136293 (2021).

[10] S. Marin, I. A. Tolstukhin, N. P. Giha, F. Tovesson, V. Protopopescu, and S. A. Pozzi, "Measurement of fragment-correlated γ-ray emission from ^{252}Cf(sf)", Phys. Rev. C **109**, 054617 (2024).

[11] D. Gjestvang, S. Siem, F. Zeiser, J. Randrup, R. Vogt, J. N. Wilson, F. Bello-Garrote, L. A. Bernstein, D. L. Bleuel, M. Guttormsen, A. Görgen, A. C. Larsen, K. L. Malatji, E. F. Matthews, A. Oberstedt, S. Oberstedt, T. Tornyi, G. M. Tveten, and A. S. Voyles, "Excitation energy dependence of prompt fission γ-ray emission from ^{241}Pu*", Phys. Rev. C **103**, 034609 (2021).

[12] N. P. Giha, S. Marin, J. A. Baker, I. E. Hernandez, K. J. Kelly, M. Devlin, J. M. O'Donnell, R. Vogt, J. Randrup, P. Talou, I. Stetcu, A. E. Lovell, O. Litaize, O. Serot, A. Chebboubi, C.-Y. Wu, S. D. Clarke, and S. A. Pozzi, "Correlations between energy and γ-ray emission in ^{239}Pu(n,f)", Phys. Rev. C **107**, 014612 (2023).

[13] J. B. Wilhelmy, E. Cheifetz, R. C. Jared, S. G. Thompson, H. R. Bowman, and J. O. Rasmussen, "Angular momentum of primary products formed in the spontaneous fission of ^{252}Cf", Phys. Rev. C **5**, 2041–2060 (1972).

[14] J. N. Wilson, D. Thisse, M. Lebois, N. Jovančević, D. Gjestvang, R. Canavan, M. Rudigier, D. Étasse, R.-B. Gerst, L. Gaudefroy, E. Adamska, P. Adsley, A. Algora, M. Babo, K. Belvedere, J. Benito, G. Benzoni, A. Blazhev, A. Boso, S. Bottoni, M. Bunce, R. Chakma, N. Cieplicka-Oryńczak, S. Courtin, M. L. Cortés, P. Davies,

C. Delafosse, M. Fallot, B. Fornal, L. Fraile, A. Gottardo, V. Guadilla, G. Häfner, K. Hauschild, M. Heine, C. Henrich, I. Homm, F. Ibrahim, Ł. W. Iskra, P. Ivanov, S. Jazrawi, A. Korgul, P. Koseoglou, T. Kröll, T. Kurtukian-Nieto, L. Le Meur, S. Leoni, J. Ljungvall, A. Lopez-Martens, R. Lozeva, I. Matea, K. Miernik, J. Nemer, S. Oberstedt, W. Paulsen, M. Piersa, Y. Popovitch, C. Porzio, L. Qi, D. Ralet, P. H. Regan, K. Rezynkina, V. Sánchez-Tembleque, S. Siem, C. Schmitt, P.-A. Söderström, C. Sürder, G. Tocabens, V. Vedia, D. Verney, N. Warr, B. Wasilewska, J. Wiederhold, M. Yavahchova, F. Zeiser, and S. Ziliani, "Angular momentum generation in nuclear fission", Nature **590**, 566–570 (2021).

[15] D. Gjestvang, J. N. Wilson, A. Al-Adili, S. Siem, Z. Gao, J. Randrup, D. Thisse, M. Lebois, N. Jovan čevi ć, R. Canavan, M. Rudigier, D. Étasse, R.-B. Gerst, E. Adamska, P. Adsley, A. Algora, C. Belvedere, J. Benito, G. Benzoni, A. Blazhev, A. Boso, S. Bottoni, M. Bunce, R. Chakma, N. Cieplicka-Ory ńczak, S. Courtin, M. L. Cortés, P. Davies, C. Delafosse, M. Fallot, B. Fornal, L. Fraile, A. Gottardo, V. Guadilla, G. Häfner, K. Hauschild, M. Heine, C. Henrich, I. Homm, F. Ibrahim, Ł. W. Iskra, P. Ivanov, S. Jazrawi, A. Korgul, P. Koseoglou, T. Kröll, T. Kurtukian-Nieto, S. Leoni, J. Ljungvall, A. Lopez-Martens, R. Lozeva, I. Matea, K. Miernik, J. Nemer, S. Oberstedt, W. Paulsen, M. Piersa-Siłkowska, Y. Popovitch, C. Porzio, L. Qi, P. H. Regan, K. Rezynkina, V. Sánchez-Tembleque, C. Schmitt, P.-A. Söderström, C. Sürder, G. Tocabens, V. Vedia, D. Verney, N. Warr, B. Wasilewska, J. Wiederhold, M. Yavahchova, and S. Ziliani, "Examination of how properties of a fissioning system impact isomeric yield ratios of the fragments", Phys. Rev. C **108**, 064602 (2023).

[16] G. Herrmann, "Discovery and confirmation of fission", Nuclear Physics A **502**, 141–158 (1989).

[17] P. E. FERMI, "Possible production of elements of atomic number higher than 92", Nature **133**, 898–899 (1934).

[18] *Oppenheimer*, 2023.

[19] https://commons.wikimedia.org/w/index.php?curid=1540082, 2024.

[20] N. Bohr and J. A. Wheeler, "The mechanism of nuclear fission", Physical Review **56**, 426–450 (1939).

[21] H. A. Bethe and R. F. Bacher, "Nuclear physics a. stationary states of nuclei", Rev. Mod. Phys. **8**, 82–229 (1936).

[22] C. F. v. Weizsäcker, "Zur theorie der kernmassen", Zeitschrift für Physik **96**, 431–458 (1935).

[23] L. Glendenin and E. Steinberg, "Fission yields in spontaneous fission of cf252", Journal of Inorganic and Nuclear Chemistry **1**, 45–48 (1955).

[24] V. Strutinsky, "Shell effects in nuclear masses and deformation energies", Nuclear Physics A **95**, 420–442 (1967).

[25] T. Ichikawa, A. Iwamoto, P. Möller, and A. J. Sierk, "Contrasting fission potential-energy structure of actinides and mercury isotopes", Phys. Rev. C **86**, 024610 (2012).

[26] F. Gönnenwein, "Neutron and gamma emission in fission", in Lanl fiesta fission school & workshop (2014).

[27] I. Stetcu, A. E. Lovell, P. Talou, T. Kawano, S. Marin, S. A. Pozzi, and A. Bulgac, *Angular momentum removal by neutron and γ-ray emissions during fission fragment decays*, 2021.

[28] A. Spyrou, S. N. Liddick, F. Naqvi, B. P. Crider, A. C. Dombos, D. L. Bleuel, B. A. Brown, A. Couture, L. Crespo Campo, M. Guttormsen, A. C. Larsen, R. Lewis, P. Möller, S. Mosby, M. R. Mumpower, G. Perdikakis, C. J. Prokop, T. Renstrøm, S. Siem, S. J. Quinn, and S. Valenta, "Strong neutron-γ competition above the neutron threshold in the decay of ^{70}Co", Phys. Rev. Lett. **117**, 142701 (2016).

[29] A. Sonzogni, "Experimental data on ground- and excited-state properties for all nuclei with mass number a=144 have been compiled and evaluated. states populated in radioactive decay as well as in nuclear reactions have been considered. for these nuclei, level and decay schemes have been built, as well as tables of nuclear properties. this work supersedes the 1989 evaluation by j.k. tuli (1989tu02). manuscripts published before december 2000 have been included in this work", Nuclear Data Sheets **93**, 599–762 (2001).

[30] L. G. Moretto, G. F. Peaslee, and G. J. Wozniak, "Angular — momentum — bearing modes in fission", Nuclear Physics A **502**, 453–472 (1989).

[31] J. Fréhaut, A. Bertin, and R. Bois, in Nuclear data for science and technology, edited by K. H. Böckhoff (1983), pp. 78–81.

[32] J. Fréhaut, *Neutron gamma competition in fast fission*, tech. rep., INDC(NDS)–220 (International Atomic Energy Agency (IAEA), 1989), pp. 99–111.

[33] L. Qi, M. Lebois, J. N. Wilson, A. Chatillon, S. Courtin, G. Fruet, G. Georgiev, D. G. Jenkins, B. Laurent, L. Le Meur, A. Maj, P. Marini, I. Matea, L. Morris, V. Nanal, P. Napiorkowski, A. Oberstedt, S. Oberstedt, C. Schmitt, O. Serot, M. Stanoiu, and B. Wasilewska, "Statistical study of the prompt-fission γ-ray spectrum for ^{238}U(n, f) in the fast-neutron region", Phys. Rev. C **98**, 014612 (2018).

[34] J.-M. Laborie, R. Billnert, G. Bélier, A. Oberstedt, S. Oberstedt, and J. Taieb, "First experimental prompt γ-ray spectra in fast-neutron-induced fission of ^{238}U", Phys. Rev. C **98**, 054604 (2018).

[35] A. Oberstedt, M. Lebois, S. Oberstedt, L. Qi, and J. N. Wilson, "Prompt γ-ray characteristics from ^{235}U(n, f) at E_n= 1.7 MeV", The European Physical Journal A **56**, 236 (2020).

[36] S. J. Rose, F. Zeiser, J. N. Wilson, A. Oberstedt, S. Oberstedt, S. Siem, G. M. Tveten, L. A. Bernstein, D. L. Bleuel, J. A. Brown, L. Crespo Campo, F. Giacoppo, A. Görgen,

M. Guttormsen, K. Hady ńska, A. Hafreager, T. W. Hagen, M. Klintefjord, T. A. Laplace, A. C. Larsen, T. Renstrøm, E. Sahin, C. Schmitt, T. G. Tornyi, and M. Wiedeking, "Energy dependence of the prompt γ-ray emission from the (d, p)-induced fission of ^{234}U* and ^{240}Pu*", Phys. Rev. C **96**, 014601 (2017).

[37] D. Brown, M. Chadwick, R. Capote, A. Kahler, A. Trkov, M. Herman, A. Sonzogni, Y. Danon, A. Carlson, M. Dunn, D. Smith, G. Hale, G. Arbanas, R. Arcilla, C. Bates, B. Beck, B. Becker, F. Brown, R. Casperson, J. Conlin, D. Cullen, M.-A. Descalle, R. Firestone, T. Gaines, K. Guber, A. Hawari, J. Holmes, T. Johnson, T. Kawano, B. Kiedrowski, A. Koning, S. Kopecky, L. Leal, J. Lestone, C. Lubitz, J. Márquez Damián, C. Mattoon, E. McCutchan, S. Mughabghab, P. Navratil, D. Neudecker, G. Nobre, G. Noguere, M. Paris, M. Pigni, A. Plompen, B. Pritychenko, V. Pronyaev, D. Roubtsov, D. Rochman, P. Romano, P. Schillebeeckx, S. Simakov, M. Sin, I. Sirakov, B. Sleaford, V. Sobes, E. Soukhovitskii, I. Stetcu, P. Talou, I. Thompson, S. van der Marck, L. Welser-Sherrill, D. Wiarda, M. White, J. Wormald, R. Wright, M. Zerkle, G. Žerovnik, and Y. Zhu, "Endf/b-viii.0: the 8th major release of the nuclear reaction data library with cielo-project cross sections, new standards and thermal scattering data", Nuclear Data Sheets **148**, Special Issue on Nuclear Reaction Data, 1–142 (2018).

[38] K. J. Kelly, M. Devlin, J. M. O'Donnell, J. A. Gomez, D. Neudecker, R. C. Haight, T. N. Taddeucci, S. M. Mosby, H. Y. Lee, C. Y. Wu, R. Henderson, P. Talou, T. Kawano, A. E. Lovell, M. C. White, J. L. Ullmann, N. Fotiades, J. Henderson, and M. Q. Buckner, "Measurement of the ^{239}Pu(n, f) prompt fission neutron spectrum from 10 kev to 10 MeV induced by neutrons of energy 1–20 MeV", Phys. Rev. C **102**, 034615 (2020).

[39] P. Talou, I. Stetcu, P. Jaffke, M. E. Rising, A. E. Lovell, and T. Kawano, "Fission fragment decay simulations with the cgmf code", Computer Physics Communications **269**, https://doi.org/10.1016/j.cpc.2021.108087 (2021).

[40] O. Litaize, O. Serot, and L. Berge, "Fission modelling with FIFRELIN", The European Physical Journal A **51**, 177 (2015).

[41] J. Randrup and R. Vogt, "Calculation of fission observables through event-by-event simulation", Phys. Rev. C **80**, 024601 (2009).

[42] https://lansce.lanl.gov.

[43] C. Wu, R. Henderson, R. Haight, H. Lee, T. Taddeucci, B. Bucher, A. Chyzh, M. Devlin, N. Fotiades, E. Kwan, J. O'Donnell, B. Perdue, and J. Ullmann, "A multiple parallel-plate avalanche counter for fission-fragment detection", Nuclear Instruments and Methods in Physics Research Section A: Accelerators, Spectrometers, Detectors and Associated Equipment **794**, 76–79 (2015).

[44] https://eljentechnology.com/products/liquid-scintillators/ej-301-ej-309.

[45] S. Marin, V. A. Protopopescu, R. Vogt, M. J. Marcath, S. Okar, M. Y. Hua, P. Talou, P. F. Schuster, S. D. Clarke, and S. A. Pozzi, "Event-by-event neutron–photon multiplicity correlations in 252cf(sf)", Nuclear Instruments and Methods in Physics Research Section A: Accelerators, Spectrometers, Detectors and Associated Equipment **968**, 163907 (2020).

[46] S. A. Pozzi, E. Padovani, and M. Marseguerra, "MCNP-PoliMi: a monte-carlo code for correlation measurements", Nuclear Instruments and Methods in Physics Research Section A: Accelerators, Spectrometers, Detectors and Associated Equipment **513**, 550–558 (2003).

[47] S. Schmitt, "Data unfolding methods in high energy physics", EPJ Web Conf. **137**, 11008 (2017).

[48] I. Stetcu, M. Chadwick, T. Kawano, P. Talou, R. Capote, and A. Trkov, "Evaluation of the prompt fission gamma properties for neutron induced fission of 235,238u and 239pu", Nuclear Data Sheets **163**, 261–279 (2020).

[49] H. A. Bethe, "An attempt to calculate the number of energy levels of a heavy nucleus", Phys. Rev. **50**, 332–341 (1936).

[50] T. Kawano, *Unified coupled-channels and hauser-feshbach model calculation for nuclear data evaluation*, tech. rep., NUCLEAR PHYSICS AND RADIATION PHYSICS (Japan, 2019), pp. 59–64.

[51] R. Capote, M. Herman, P. Obložinský, P. Young, S. Goriely, T. Belgya, A. Ignatyuk, A. Koning, S. Hilaire, V. Plujko, M. Avrigeanu, O. Bersillon, M. Chadwick, T. Fukahori, Z. Ge, Y. Han, S. Kailas, J. Kopecky, V. Maslov, G. Reffo, M. Sin, E. Soukhovitskii, and P. Talou, "Ripl – reference input parameter library for calculation of nuclear reactions and nuclear data evaluations", Nuclear Data Sheets **110**, Special Issue on Nuclear Reaction Data, 3107–3214 (2009).

[52] Thulliez, L., Litaize, O., and Serot, O., "Sensitivity studies of spin cut-off models on fission fragment observables", EPJ Web of Conferences **111**, 10003 (2016).

[53] A. J. M. Plompen, O. Cabellos, C. De Saint Jean, M. Fleming, A. Algora, M. Angelone, P. Archier, E. Bauge, O. Bersillon, A. Blokhin, F. Cantargi, A. Chebboubi, C. Diez, H. Duarte, E. Dupont, J. Dyrda, B. Erasmus, L. Fiorito, U. Fischer, D. Flammini, D. Foligno, M. R. Gilbert, J. R. Granada, W. Haeck, F.-J. Hambsch, P. Helgesson, S. Hilaire, I. Hill, M. Hursin, R. Ichou, R. Jacqmin, B. Jansky, C. Jouanne, M. A. Kellett, D. H. Kim, H. I. Kim, I. Kodeli, A. J. Koning, A. Y. Konobeyev, S. Kopecky, B. Kos, A. Krása, L. C. Leal, N. Leclaire, P. Leconte, Y. O. Lee, H. Leeb, O. Litaize, M. Majerle, J. I. Márquez Damián, F. Michel-Sendis, R. W. Mills, B. Morillon, G. Noguère, M. Pecchia, S. Pelloni, P. Pereslavtsev, R. J. Perry, D. Rochman, A. Röhrmoser, P. Romain, P. Romojaro, D. Roubtsov, P. Sauvan, P. Schillebeeckx, K. H. Schmidt, O. Serot, S. Simakov, I. Sirakov, H. Sjöstrand, A. Stankovskiy, J. C. Sublet, P. Tamagno, A. Trkov, S. van der Marck, F. Álvarez-Velarde, R. Villari, T. C.

Ware, K. Yokoyama, and G. Žerovnik, "The joint evaluated fission and fusion nuclear data library, jeff-3.3", The European Physical Journal A **56**, 181 (2020).

[54] F. Bečvář, "Simulation of γ cascades in complex nuclei with emphasis on assessment of uncertainties of cascade-related quantities", Nuclear Instruments and Methods in Physics Research Section A: Accelerators, Spectrometers, Detectors and Associated Equipment **417**, 434–449 (1998).

[55] D. Regnier, O. Litaize, and O. Serot, "An improved numerical method to compute neutron/gamma deexcitation cascades starting from a high spin state", Computer Physics Communications **201**, 19–28 (2016).

[56] O. Litaize, O. Serot, L. Thulliez, and A. Chebboubi, "Prompt particle emission in correlation with fission fragments", EPJ Web Conf. **146**, 04006 (2017).

[57] O. Litaize, A. Chebboubi, O. Serot, L. Thulliez, T. Materna, and M. Rapala, "Influence of nuclear structure data on fission observables", EPJ Nuclear Sci. Technol. **4**, 28 (2018).

[58] R. Vogt and J. Randrup, "Angular momentum effects in fission", Phys. Rev. C **103**, 014610 (2021).

[59] J. Randrup and R. Vogt, "Refined treatment of angular momentum in the event-by-event fission model FREYA", Phys. Rev. C **89**, 044601 (2014).

[60] R. Vogt and J. Randrup, "Improved modeling of photon observables with the event-by-event fission model freya", Phys. Rev. C **96**, 064620 (2017).

[61] L. Qi, C. Schmitt, M. Lebois, A. Oberstedt, S. Oberstedt, J. N. Wilson, A. Al-Adili, A. Chatillon, D. Choudhury, A. Gatera, G. Georgiev, A. Göök, B. Laurent, A. Maj, I. Matea, S. J. Rose, B. Wasilewska, and F. Zeiser, "Potential of prompt γ-ray emission studies in fast-neutron induced fission: a first step", The European Physical Journal A **56**, 98 (2020).

[62] A. Gatera, T. Belgya, W. Geerts, A. Göök, F.-J. Hambsch, M. Lebois, B. Maróti, A. Moens, A. Oberstedt, S. Oberstedt, F. Postelt, L. Qi, L. Szentmiklósi, G. Sibbens, D. Vanleeuw, M. Vidali, and F. Zeiser, "Prompt-fission γ-ray spectral characteristics from ^{239}Pu(n_{th}, f)", Phys. Rev. C **95**, 064609 (2017).

[63] K. J. Kelly, T. Kawano, J. M. O'Donnell, J. A. Gomez, M. Devlin, D. Neudecker, P. Talou, A. E. Lovell, M. C. White, R. C. Haight, T. N. Taddeucci, S. M. Mosby, H. Y. Lee, C. Y. Wu, R. Henderson, J. Henderson, and M. Q. Buckner, "Preequilibrium asymmetries in the ^{239}Pu(n, f) prompt fission neutron spectrum", Phys. Rev. Lett. **122**, 072503 (2019).

[64] M. Chadwick, M. Herman, P. Obložinský, M. Dunn, Y. Danon, A. Kahler, D. Smith, B. Pritychenko, G. Arbanas, R. Arcilla, R. Brewer, D. Brown, R. Capote, A. Carlson, Y. Cho, H. Derrien, K. Guber, G. Hale, S. Hoblit, S. Holloway, T. Johnson, T. Kawano, B. Kiedrowski, H. Kim, S. Kunieda, N. Larson, L. Leal, J. Lestone, R. Little, E. McCutchan, R. MacFarlane, M. MacInnes, C. Mattoon, R. McKnight, S. Mughabghab, G. Nobre, G. Palmiotti, A. Palumbo, M. Pigni, V. Pronyaev, R. Sayer, A. Sonzogni, N. Summers, P. Talou, I. Thompson, A. Trkov, R. Vogt, S. van der Marck, A. Wallner, M. White, D. Wiarda, and P. Young, "Endf/b-vii.1 nuclear data for science and technology: cross sections, covariances, fission product yields and decay data", Nuclear Data Sheets **112**, Special Issue on ENDF/B-VII.1 Library, 2887–2996 (2011).

[65] M. R. Mumpower, T. Kawano, and P. Möller, "Neutron-γ competition for β-delayed neutron emission", Phys. Rev. C **94**, 064317 (2016).

[66] G. Boutoux, B. Jurado, V. Méot, O. Roig, L. Mathieu, M. Aïche, G. Barreau, N. Capellan, I. Companis, S. Czajkowski, K.-H. Schmidt, J. Burke, A. Bail, J. Daugas, T. Faul, P. Morel, N. Pillet, C. Théroine, X. Derkx, O. Sérot, I. Matéa, and L. Tassan-Got, "Study of the surrogate-reaction method applied to neutron-induced capture cross sections", Physics Letters B **712**, 319–325 (2012).

[67] F. Zeiser, G. M. Tveten, G. Potel, A. C. Larsen, M. Guttormsen, T. A. Laplace, S. Siem, D. L. Bleuel, B. L. Goldblum, L. A. Bernstein, F. L. Bello Garrote, L. Crespo Campo, T. K. Eriksen, A. Görgen, K. Hadynska-Klek, V. W. Ingeberg, J. E. Midtbø, E. Sahin, T. Tornyi, A. Voinov, M. Wiedeking, and J. Wilson, "Restricted spin-range correction in the oslo method: the example of nuclear level density and γ-ray strength function from ^{239}Pu$(d, p\gamma)^{240}$Pu", Phys. Rev. C **100**, 024305 (2019).

[68] S. Marin, E. P. Sansevero, M. S. Okar, I. E. Hernandez, R. Vogt, J. Randrup, S. D. Clarke, V. A. Protopopescu, and S. A. Pozzi, "Directional dependence of the event-by-event neutron-γ multiplicity correlations in ^{252}Cf(sf)", Phys. Rev. C **105**, 054609 (2022).

[69] https://www.nndc.bnl.gov/nudat3/.

[70] U. Brosa, S. Grossmann, and A. Müller, "Nuclear scission", Physics Reports **197**, 167–262 (1990).

[71] D. L. Duke, "Fission fragment mass distributions and total kinetic energy release of 235-uranium and 238-uranium in neutron-induced fission at intermediate and fast neutron energies", Ph.D. dissertation (Colorado School of Mines, 2015).

[72] S. Marin, M. Stephan Okar, L. M. Clark, I. E. Hernandez, S. D. Clarke, and S. A. Pozzi, "Neutron-gamma correlation analysis using the fission sphere (fs-3)", in 2021 ieee nuclear science symposium and medical imaging conference (nss/mic) (2021), pp. 1–3.

[73] C. Budtz-Jørgensen, H.-H. Knitter, C. Straede, F.-J. Hambsch, and R. Vogt, "A twin ionization chamber for fission fragment detection", Nuclear Instruments and Methods in Physics Research Section A: Accelerators, Spectrometers, Detectors and Associated Equipment **258**, 209–220 (1987).

[74] A. Göök, W. Geerts, F.-J. Hambsch, S. Oberstedt, M. Vidali, and S. Zeynalov, "A position-sensitive twin ionization chamber for fission fragment and prompt neutron

correlation experiments", Nuclear Instruments and Methods in Physics Research Section A: Accelerators, Spectrometers, Detectors and Associated Equipment **830**, 366–374 (2016).

[75] L. Gaudefroy, T. Roger, J. Pancin, C. Spitaels, J. Aupiais, and J. Mottier, "A twin frisch-grid ionization chamber as a selective detector for the delayed gamma-spectroscopy of fission fragments", Nuclear Instruments and Methods in Physics Research Section A: Accelerators, Spectrometers, Detectors and Associated Equipment **855**, 133–139 (2017).

[76] S. Mosby, F. Tovesson, A. Couture, D. Duke, V. Kleinrath, R. Meharchand, K. Meierbachtol, J. M. O'Donnell, B. Perdue, D. Richman, and D. Shields, "A fission fragment detector for correlated fission output studies", Nuclear Instruments and Methods in Physics Research Section A: Accelerators, Spectrometers, Detectors and Associated Equipment **757**, 75–81 (2014).

[77] G. F. Knoll, *Radiation detection and measurement* (John Wiley and Sons, Inc., 2010 (4th edition)).

[78] C. Geuzaine and J.-F. Remacle, "Gmsh: a three-dimensional finite element mesh generator with built-in pre- and post-processing facilities", International Journal for Numerical Methods in Engineering **79**, 1309–1331 (2009).

[79] CSC – IT Center for Science LTD., *Elmer multiphysical simulation software*, (2020) `https://www.csc.fi/web/elmer`.

[80] T. H. Shin, P. L. Feng, J. S. Carlson, S. D. Clarke, and S. A. Pozzi, "Measured neutron light-output response for trans-stilbene and small-molecule organic glass scintillators", Nuclear Instruments and Methods in Physics Research Section A: Accelerators, Spectrometers, Detectors and Associated Equipment **939**, 36–45 (2019).

[81] S. A. Pozzi, S. D. Clarke, W. J. Walsh, E. C. Miller, J. L. Dolan, M. Flaska, B. M. Wieger, A. Enqvist, E. Padovani, J. K. Mattingly, D. L. Chichester, and P. Peerani,

"MCNPX-PoliMi for nuclear nonproliferation applications", Nuclear Instruments and Methods in Physics Research, Section A: Accelerators, Spectrometers, Detectors and Associated Equipment **694**, 119–125 (2012).

[82] J. B. Birks, *The Theory and Practice of Scintillation Counting*, Vol. 148, 3667 (Elsevier, 1964), p. 662.

[83] D. L. Duke, F. Tovesson, A. B. Laptev, S. Mosby, F.-J. Hambsch, T. Bry ś, and M. Vidali, "Fission-fragment properties in ^{238}U(n, f) between 1 and 30 mev", Phys. Rev. C **94**, 054604 (2016).

[84] M. Moore, J. Latta, L. Snyder, B. Fulsom, U. Greife, S. Lyons, L. Wood, D. Duke, M. Anastasiou, J. Barrett, N. Bowden, J. Bundgaard, R. Casperson, T. Classen, D. Dongwi, J. Gearhart, V. Geppert-Kleinrath, U. Greife, M. Haseman, M. Heffner, D. Higgins, J. King, J. Klay, J. Latta, W. Loveland, J. Magee, B. Manning, M. Mendenhall, M. Monterial, C. Prokop, S. Sangiorgio, B. Seilhan, L. Snyder, F. Tovesson, R. Towell, and L. Yao, "Stopping force analysis of ^{235}U elemental fission product yields for E_n = 0.11–92.4 MeV", Nuclear Data Sheets **184**, 1–28 (2022).

[85] F.-J. Hambsch, J. Van Aarle, and R. Vogt, "Is there a pulse height defect for methane?", Nuclear Instruments and Methods in Physics Research Section A: Accelerators, Spectrometers, Detectors and Associated Equipment **361**, 257–262 (1995).

[86] I.-Y. Lee, "The gammasphere", Nuclear Physics A **520**, c641–c655 (1990).

[87] A. Chemey, A. Pica, L. Yao, W. Loveland, H. Y. Lee, and S. A. Kuvin, "Total kinetic energy and mass yields from the fast neutron-induced fission of 239pu", European Physical Journal A **56**, 10.1140/epja/s10050-020-00295-6 (2020).

[88] A. Pica, A. T. Chemey, L. Yao, W. Loveland, H. Y. Lee, and S. A. Kuvin, "Total kinetic energy release in the fast-neutron-induced fission of ^{237}Np", Phys. Rev. C **102**, 064612 (2020).

[89] R. Yanez, L. Yao, J. King, W. Loveland, F. Tovesson, and N. Fotiades, "Excitation energy dependence of the total kinetic energy release in ^{235}U (n,f)", Phys. Rev. C **89**, 051604 (2014).

[90] S. Marin, I. A. Tolstukhin, N. Giha, M. Oberling, R. Knaack, B. Kay, D. Duke, K. Montoya, D. Connolly, W. Loveland, A. Chemey, S. Pozzi, and F. Tovesson, "Instrumentation for correlated prompt n-γ emission studies in coincidence with fission fragments", Nuclear Instruments and Methods in Physics Research Section A: Accelerators, Spectrometers, Detectors and Associated Equipment **1048**, 168027 (2023).

[91] S. Marin, I. A. Tolstukhin, N. P. Giha, M. B. Oberling, R. A. Knaack, B. P. Kay, D. L. Duke, K. B. Montoya, D. Connolly, W. Loveland, A. Chemey, S. A. Pozzi, and F. Tovesson, "Instrumentation for correlated prompt n-γ emission studies in coincidence with fission fragments", Nuclear Instruments and Methods in Physics Research Section A **1048**, 168027 (2023).

[92] R. Knaack, personal communication, 2023.

[93] https://wiki.anl.gov/gsdaq/DAQ_system.

[94] https://gitlab.phy.anl.gov/tlauritsen/gebsort.

[95] R. Brun and F. Rademakers, "Root — an object oriented data analysis framework", Nuclear Instruments and Methods in Physics Research Section A: Accelerators, Spectrometers, Detectors and Associated Equipment **389**, New Computing Techniques in Physics Research V, 81–86 (1997).

[96] https://www.ezag.com/fileadmin/ezag/user-uploads/isotopes/isotopes/Isotrak/isotrak-pdf/Decay_Schema_Data/Ra-226.pdf.

[97] https://radware.phy.ornl.gov.

[98] T. R. England and B. F. Rider, "Evaluation and compilation of fission product yields", Los Alamos Report LA-UR-94-3106, ENDF–349 (1997).

[99] M. Morháč, J. Kliman, V. Matoušek, M. Veselský, and I. Turzo, "Background elimination methods for multidimensional coincidence γ-ray spectra", Nuclear Instruments and Methods in Physics Research Section A: Accelerators, Spectrometers, Detectors and Associated Equipment **401**, 113–132 (1997).

[100] J. Blachot, "Nuclear data sheets for a = 104", Nuclear Data Sheets **108**, 2035–2172 (2007).

[101] D. De Frenne and A. Negret, "Nuclear data sheets for a = 106", Nuclear Data Sheets **109**, 943–1102 (2008).

[102] T. Kibédi, T. Burrows, M. Trzhaskovskaya, P. Davidson, and C. Nestor, "Evaluation of theoretical conversion coefficients using bricc", Nuclear Instruments and Methods in Physics Research Section A: Accelerators, Spectrometers, Detectors and Associated Equipment **589**, 202–229 (2008).

[103] L. Kirsch and L. Bernstein, "Rainier: a simulation tool for distributions of excited nuclear states and cascade fluctuations", Nuclear Instruments and Methods in Physics Research Section A: Accelerators, Spectrometers, Detectors and Associated Equipment **892**, 30–40 (2018).